# DEVELOPMENT OF FIBER-OPTIC BOLOMETER BASED ON A SILICON FABRY-PEROT INTERFEROMETER

By

Qiwen Sheng

A DISSERTATION

Submitted to
Michigan State University
in partial fulfillment of the requirements
for the degree of

Electrical Engineering – Doctor of Philosophy

2021

# ABSTRACT

## DEVELOPMENT OF FIBER-OPTIC BOLOMETER BASED ON A SILICON FABRY-PEROT INTERFEROMETER

By

Qiwen Sheng

In magnetically confined fusion (MCF), resistive bolometers are conventionally used for the detection of the plasma radiation helping to understand heat exhaust scenarios. However, the performance of resistive bolometer experiences unavoidable degradation in the practical applications due to the strong electromagnetic interference present in MCF systems. The limitations of the resistive bolometer motivate us to develop a novel fiber-optic bolometer instead of the original resistive bolometer due to the inherent immunity of optical fiber to the electromagnetic interference.

To develop a fiber-optic bolometer, we first theoretically study the spectral characteristics and noise performance of wavelength-interrogated fiber-optic sensors based on an extrinsic Fabry-Perot (FP) interferometer formed by thin metal mirrors. The fiber-optic bolometer is indeed a fiber-optic extrinsic FP interferometric temperature sensor. We develop a model and use it to analyze the effect of key sensor parameters, including the beam width of the incident light, the metal coating film thickness, the FP cavity length, and the wedge angle of the two mirrors, on the visibility and spectral width of the sensors. Through Monte Carlo simulations, we obtain an empirical equation that can be used to estimate the wavelength resolution from the visibility and bandwidth of reflection fringes. The work provides a useful tool for designing, constructing, and interrogating high-resolution fiber-optic extrinsic FP interferometric sensors with metal mirrors.

Based on the theoretical analysis mentioned above, we demonstrated a low-finesse fiber-optic silicon FP temperature sensor with high speed by considering the end-conduction effect, which refers to the unwanted heat transfer between the sensing element and the fiber stub delaying the sensor to reach thermal equilibrium with the ambient environment. Compared with the sensor of traditional design, the sensor of the new design shortened the characteristic response time in still air from 83 ms to 13 ms and improved the sensor resolution by a factor of 12, from 0.15 K to 0.012

K. Wavelength tracking method is commonly used for low finesse fiber-optic FP interferometric sensors due to its high resolution and straightforward implementation. We report the observation of random spurious jumps in a commonly used wavelength tracking method based on curve fitting. We analyze the origin of the spurious jumps through Monte Carlo simulations.The simulation results show that the spurious jumps arise mainly from the systematic errors of the curve fitting function for modeling the sensor spectrum and manifested by the changes in the pixel set for curve fitting. To eliminate these jumps, we propose a modified correlation demodulation method. The simulation and experimental results show that the modified correlation method can eliminate the spurious jumps encountered in the regular wavelength tracking.

In addition to the low-finesse fiber-optic bolometer, we demonstrate a fiber-optic bolometer based on a high-finesse silicon FP interferometer. The FP interferometer is a silicon pillar with one side coated with a high-reflectivity dielectric mirror and the other side coated with a gold mirror. A reference bolometer was used to effectively reduce the common noises from the laser drift and the ambient temperature variations. Experimental results show that our new fiber-optic bolometer has a noise equivalent power density of 0.27 W/m$^2$, which is comparable with the conventional resistive bolometer.Taking advantage of this new fiber-optic bolometer, we then carefully study the influences of mechanical vibration and static or quasi-static magnetic field, which can present in the practical applications, on the noise performance of bolometer. It is found that both the vibration and the magnetic field could cause large fluctuations in the demodulation results of bolometer measured in a stable environment due to the birefringence of the silicon FP interferometer. To mitigate the birefringence effects, we demonstrated two effective methods: polarization maintaining fiber replace the single-mode fiber, and polarization scrambling. Experimental results show that these two methods have a good performance in mitigating the birefringence effects.

*To my love Dongxiang Pan for the amazing support you have always provided.*

# ACKNOWLEDGEMENTS

I would first like to express my deepest gratitude to my supervisor, Dr. Ming Han, for his continuous guidance, support, trust, and encouragement throughout my study and research at University of Nebraska-Lincoln (UNL) and Michigan State University (MSU).

I would like to acknowledge the other committee members, Dr. Hogan, Dr. Udpa, and Dr. Haq for their help throughout my studies at MSU.

I would also like to thank the committee members, Dr. Argyropoulos, Dr.Alexander, and Dr. Tan for their help at the beginning of my work at UNL. I also want to give my special thanks to Dr. Xia Hong for her help, patience, and encouragement in the learning of solid physics, and the recommendation for the study at MSU.

I would like to thank the group members, past and present, that I have worked with during my stay at UNL and MSU. I would like to give my special thanks to Dr. Guigen Liu for his help both in and outside work. Thanks also go to Qi Zhang, Lingling Hu, Yujie Lu, Yupeng Zhu, Zigeng Liu, Xin Wang, Bohan Zhou, Huiyu (Peter) Zhao, Tailun Shen, Xiangyu Luo, Nezam Uddin, Abu F. Mitul, Hasanur R. Chowdhury, Sema G. Kilic, and Farzia Karim for their great contributions in the projects that we work on together. A big thank you goes to Jiong Hua (UNL), Dr. Wen Qian (UNL), Brian Wright, Roxanne Peacock, Meagan Kroll and other staff members at ECE who make our work easy. I would also like to thank Dr. Qi Wang, Dr. Zhen Qiu, and Dr. Yiming Deng for their aids in my research.

I would like to extend my acknowledgment to all of my friends in Lincoln and East Lansing. Special thanks would go to Tianjing Guo and Ying Li for their helps in our daily life, especially for the friendship of more than 10 years. Special thanks would also go to Weiyang Yang, Yue Zhang, and Chen Zheng for the good trips and dinners that we share. I also want to thank my aunt Zhongfang Shan, and her two lovely daughters Chen Zhu and Xi Zhu for the help in my daily life and work. I want to thank Dr. Ming Qu and his wife for the help from culture to language when I was in Lincoln. I would like to thank the wonderful couples of Jingpeng Liu & Liying Sun for sharing the wonderful trips. A big thank you goes to the couples, also my best friends, Jingyu Peng & Xinxin Wang, Hainan Zhao & Xin Liu, Chao Fang & Xin Chang, Nick & Wei Dong, and Jie Wang & Yang Fu for lots of things that I have learned from one of you.

Finally, I want to thank my family for their support throughout this process. I am deeply grateful to my wife, Dongxiang Pan, for her continuous support, great patience, encouragement, and dedication, for being the most important person in my whole life, and for being a wonderful mother of our lovely son, Steven Sheng.

# TABLE OF CONTENTS

# LIST OF TABLES

# LIST OF FIGURES

# CHAPTER 1

# INTRODUCTION

## 1.1 Research Background

As environment changes, scientists are trying to find environmentally friendly energy sources to meet our long-term needs instead of the fossil fuels. Magnetically confined fusion (MCF) using strong magnetic fields to confine high temperature MCF plasma is an important option [1]. In recent a few decades, the US and the nations around the world are working to harness this thermonuclear fusion. Although several megawatts fusion power have been produced, the generated power is still less than the injection power used for heating the fusion fuel, therefore a MCF reactor with higher performance is required. One of the major challenges in the design and operation of the MCF reactor is to control the excessive heat exhaust from the MCF plasma to make the plasma have a constant temperature. The exhausted heat is directed into the narrow boundary layers of the MCF with heat flux power density exceed 100 MW/m$^2$ well beyond the upper limit of the layers that can handle with a number of 10 MW/m$^2$.

To reduce the heat flux for the plasma-facing components to 10 MW/m$^2$, a conventional method is to introduce controlled amounts of impurities into the plasma converting exhaust power to the short wavelength photon radiation with wavelength range from soft x-ray to ultraviolet [2, 3]. The reduced plasma distributes more homogeneous heat flux reaching the plasma facing components. Despite extensive work has been reported [4–6], this method is not that straightforward. The too little impurities risks the overheating of plasma facing components, while the excessive impurities will reduce the activity of the plasma reaction, even cause a plasma reaction extinction.

To overcome these limits, research work has been carried out to understand the physics basis of the plasma radiation based on the state-of-the-art simulation techniques, and then the obtained simulation results need to be further verified and improved based on the feedback of the detected plasma radiation. The plasma radiation are usually obtained by using a cost-effective sensor with compatibility of high temperature and high vacuum. In addition, to obtain the spatial distribution of the plasma radiation, a large number of the compacted sensors need to be deployed for the radiation detection. Generally, the sensors are installed in a pinhole camera as shown in Fig. 1.1. It is seen that the spatial resolution is dependent on the distance of L between the aperture of the pinhole camera and the sensor. To improve the spatial resolution, the distance of L needs to be increased leading to a reduction of the plasma radiation power, therefore a cost-effective sensor with a low noise equivalent power density, defined as the power flux into the bolometer when the signal to noise ratio equals unity, will be desired, and the noise equivalent power density is also a key parameter to characterize the performance of sensor in MCF. The resistive bolometers are conventionally deployed in the most of the MCF reactors to measure the plasma radiation. For the resistive bolometers, the radiation is absorbed by a thin metal film (usually Au or Pt) and converted into temperature variation, which is then sensed by a meander resistor as shown in Fig. 1.2(a) (side view) and (b)(back view) [7, 8]. Taking advantage of the AC-driven Wheatstone bridge, high-precision measurement of the resistance of the meander resistor can be realized and thus high-resolution detection of electromagnetic radiation is obtained. A resistive bolometer using Pt absorbers on SiN membranes with a noise equivalent power density value of 0.2 W/m$^2$ has been reported [8]. While the resistive bolometers can achieve a low noise equivalent power density, they encounter the potential problems associated with extensive electric cabling and drift due to mismatching characteristics of the reference and sensing resistors. As an alternative, an infrared camera to

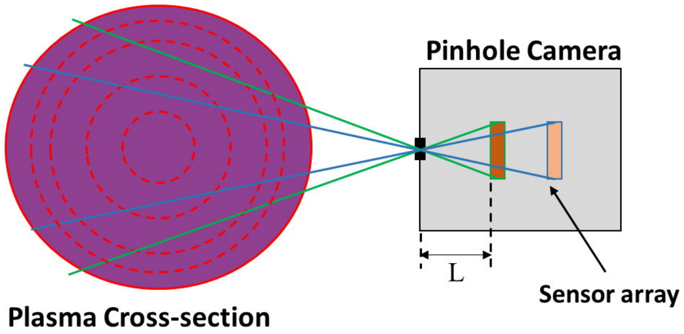

Figure 1.1: Layout of a pinhole camera showing how the distance of L influences on the resolution and the intensity of signal.

record the temperature variation of a thin metal foil that absorbs the incident electromagnetic radiations [9, 10]. This has the benefit of being resistant to electromagnetic interference and allowing 2D imaging of plasma radiation. Exploiting improvements in infrared cameras, a noise equivalent power density as low as 0.23 W/m$^2$ in a laboratory environment has been reported, but generally is limited to > 1 W/m$^2$ for reasonable spatio-temporal resolution [9]. Although the performance of resistive bolometer and the infrared video bolometer have been improved, they ultimately encounter the challenge when integrated into the plasma environment, leading to an unavoidable degradation in performance or limitations in where they can be deployed.

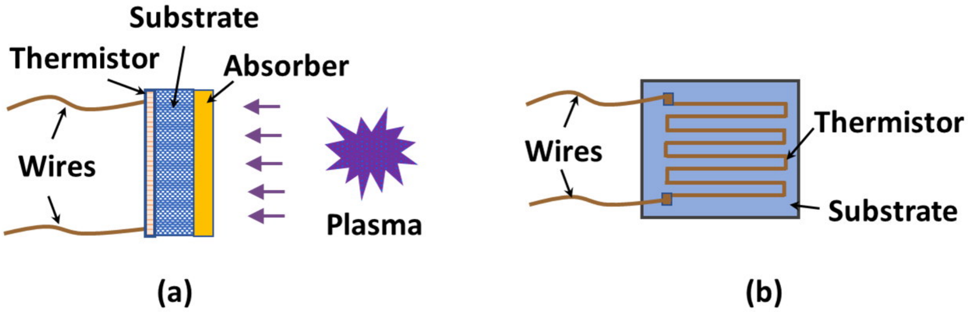

Figure 1.2: Schematic of a resistive bolometer from side view (a) and back view (b), respectively.

The challenges encountering from the resistive bolometers motivated us to develop a fiber-optic bolometer due to the unique advantages of the fiber-optic sensors. First, the optical fiber is made from the dielectric material endowing the fiber-optic sensor with inherent immunity to the electromagnetic interference. Second, the measuring point could locate at a long distance from the light source and the sensor demodulators achieving the remote sensing. Third, the fiber-optic sensor has a small size and light weight allowing large number of fiber-optic sensors integrated together to obtain a compact structure achieving a relative high spatial resolution. Due to these advantages, the special designed radiation-hardened optical fiber has been successfully applied into the MCF system for data transmission and sensing. In addition, the fiber-optic grating sensors have been successfully used for the measurements of strain and temperature in a MCF system. Although, extensive work related to the radiation-hardened fiber used for data transmission or fiber-optic grating sensors used for temperature or strain measurements in MCF has been reported [10–12], there is no fiber-optic bolometer being reported limited from the relative long time constant and low resolution of regular fiber-optic sensors.

In order to develop a fiber-optic bolometer, the development of fiber-optic sensors turned our attention from the fiber-optic grating sensors to the fiber-optic extrinsic Fabry-Perot (FP) interferometric sensors, which is one of the main types of the fiber-optic sensors. The fiber-optic extrinsic FP interferometric sensor consisting of FP cavities fabricated at the tips of the lead-in fiber has received increasing interest in measuring a wide range of parameters, such as temperature [13–15], pressure [16], acoustic and ultrasonic waves [17, 18], flow [19, 20], refractive index [21], and biochemical specifications [22, 23]. Figure 1.3(a) shows a basic structure of a low-finesse fiber-optic extrinsic FP interferometric sensor where the interrogation light output from the lead-in fiber propagates into the FP cavity, and then the light reflected from the front mirror and the back mirror are coupled back into the core of lead-in fiber to form interference fringes. Figure1.3 (b) shows a simulated reflection spectrum (red curve) of a low-finesse fiber-optic silicon FP interferometric sensor [25]. The silicon has a cavity length of 100 $\mu$m and refractive index of 3.4 at infrared wavelength range. If both surfaces of the FP cavity have a higher reflectivity, multiple reflections can be happened in the FP cavity giving rise to narrower reflection fringes and higher demodulation resolution comparing with the low-finesse fiber-optic FP interferometric sensor. Figure 1.3(b) also shows the reflection spectrum (blue curve) of a gold-mirrored high-finesse fiber-optic silicon FP interferometric sensor where the asymmetric of the reflection spectrum is caused by the absorption of the front gold mirror to the interrogation light [30]. More details could be found in **Chapter 2** and **Chapter 4**.

The measured parameters of a fiber-optic FP interferometric sensor could be obtained by encoding the wavelength shifts of the sensor reflection fringes, which are typically obtained using one of the three schemes: a laser whose wavelength is at the slope of the fringes along with a photodetector (intensity interrogation) as shown in Fig.1.4, a broadband source plus a spectrometer (angular interrogation) as shown in Fig.1.5, and a wavelength-scanning laser and a photodetector (wavelength interrogation) as shown in Fig.1.6. For the intensity interrogation, the conventional

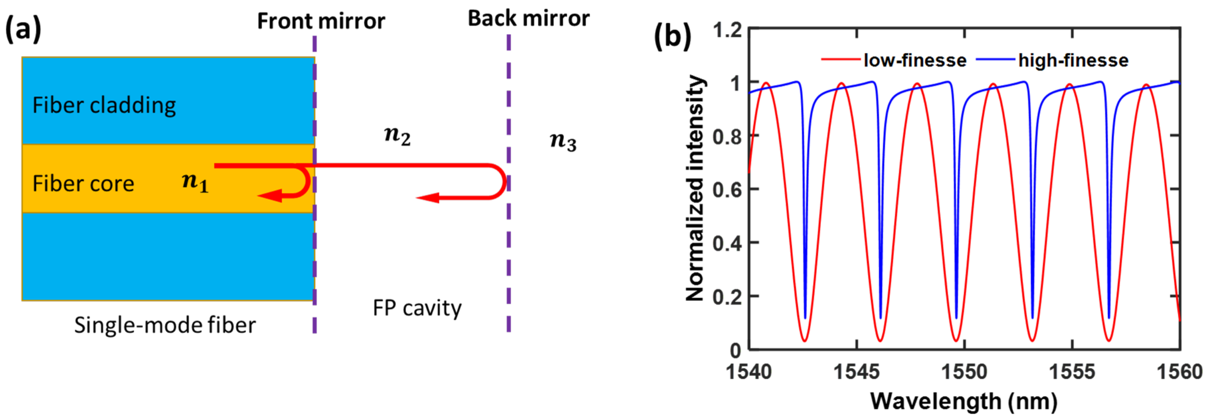

Figure 1.3: (a) Schematic of a low-finesse fiber-optic extrinsic Fabry-Perot interferometric sensor. (b) The reflection spectra of a low-finesse (red curve) and high-finesse (blue curve) fiber-optic silicon FP interferometric sensor.

demodulation system is showed in Fig.1.4 (a). The light output from the laser is delivered into the sensor head first, and then the reflection light is directed into a photodetector via a fiber-optic circulator. In the demodulation, the laser wavelength needs to be tuned to the slope of the sensor reflection fringes. When the sensor wavelength shifts, the measured parameter could be obtained by detecting the reflection signal intensity as shown in Fig.1.4 (b). For the angular interrogation, the demodulation system is similar with the intensity interrogation where the laser and the photodetector are, respectively, replaced by a white light source and a spectrometer as shown in Fig.1.5 (a). A wavelength tracking method based on curve fitting is usually used for the sensor demodulation due to the high demodulation resolution and simple demodulation algorithm. The curve fitting is applied to the data points around the valley or peak to find the wavelength position of the valley or peak of the reflection fringes. Figure 1.5 (b) shows an example of the sensor demodulation based on wavelength tracking method where the data points around the valley are used for the curve fitting to find the wavelength position. The wavelength interrogation method uses a scanning laser to scan the sensor to obtain the reflection spectrum by measuring the reflection signal intensity through a photodetector as shown in Fig.1.6. The measured signal is usually demodulated by using the wavelength tracking method as shown in Fig.1.5 (b).

Compared with other types of fiber-optic sensors, such as the fiber-optic distributed sensors [24], and fiber-optic grating sensors [11], in which most of the reported sensors use optical fiber itself

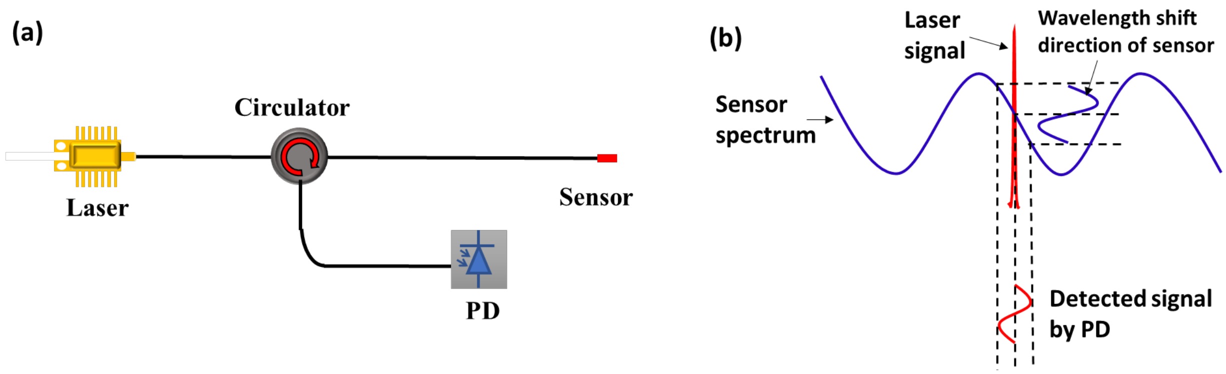

Figure 1.4: (a) schematically shows a intensity demodulation system for a fiber-optic FP interferometric sensor. (b) Wavelength shifts of sensor leads to a variation of the PD signal. PD: photodetector.

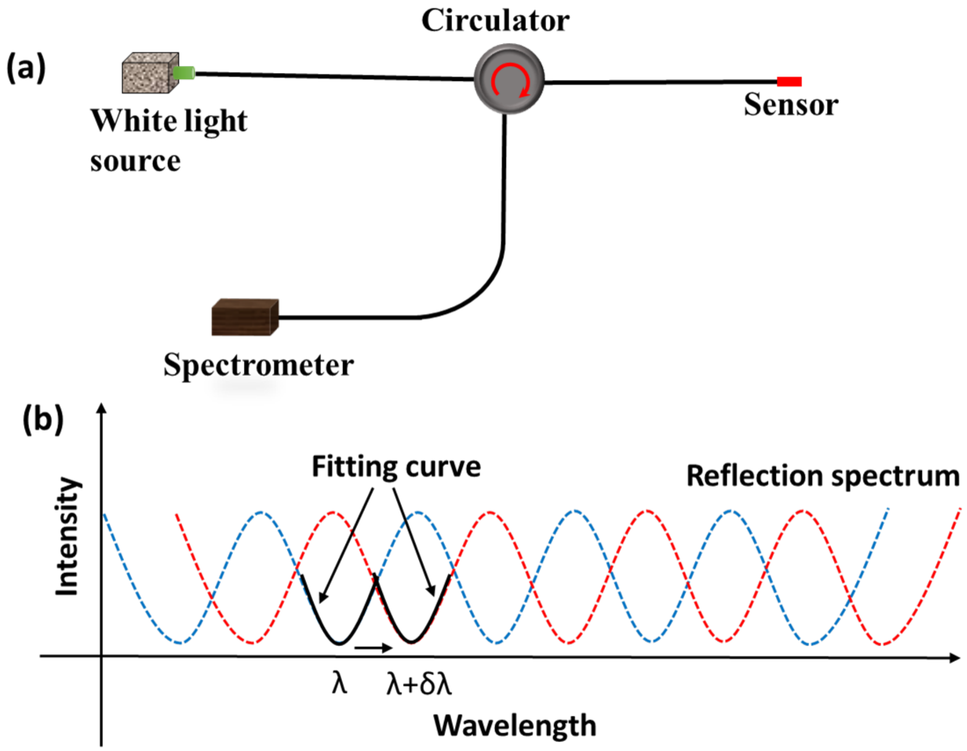

Figure 1.5: (a) schematically shows the angular interrogation system for a fiber-optic FP interferometric sensor. (b) Wavelength tracking demodulation method based on curve fitting.

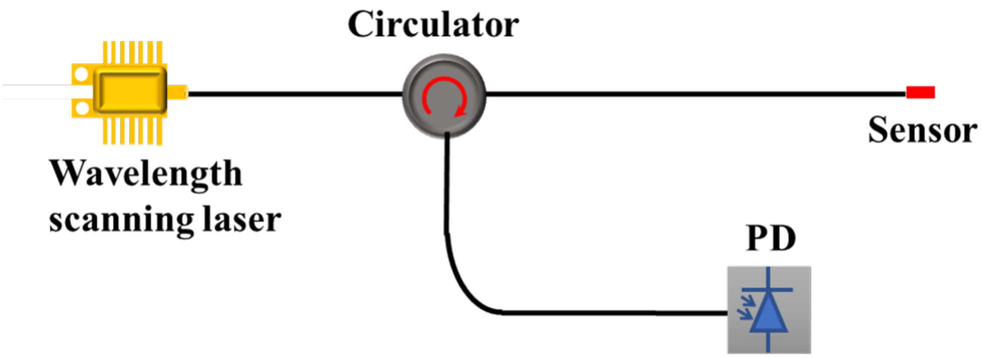

Figure 1.6: schematically shows the wavelength interrogation system for a fiber-optic FP interferometric sensor.

(or silica) as the sensing material, the FP cavities at the tip of the lead-in fiber could choose various of materials, such as silicon, graphene, and so on. Some kinds of materials will provide the sensor with extraordinary performance in the sense of resolution, and response time of sensor or some new functions such as refractive index of solution, and humidity. Recently, Han group demonstrated a high resolution and fast response fiber-optic temperature sensor based on a low-finesse silicon FP interferometer. The sensor consisted of a 200 $\mu$m silicon pillar attached to the end face of a single-mode fiber showed a response time of 150 ms in air, and 0.7 ms in water, and resolution of 0.6 mK [25]. Reinke *et al.* took advantage of this extraordinary sensor demonstrated a fiber-optic bolometer [26]. During the tests, the silicon pillar attached to the end of the lead-in fiber absorbs the incident radiation, and then converts radiation into temperature variation. The power density of the incident radiation was deduced by interrogating the wavelength shifts of the reflection fringes. Initial benchtop tests showed a noise equivalent power density of 5-10 W/m$^2$ which was about 5 times larger than the regular resistive bolometers indicating that more work is needed before a fiber-optic bolometer with comparable or better performance can be obtained comparing with a resistive bolometer.

In this dissertation, our work mainly focused on the development of fiber-optic bolometer based on a silicon FP interferometer to achieve a low noise equivalent power density. Again, the noise equivalent power density is a key metric to characterize the performance of bolometer. We first constructed a simulation model to study the structure parameters of FP cavity influences on the sensor resolution by using Monte Carlo simulations. Then we respectively studied the fiber-optic bolometer based on a low-finesse and a high-finesse silicon FP interferometer. For the low finesse fiber-optic bolometer, we first demonstrated a fast response and high resolution fiber-optic silicon sensor with reduced end conduction effect. Compared with the regular silicon sensor, the response time has an improvement about 6 times. Then we proposed a novel signal processing method based on a modified correlation method to eliminate the spurious jumps encountering in the wavelength tracking demodulation method. This demodulation method showed a very high accuracy in the sensor measurements. For the high-finesse fiber-optic silicon sensor, we first demonstrated a fiber-optic bolometer based on a high-finesse silicon FP cavity. Both of the surfaces of the cavity are coated with high reflection mirrors. The initial benchtop tests showed a noise equivalent power density value of 0.27 W/m$^2$, which is comparable with the conventional resistive bolometer. Then we studied the mechanical vibration and the magnetic field influences on the resolution of the bolometer, both of which can present in a MCF system. To mitigate the influences of vibration and magnetic field,two effective methods were proposed including using bending insensitive fiber to replace the original single-mode fiber, and using the polarization scrambler to randomize the polarization states of the light propagated in the fiber. Finally, we have a short discussion of the future work and make a summary of this dissertation.

## 1.2 Outline of Dissertation

Due to the unique advantages of fiber-optic bolometers, this dissertation mainly focused on how to improve the performance of fiber-optic bolometer including the bolometer theoretical analysis from optics, the bolometer design and fabrication, and the bolometer signal processing. The outline of this dissertation is briefly described and listed below.

**Chapter 2** provides a useful tool to design, fabrication, and interrogating fiber-optic extrinsic FP interferometric sensor, which could also be applied to other kinds of fiber-optic extrinsic FP interferometric sensors. We constructed a simulation model to analyze fiber-optic extrinsic FP interferometric sensor based on polynomial curve fitting and Monte Carlo simulations. In this simulation, we assumed that the whole sensor system worked in a white-noise-limited regime. We respectively studied the structure parameters of FP cavity influences on the sensor resolution including the metal mirror thickness, cavity length, beam width, and wedge angle. Based on the simulation results, we can conveniently change the parameters of a fiber-optic extrinsic FP interferometric sensor to obtained a desired resolution at certain conditions. We also provided a empirical equation which can be used for the resolution estimation just based on the visibility and the bandwidth obtained from the reflection fringes of sensor.

**Chapter 3** focuses on the development of fiber-optic bolometer based on a low-finesse silicon FP interferometer. Time constant is a key parameter to determine the temporal resolution of bolometer. In this chapter, we first demonstrated a high resolution and fast response fiber-optic temperature sensor with reduced end conduction effect. A hollow core microtube was used to cut off the heat transition path from the silicon sensor head to the substrate. The experimental results showed that this new temperature sensor had a response time of 13 ms, which was more than 6 times faster than the regular sensor (13 vs. 83 ms). Then we studied the spurious jumps encountered in the demodulation of fiber-optic bolometer by using the Monte Carlo simulation method. The simulation results show that the spurious jumps arise mainly from the systematic errors of the curve fitting function for modeling the sensor spectrum and manifested by the changes in the pixel set for curve fitting. To overcome this challenge, we proposed a novel signal processing method by using a modified correlation method. Both the simulation and experimental results showed that our new demodulation method had a high accuracy in sensor reading, and the spurious jumps were well eliminated.

**Chapter 4** pays attention to the development of high-finesse fiber-optic bolometers. We initially presents a novel fiber-optic bolometer design and fabrication method. Compared with previously reported fiber-optic bolometer with low finesse silicon pillar, we reduce the cavity length, enlarge the diameter of silicon pillar, and introduce the gold mirror to increase the radiation responsivity of bolometer. In addition to the gold mirror on the top surface of silicon FP interferometer, we introduce multilayer dielectric coating to increase the finesse of the silicon FP interferometer to reduce the noise level of the whole demodulation system. In the experiments, to reduce the common noises from the interrogation light source and the ambient temperature fluctuations, a reference bolometer was introduced into the system. The experimental results show that this novel fiber-optic bolometer has a noise equivalent power density of 0.27 W/m$^2$, which is comparable with the conventional resistive bolometer. Then we demonstrates two methods to mitigate degradation of fiber-optic bolometer in the practical applications. We introduce mechanical vibration and static or quasi-static magnetic field into the fiber-optic bolometer system, which can present in the practical applications. Through the analysis and the experimental results, we find that both the vibration and the magnetic field have strong influences on the noise performance of bolometer attributing to the birefringence of silicon FP interferometer. To mitigate the birefringence effects, we proposed two methods including: polarization maintaining fiber replacing single-mode fiber and polarization scrambling. Experimental results showed that both methods could effectively mitigate the influences from the vibration and the magnetic field showing a promising prospect in the practical application of fiber-optic bolometer.

**Chapter 5** briefly summarizes the work demonstrated in this dissertation and discusses the future work in the development of fiber-optic bolometer.

# CHAPTER 2

# ANALYSIS OF SINGLE-MODE FIBER-OPTIC EXTRINSIC FP INTERFEROMETRIC SENSORS WITH PLANAR METAL MIRRORS

*Contents of this chapter have been submitted to Applied Optics and accepted. Currently, it is in the process of production*

- *Q. Sheng, G. Liu, N. Uddin, and M. Han, "Analysis of single-mode fiber-optic extrinsic Fabry-Perot interferometric sensors with planar metal mirrors," Applied Optics, vol.60, no. 24, 2021.*

The fiber-optic bolometer based on a silicon FP interferometer is actually a fiber-optic temperature sensor consisting of a silicon FP interferometer fabricated at the tips of the single-mode fiber, therefore, in this chapter, we present a model to describe a fiber-optic extrinsic FP interferometric sensor formed by two planar gold films and analyze the effect of key sensor parameters, including the beam width of the incident light, the metal coating film thickness, the FP cavity length, and the wedge angle of the two mirrors, on the visibility and spectral width of the sensors. Due to its superior performance, wavelength interrogation is employed for the sensor where spectrum is measured by a wavelength-scanning laser and the wavelength position of a fringe valley is found by polynomial fitting of the data points around the valley. Through Monte Carlo simulations, we have obtained an empirical equation for estimating the wavelength resolution from the fringe visibility and spectral width for a system with given noise level. The results separate the contributions to the measurement resolution from the system noise and from the sensor structure, which allow to define a figure-of-merit that is inherent to the sensor and independent on the system noises. The model provides a useful tool for the design and fabrication of such sensors. In our analysis, metal films are selected as the mirrors for the FP cavity as opposed to dielectric coatings with both practical and theoretical considerations. On the practical aspect, dielectric mirrors require complicated mirror design, has more stringent requirements on the coating substrate, are much thicker than metal coatings, and have a higher fabrication cost. On the theoretical aspect, the refractive indices of metals are complex numbers. The model for an FP cavity with metal mirrors is more general with consideration of complex reflection and transmission coefficients of the mirrors and can be easily adapted to analyze an FP cavity with dielectric coatings.

## 2.1 Wavelength resolution of extrinsic FP interferometric sensors with Lorentzian lines

We start with a high-finesse extrinsic FP interferometric sensor formed by lossless mirrors, whose reflection spectrum can be approximated by a Lorentzian function (narrow-peak approximation) [27]. Intuitively, the inherent noise performance of the sensor is dependent on the fringe visibility and the spectral width, and a large visibility and a narrower fringe width favor a higher resolution. Analysis of how fringe visibility and width affect the resolution in such a sensor with well-defined spectral shape can provide useful insight on the metal mirrored extrinsic FP interferometric sensors with more complex spectral shapes. Figure 2.1 (a) shows a notch in the reflection spectrum, $I_L(\lambda)$, where the maximum reflectivity is normalized to unity, $I_d$ is the depth of the valley related to the fringe visibility of the sensor, $\delta\lambda$ is the 3-dB spectral width counting from the peak to the valley, and $\lambda$ denotes wavelength. With noise, the measured spectrum is given by

$$I_{rn}(\lambda) = I_L(\lambda) + \delta I \tag{2.1}$$

where $\delta I$ is the relative intensity noise following the normal distribution arising from the sensor system. In practice, the spectrum is sampled and digitalized. Assume the data points are evenly distributed along the notch at a wavelength interval of 1.2 pm (600 pm over 500 data points). For simplicity, we further assume that the noise of any data point is independent, and the noise level (standard deviation) is uniform for all data points. A second-order polynomial function was applied to fit the data points around the valley to obtain the valley position. The data points were chosen by setting a threshold, and those below the threshold were chosen for curve fitting as shown in Fig. 2.1 (a). The threshold defined as the level at one fifth of the peak to valley value ($I_d/5$) above the valley. Monte Carlo simulations were carried out to obtain the standard deviation of the obtained fringe valley position for a given sensor spectrum and noise level, which is defined as the wavelength resolution of the sensor system [28]. We first analyzed the effect of 3-dB spectral width on the

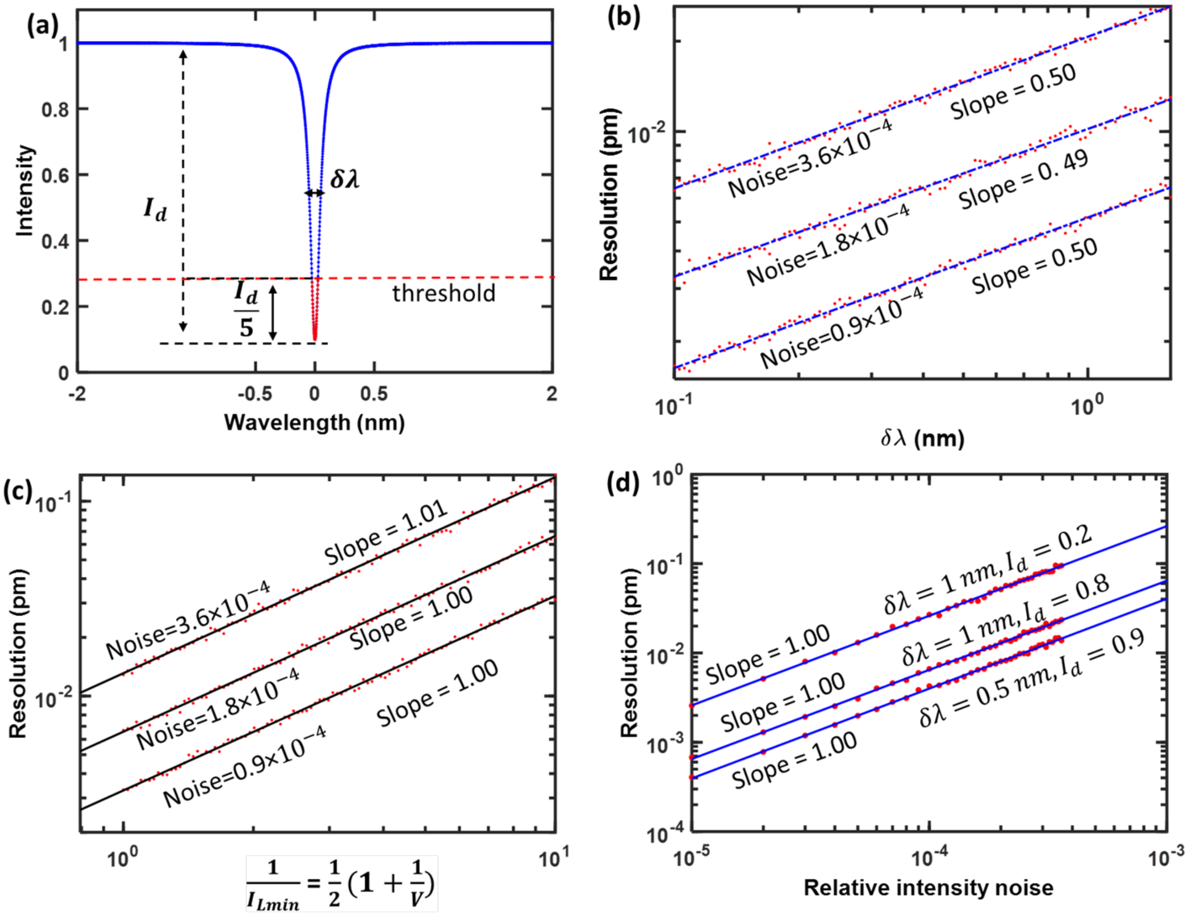

Figure 2.1: Analysis of how fringe visibility and bandwidth influences on the sensor resolution. (a) Simulated reflection notch of sensor. (b) Sensor wavelength resolution vs. 3-dB spectral width ($\delta\lambda$) when the fringe visibility is set at 0.8. (c) Sensor wavelength resolution vs.$(1 + 1/V)/2$ when the 3-dB spectral width is set 0.5 nm. (d) Sensor wavelength resolution vs. relative intensity noise.

sensor resolution. Figure 2.1 (b) shows the sensor resolution as function of the 3-dB spectral width at three different noise levels when the fringe visibility is fixed to 0.8 on the logarithmic scale. The linear fittings of the data points on the logarithmic scale for the three different noise levels show similar slopes close to 0.5, indicating that wavelength resolution is proportional to the square root of the bandwidth $\sqrt{\delta\lambda}$. We then obtained the sensor resolution as function of valley depth ($I_d$) for different noise levels when $\delta\lambda$ was fixed at 0.5 nm, and the result is plot in Fig. 2.1 (c). The linear fittings of data for the three different noise levels show similar slopes close to 1, which reveals that the value of wavelength resolution scales with $1/I_d$ . In practice, fringe visibility, $V$, is more commonly used for characterizing the fringes of an extrinsic FP interferometric sensor, and $1/I_d = (1 + 1/V)/2$. Summarizing the results shown in Fig. 2.1 (b) and (c), we have found that the sensor resolution is proportion to $\sqrt{\delta\lambda}(1 + 1/V)$, which can be used as an figure-of-merit of the sensor. Figure 2.1 (d) shows the sensor wavelength resolution as a function of noise level with different bandwidth ($\delta\lambda$) and depth ($I_d$). As expected, the resolution increases linearly with the relative intensity noise with given bandwidth and depth.

It is worth reminding that the results are obtained for high-finesse extrinsic FP interferometric sensors whose spectrum can be approximated by Lorentzian functions. The spectrum from extrinsic FP interferometric sensors with metal mirrors may be more complex and have large deviations from a Lorentzian shape. Nevertheless, the results indicate that spectral width and fringe visibility are the major parameters that determine the noise performance of an extrinsic FP interferometric sensor.

## 2.2 Optical model of extrinsic FP interferometric sensors with planar metal mirrors

The fiber-optic extrinsic FP interferometric sensor with planar metal mirrors under analysis is schematically shown in Fig. 2.2. Light from an single-mode fiber is expanded by a collimator before illuminating an FP cavity formed by two metal films on both sides of a substrate with thickness of $d_3$ and refractive index of $n_3$. In practice, the collimator can be made from a short section of graded-index multimode fiber [29], whose refractive index can be considered as a constant, $n_1$, for the purpose of calculating the reflection and transmission coefficients of the meal film. The thicknesses of the metal films on the front side ($M_1$) and the far side ($M_2$) of the substrate are, respectively, $d_2$ and $d_4$, and their complex refractive indices are, respectively, $n_2$ and $n_4$. For simplicity, we assume the same metals are used for both mirrors, thus $n_2 = n_4$. The external medium surrounding the sensor is assumed to be air with refractive index of $n_5 \approx 1$. The light beam at the exit of the collimator can be approximated as a Gaussian beam with a plane wavefront whose electric field is given by $E(\rho) = E_0 exp(-\rho^2/\omega_0^2)$, where $E_0$ is the maximum amplitude, $\omega_0$ is the waist radius of the Gaussian beam, and $\rho$ is the radial distance from the center axial of the

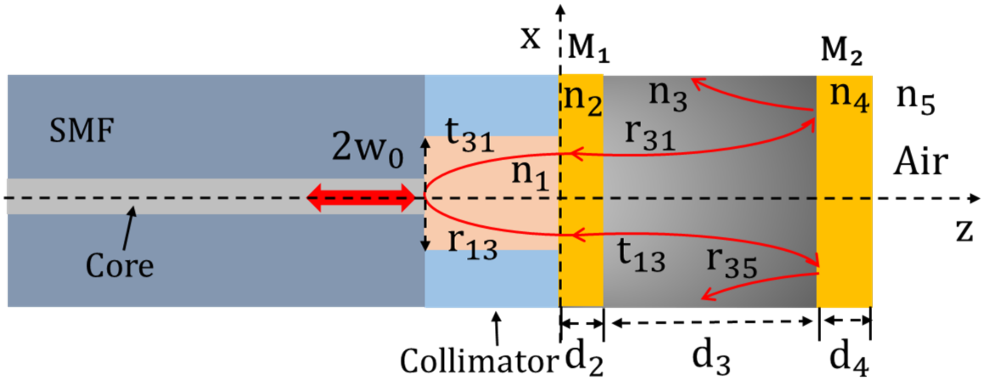

Figure 2.2: Schematic of a fiber-optic extrinsic FP interferometric sensor with planar metal mirrors

Gaussian beam. After transmitting through the metal mirror ($M_1$) into the FP cavity, the electric field of the Gaussian beam travels back and forth between the two mirrors. For each round trip, due to the diffraction of beam that leads to the mismatch from the original Gaussian field, only a part of the backward travelling light can be coupled into the same mode of the collimator that matches the fundamental mode of the lead-in single-mode fiber [30]. The total reflected field coupled into the fundamental mode of the lead-in SMF from the FP cavity is given by

$$E_r = r_{13}E\left(\rho\right) + \sum_{m=2}^{\infty} t_{13}\left(r_{35}\right)^{m-1}\left(r_{31}\right)^{m-2} t_{31}\eta_m E\left(\rho\right) \tag{2.2}$$

where $r_{13}$ ( $r_{31}$ ) and $t_{13}$ ( $t_{31}$ ) are, respectively, the reflection and transmission coefficients of metal mirror $M_1$ calculated from the extracavity (intracavity) side of the mirror, $r_{35}$ is the reflection coefficient of $M_2$ calculated from the intracavity side of the mirror, and $\eta_m$ is the coupling coefficient of the Gaussian beam after the $m^{th}$ round trip in the cavity to the Gaussian beam of the collimator that matches the fundamental mode of the single-mode fiber [31, 32], which is given by

$$\eta_m = \frac{2}{\omega_0\omega'_m q} exp\left(i\phi_m\right), \tag{2.3}$$

where $\omega'_m$ is the spherical wavefront radius of the Gaussian beam after the $m^{th}$ round trip in the cavity, $\phi_m = 2kmd_3 - tan^{-1}\left(2md_3/z_0\right)$ is the phase shift due to wave propagation of the Gaussian beam ( $z_0 = \pi\omega_0^2 n_3/\lambda_0$ is the Rayleigh range of the beam at free-space wavelength $\lambda_0$), and $q$ is a complex number given by $q = \frac{1}{\omega_0^2} + \frac{1}{\omega_m'^2} + i\frac{k}{2R'_m}$, where $k = 2\pi n_3/\lambda_0$ is the wave number, and $R'_m$

is the spherical wavefront radius curvature after the $m^{th}$ round trip in the cavity of the beam. The details could be found in the Appendix.

The reflection and transmission coefficients of the metal mirror, $M_1$, can be deduced using the transfer matrix method [33, 34]. The mirror coated on the end of fiber is sandwiched between the collimator and the FP interferometer. Thus, the transfer matrix of this metal layer can be obtained from

$$\begin{bmatrix} M_{11} & M_{12} \\ M_{21} & M_{22} \end{bmatrix} = \frac{1}{t'_{12}} \begin{bmatrix} 1 & r'_{12} \\ r'_{12} & 1 \end{bmatrix} \cdot \begin{bmatrix} exp(-i\beta_2) & 0 \\ 0 & exp(i\beta_2) \end{bmatrix} \cdot \frac{1}{t'23} \begin{bmatrix} 1 & r'_{23} \\ r'_{23} & 1 \end{bmatrix} \tag{2.4}$$

where $\beta_2 = \frac{2\pi}{\lambda_0} n_2 d_3$, $r'_{12}$ and $r'_{23}$ are the reflection coefficients defined by the Fresnel reflection arising from the refractive index mismatch of two adjacent layers: fiber and metal film, and $t'_{12}$ and $t'_{23}$ are the transmission coefficients. Then the reflection coefficient $r_{13}$ and transmission coefficient $t_{13}$ of metal mirror are

$$r_{13} = \frac{M_{21}}{M_{11}} = \frac{r'_{12} + r'_{23} exp\,(2i\beta_2)}{1 + r'_{12} r'_{23} exp\,(2i\beta_2)}, \tag{2.5}$$

$$t_{13} = \frac{1}{M_{11}} = \frac{t'_{12} t'_{23} exp\,(i\beta_2)}{1 + r'_{12} r'_{23} exp\,(2i\beta_2)}, \tag{2.6}$$

Using the same method, the other three reflection or transmission coefficients, $r_{31}$, $t_{31}$ and $r_{35}$ are obtained and given by

$$r_{31} = \frac{r'_{32} + r'_{21} exp\,(2i\beta_2)}{1 + r'_{32} r'_{21} exp\,(2i\beta_2)}, \tag{2.7}$$

$$t_{31} = \frac{t'_{32} t'_{21} exp\,(i\beta_2)}{1 + r'_{12} r'_{23} exp\,(2i\beta_2)}, \tag{2.8}$$

$$r_{35} = \frac{r'_{34} + r'_{45} exp\,(2i\beta_4)}{1 + r'_{34} r'_{45} exp\,(2i\beta_4)}. \tag{2.9}$$

where $\beta_4 = \frac{2\pi}{\lambda_0} n_4 d_4$. The reflection coefficients and transmission coefficients at the interface of two adjacent layers $r'_{lm}$ and $t'_{lm}$ ($l = 1, \cdots, 5; m = 1, \cdots, 5$), in Eqs. (2.4-2.9) can be calculated using the Fresnel equations given by

$$r'_{lm} = \frac{n_l - n_m}{n_l + n_m}, \tag{2.10}$$

$$t'_{lm} = \frac{2n_l}{n_l + n_m}. \tag{2.11}$$

Substituting Eqs. (2.3) and (2.5-2.9) into Eq. (2.2), the total reflected intensity coupled into the fiber can be obtained by

$$I_{r0} \propto E_r \cdot (E_r)^* . \tag{2.12}$$

where “*” denotes complex conjugate.

## 2.3 Simulation

### 2.3.1 Simulation methodology

We investigated the noise performance of the sensor system following the method described in *Section 2.1.* The reflection fringes in the absence of the noise can be directly obtained by using Eq. (2.12). A noise term is added to find the wavelength resolution through Monte-Carlo simulations.

We validated our model and simulation method by implementing them on a fiber-optic extrinsic FP interferometric sensor and comparing its reflection spectrum and noise performance obtained from simulation and from experimental measurement. The sensor, which has a similar structure as that shown in Fig. 2.2, consists of a gold mirrored silicon pillar attached to the end face of a short section of graded-index multimode fiber that is connected to a lead-in single-mode fiber. The graded-index multimode fiber, when its length is controlled, functions as a collimator to expand the light beam guided by the single-mode fiber. The fabrication processes are similar to those detailed in Ref. [25] and briefly described as follows. A graded-index multimode fiber with a core-diameter of 60 µm was spliced to an single-mode fiber using a fiber fusion splicer. The graded-index multimode fiber was then cleaved to the desirable length using a fiber cleaver with the help of a microscope. Gold coatings were deposited onto both sides of a 100 µm thick silicon wafer by sputtering with estimated coating thickness of 25 nm on the front side ($M_1$) and 100 nm on the far side ($M_2$).

A small fragment of the coated silicon wafer was glued to the cleaved end of the graded-index multimode fiber to complete the fabrication. The red curve in Fig. 2.3 (a) is a single reflection notch of the fabricated silicon extrinsic FP interferometric sensor measured by an optical sensing interrogator (Model: sm125, Micron Optics) based on a wavelength-swept fiber laser. Due to the limited accuracy in characterization and fabrication of the sensor components, fine adjustments of the simulation parameters of the extrinsic FP interferometric sensor are necessary to get similar reflection fringes with the fabricated silicon extrinsic FP interferometric sensor including the gold mirror thickness, cavity length, refractive index of silicon, wedge angle, and beam width. Note that the wedge angle refers to the angle formed by the two planar surfaces of FP cavity (see *Section 2.3.2.3*). These parameters used in the simulation are listed in Table 1 and the resulting simulated spectral notch is shown in Fig. 2.3 (a) (blue curve). It is seen that the reflection notches obtained experimentally and from the simulation have similar visibility of 0.46 and similar FWHM of 380 pm.

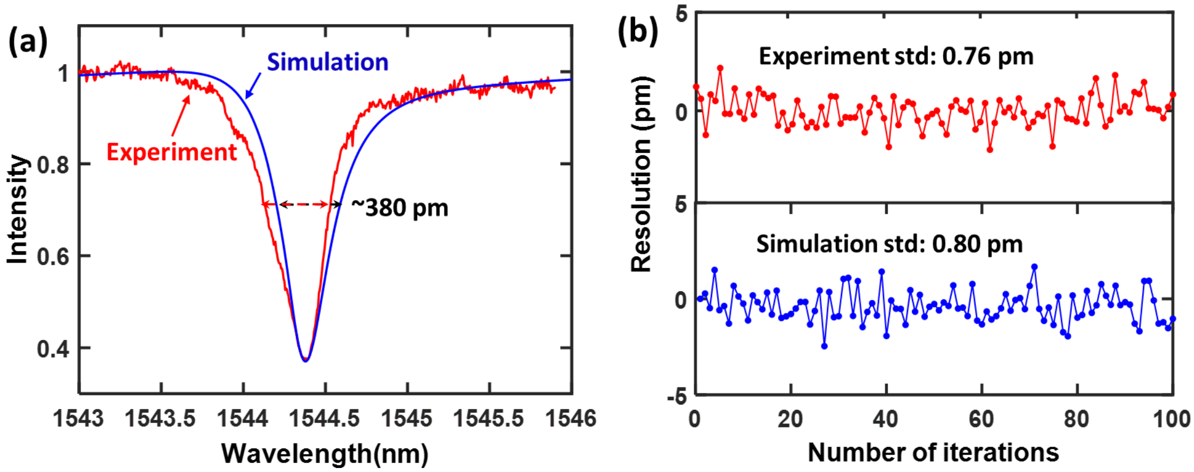

Figure 2.3: (a) A reflection spectral notch of a sensor obtained from the experiment (red) and from the simulation (blue). (b) Standard deviation of the fringe valley position (wavelength resolution) of sensor obtained from the experiment (upper) and the simulation (lower). Std: standard deviation.

Table 2.1: Silicon Extrinsic FP Interferometer Parameters Used in the Simulation

| Parameters | $2\omega_0(\mu m)$ | $d_2$(nm) | $d_3(\mu m)$ | $d_4$(nm) | $n_1$ | $n_2$ | $n_3$ | $\alpha(\circ)$ |
|---|---|---|---|---|---|---|---|---|
| | 20 | 22.5 | 100 | 200 | 1.45 | 0.52+i10.74 | 3.4115 | 0.008 |

The noise performance of the sensor was studied experimentally and compared with the simulation results. Experimentally, the sensor was placed in the lab environment with a constant temperature and its reflection spectra were obtained continuously using the optical sensing interrogator with a frame rate of 1 Hz and wavelength interval between two neighboring data points was 5 pm. For each spectrum, a second-order polynomial function was used to fit the spectrum around a fringe valley and find the wavelength position of the valley. The upper panel of Fig. 2.3 (b) shows the relative fluctuation of the wavelength position for 100 continuous spectral frames obtained from the experiment with a standard deviation of 0.76 pm. For simulation, noise needs to be added to the simulated spectrum of the sensor. With the assumption of an intensity noise with Gaussian distribution, we first needed to determine the standard deviation of the noise used in simulation that should be close to the experimental condition for comparison. Therefore, the fitting errors in the experiment are considered as the relative intensity noise (relative to the intensity of the light at the threshold used for selection of the data for curve fitting) of the system and its standard deviation is calculated to be $6.1 \times 10^{-3}$. In the simulation, independent Gaussian noises with the same standard deviation were added to each data point in each of the spectral frames. After a spectral valley with noise was obtained, polynomial curve fitting was used to find the wavelength position of the fringe valley. The lower panel of Fig. 2.3 (b) shows the relative wavelength obtained from a simulation of 100 iterations. The standard deviation of the result is 0.80 pm, which agree well with the experimental results (0.76 vs. 0.80 pm). The reasonably good agreement between the experimental and simulation results validates the theoretical model and simulation methodology.

### 2.3.2 Simulation results and discussion

As shown in *Section 2.1*, the resolution is largely determined by the fringe visibility and spectral width of the fiber-optic extrinsic FP interferometric sensor. These characteristics are affected by sensor structural parameters such as the thickness of the front gold mirror ($d_2$) beam width ($2\omega_0$), cavity length($d_3$), and wedge angle ($\theta$). In this subsection, we systematically investigate effects of these parameters on the spectral characteristics and measurement resolution of the sensor by using

Monte Carlo simulation method with a given relative intensity noise of $1.8\times10^{-4}$. In the simulation, the data points are evenly distributed along the fringes with a separate distance of 1.2pm.

#### 2.3.2.1 Beam width and thickness of the front gold mirror

We first study the influence of the beam width of the illuminating light on the reflection spectrum of the sensor. We use a silicon extrinsic FP interferometric sensor with a cavity length of 100 µm and a gold film thickness of 30 nm for the front mirror as an example (the thickness of the back gold mirror is kept at 200 nm throughout the simulation). Fig. 2.4 (a) shows the simulated fringes obtained when the sensor is illuminated by Gaussian beams of different beam widths. When the beam width is small (e.g., 10 µm corresponding to a beam width of the mode in a regular single-mode fiber), the reflection spectrum shows a relatively broad and shallow notch, partially due to the diffraction of the beam inside the cavity that reduces both the finesse and the fringe visibility of the FP interferometer. As the beam width increase, the diffraction is reduced, leading to higher finesse and increased visibility. It is seen that as the beam width is larger than  60 µm, the spectral shape of the FP interferometer shows little changes with the beam width, indicating that the diffraction due to the finite beam width can be ignored and the spectral width and visibility approaches to the case where the FP interferometer is illuminated by a plane wave.

Next, we study the effect of the gold film thickness of the front mirror on the reflection spectrum of the sensor with a 100-µm silicon cavity length. We demonstrate how the film thickness affects the shape of the sensor spectrum. For this purpose, we simulate the reflection spectrum of sensors with different gold film thicknesses as shown in Fig. 2.4 (b), assuming that they are probed by a laser with a beam width of 60 µm, which, as discussed above, is sufficiently large to ignore the diffraction of the laser inside the cavity. It shows that both the spectral width and the visibility of the fringes are sensitive to the film thickness. Specifically, the spectral width seems to monotonically decrease as the film thickness increases, whereas the fringe visibility reaches its maximum value close to unity at a specific film thickness around 20 nm. These observations are confirmed in Figs. 2.4 (c) and (d) that show, respectively, the spectral width and fringe visibility as a function of film thickness probed with lasers of different beam widths. Again, the results show that when the beam width reaches 60 µm, the spectral characteristics are largely independent on the beam width. It is also noted that, from Fig. 2.4 (c), larger gold film thickness results in narrower spectral width of the fringes. This is reasonable because larger gold film thickness yields a higher reflection and better energy confinement of the light field inside the cavity for a narrower resonant notch. However, the larger gold film thickness also results in a larger transmission loss of the front mirror, and, toward the thick gold film end, causing a low visibility due to the large mismatch between the beam powers directly reflected from the front mirror and the beam that is transmitted back to the fiber through the film.

It is intuitive that a narrower spectral width and a larger visibility will, in general, favor a better measurement resolution. We use the Monte Carlo simulation to find how the gold film thickness and beam width affect the measurement resolution for silicon FP interferometric sensor with the same cavity length of 100 µm at a given noise level. As an example, we assume that the sensor system noise are white Gaussian noises. Figure 2.4 (e) shows the simulated wavelength resolution as a function of the gold film thickness when the beam widths are 10, 20, 40, 60, and 80 µm. It is seen that the changes of resolution with different beam widths follow a similar trend in the sense that an optimized gold film thickness is found that results in the highest resolution (the value for the resolution is minimum) for a given beam width. When the beam width is larger than 60 µm, the resolution vs. metal film curves largely overlap, another indication that the diffraction due to the finite beam width becomes negligible. In this case, the optimal thickness for the gold film is 23 nm. When the beam width is smaller, the highest resolution occurs at a thinner thickness of gold film. For example, when the beam width is 20 µm, the optimal thickness of the gold film is 12 nm. In general, a larger beam width favors a higher resolution. It is worth noting that when the beam width is 40 µm, the sensor achieves similar resolution as the cases where the beam widths are larger (60 and 80 µm) until the gold film thickness reaches its optimal value around 20 nm. However, as the gold film thick continues to increase from its optimal value, the resolution for the 40 µm beam width starts to get lower than for the cases of 60 and 80 µm beam widths.

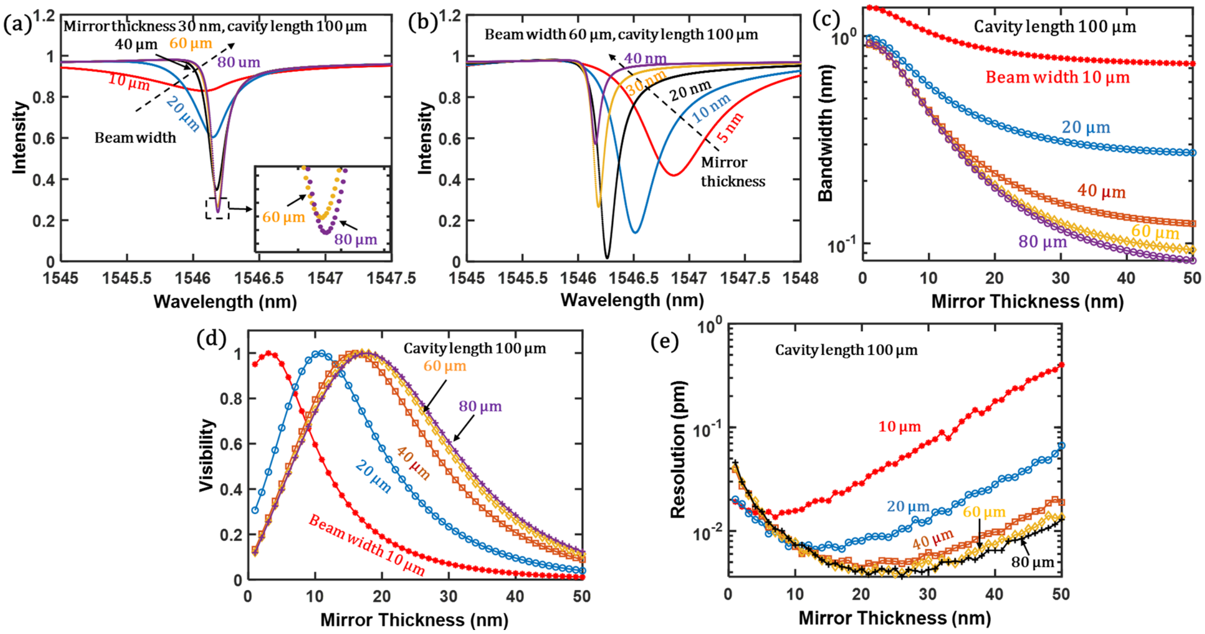

Figure 2.4: Effect of the front gold mirror thickness and illuminating light beam width on the visibility, bandwidth, and resolution of extrinsic FP interferometric sensor. (a) and (b) respectively show the beam width and mirror thickness influence on the reflection spectrum of sensor. (c)-(d) show the sensor bandwidth (c), visibility (d), and resolution (e) as function of mirror thickness with different beam width.

#### 2.3.2.2 Cavity length

We then characterized effect of the length of the FP cavity on the fringe visibility, spectral widths of the fringes, and the wavelength resolution of the sensor system. We set the beam widths to be 60 µm, for which case the beam diffraction can be ignored for a cavity length of 100 µm, as discussed in *Section 2.3.2.1*. Figure 2.5 (a) shows the FWHM width of the reflection spectral fringes as a function of the silicon cavity length for different gold film thicknesses. The spectral width monotonically decreases as the cavity length increases, which is expected because the free-spectral range is inversely proportional to the cavity length. As discussed in *Section 2.3.2.1*, a thicker gold film always leads to a narrower spectral notch at a given cavity length. Figure 2.5 (b) shows the fringe visibility as a function of cavity length for different gold film thicknesses. In general, the visibility does not vary significantly over the range of simulation (10-200 µm). For a 10 nm thick gold film, the visibility shows a slight increase with the cavity length, while for other thicknesses of simulation, the visibility decreases slightly with the cavity length. When the gold film thickness is 20 nm, the visibility is > 95% over the cavity length range. Figure 2.5 (c) shows the wavelength resolution as a function of cavity length, assuming the same noise characteristics as used in *Section 2.3.2.1*. It is seen that the case of 20 nm gold film thickness has a similar resolution with the case of 30 nm gold film thickness for the cavity length below 110 µm. With increase of the cavity length (> 110 µm), the values of wavelength resolution of sensor with the 30 nm gold film become larger than that with the 20 nm gold film. Again, the wavelength resolution is dependent on both the spectral width and the visibility of fringes and a narrower spectral width and higher visibility favor a higher resolution. As shown in Figs. 2.5 (a) and (b), for the case of 20 nm gold film thickness, the spectral width continuously decreases as the cavity length increases and is approximately inversely proportional to the cavity length, the visibility shows an approximately linear decrease with the cavity length. Comparing with the visibility of the 20 nm gold film, the 30 nm film shows a larger decrease of the visibility. In addition to the cases of 20 nm and 30 nm gold film thickness, the similar variation happens to the cases of 10 nm and 40 nm gold film thickness as shown in Fig. 2.5 (c). We also noticed small fluctuations in Fig. 2.5 (c), which are attributed to the variations of the pixel distribution relative to the fringe valley position. Measurement resolution decreases monotonically as the cavity length increases. In practical applications, the maximum cavity length is limited by many factors such as required spatial resolution, required sensor size, and fabrication capability. The simulation has a maximum length of 200 µm for the silicon FP cavity, corresponding to an optical length of almost 700 $\mu$m, which is above the typical cavity length used for a fiber-optic extrinsic FP interferometric sensor.

#### 2.3.2.3 Wedge angle

In practice, due to the limited fabrication accuracy, the two surfaces of FP interferometer may not be perfectly parallel and they may form a wedge angle. It is important to understand the effect of the deviation from the ideal parallelism on the sensor performance. As shown in Fig. 2.6 (a), we assume that the front mirror is perpendicular to the fiber axis (z-axis) of the lead-in fiber and the

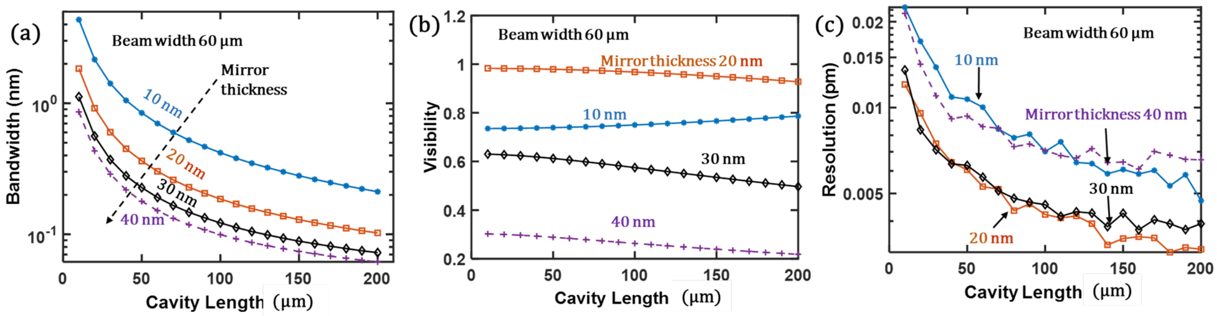

Figure 2.5: The sensor bandwidth (a), visibility (b), and resolution (c) as function of cavity length with different mirror thickness.

mirror at the far end has an angle of $\alpha$ with respect to the x-axis. The wedge results in a lateral and angle mismatch between the intracavity light beam and the optical mode of the fiber at the coupling plane. For the light beam after m round trips in the cavity, the angle and lateral mismatch are $\theta_m = 2m\alpha$ and $d_m = 2m^2 d_3 \alpha$ [31], respectively and the coupling coefficient is given by

$$\eta_m = \frac{2}{\omega_0 \omega'_m q} e^{-p d_m^2 \left(1-\frac{p}{q}\right)} e^{-\frac{k^2 \theta_m^2}{4q}} e^{-ikd_m\theta_m\left(1-\frac{p}{q}\right)} e^{i\phi_m}, \tag{2.13}$$

where $p = q - 1/\omega_0^2$ and $\phi_m = 2mkd_3 - tan^{-1}(2md_3/z_0)$ is the phase due to wave propagation. Substituting $\eta_m$ into Eq. (2.2) and using Eq. (2.12), the reflection spectrum of the sensor is obtained. The details could be found in the Appendix.

In the simulation, we assume that the beam width is 60 μm and the cavity length is 100 μm. Fig. 2.6 (b) shows the spectral width of the fringes as a function of the wedge angle in the range of 0-0.3° for different gold film thicknesses. For larger thicknesses (>30 nm) of the gold film, the spectral width increases rapidly with the wedge angle when the wedge angle is less than 0.2°. For smaller thicknesses of the gold film, the spectral width shows little increase with the wedge angle for small wedge angles and large changes when the wedge angle becomes larger (<0.2°). When the wedge angle is increased to 0.2° or larger, the spectral width is independent on the film thickness. The effect of the wedge angle on the fringe visibility is also dependent on the gold film thickness, as shown in Fig. 2.6 (c). For larger thicknesses ($\geqslant$ 20 nm), the fringe visibility monotonically decreases as the wedge angle increases. For smaller film thicknesses, as the wedge angle increases, the fringe visibility increases first, reaches its maximum value, then start to decrease. This behavior is expected because a very thin gold film for the front mirror has a smaller reflection compared with the thick gold film for the back mirror. As the wedge angle increases, it reduces the coupling efficiency of the light reflected from the back mirror to the fiber and the light beams coupled back to the fiber from both mirrors become more balanced, resulting in a larger visibility. The visibility reaches its maximum value when the two beams are balanced and starts to decrease as the wedge angle continue to increase when the beam coupled to the fiber from the back mirror is weaker than from the front mirror. The simulated wavelength resolution as a function of wedge angle is shown in Fig. 2.6 (d) using the same noise characteristics as in *Section 2.3.2.1*. For large gold film thickness ($\geqslant$ 20 nm), the value of the wavelength resolution rapidly increases as the wedge angle increases. For example, the resolutions are worsened by more than 10 times when the wedge increases to 0.2° from 0 for all three cases with gold film thickness $\geqslant$ 20 nm. For the two small gold film thicknesses (5 and 10 nm), as the wedge angle increases, the value of wavelength resolution decreases initially due to the increased fringe visibility before reaching its minimum value and starting to increase.

#### 2.3.2.4 Resolution estimation

The above analysis shows that the suite of sensor structural parameters including the gold film thickness, cavity length, and wedge angles, as well as the beam size of the interrogation light have a compounding effect on the spectral shapes and the wave resolution of the sensors. It is challenging to analytically relate the structural parameters to the resolution performance of sensors. Enlightened by the analysis and results obtained for sensors with simple Lorentzian spectral shapes in *Section 2.1*, we can obtain an empirical equation relating these two spectral parameters with wavelength resolution which will provide a valuable guideline in the sensor design. Toward this end, we analyze the simulation results obtained in *Section 2.3.2* to relate the wavelength resolution with the spectral width and fringe visibility at a given noise level without considering the sensor structures and beam size of the probe light. First, we group the data according to the fringe visibility, which allows us to plot the resolution as a function of $\delta\lambda$ at different levels of fringe visibility on the logarithmic scale,

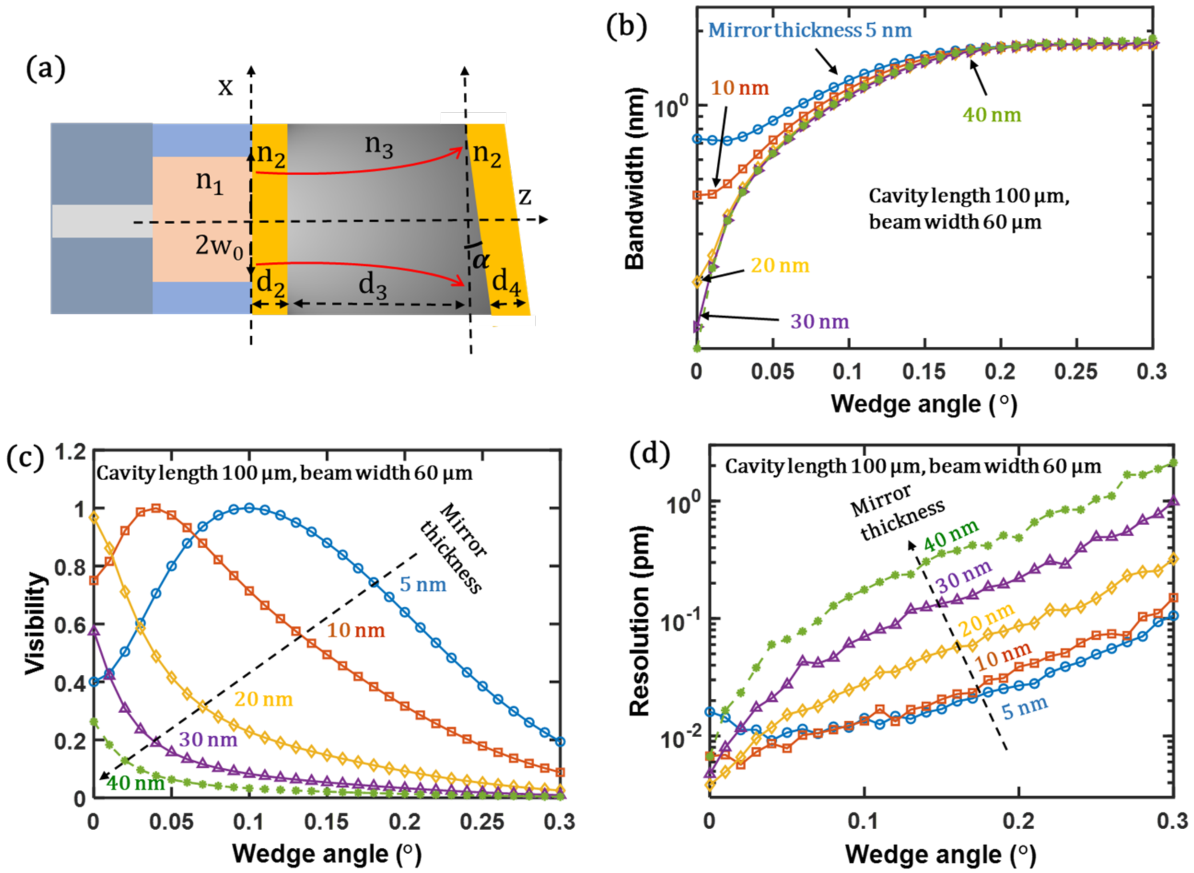

Figure 2.6: The wedge angle influences on the sensor visibility, bandwidth, and resolution with different front mirror thickness. (a) Schematic of a fiber-optic extrinsic FP interferometric sensor with the two gold mirrors forming a wedge angle. (b-d) show the sensor bandwidth (b), visibility (c), and resolution (d) as function of wedge angle for different thickness of the front gold mirror.

as shown in Fig. 2.7 (a). The linear fittings of the data for the three different fringe visibilities show similar slopes close to an average of 0.57. Similarly, we group the data according to the spectral width and scales with $(1 + 1/V)/2$ for a given spectral width as shown in Fig. 2.7 (b).

Combining the observations above, we obtain an empirical equation for estimating the wavelength resolution from the fringe visibility and the spectral width of the reflection fringes:

$$Res = \gamma \frac{\sqrt[0.57]{\delta\lambda}}{2}\left(1 + \frac{1}{V}\right), \tag{2.14}$$

where $\gamma$ is a coefficient determined by the noise level. This empirical equation separates the contributions to the sensor resolution from the system noise ($\gamma$) and from the sensor itself ( $\sqrt[0.57]{\delta\lambda}(1+$

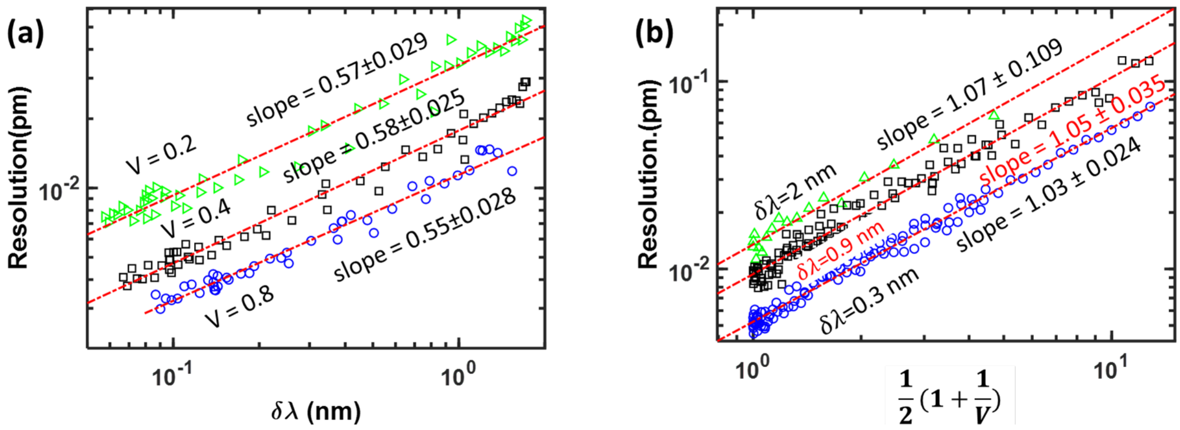

Figure 2.7: (a) Sensor resolution vs. spectral width of the reflection notches with different fringe visibilities. (b) Sensor resolution variation as function of visibility with different bandwidth.

$1/V)/2$). As a result, we can use $\sqrt[0.57]{\delta\lambda}(1+1/V)/2$ as an figure-of-merit for the sensor, which is inherent to the sensor and independent on the system noise. To test the validity of the empirical function, we obtained a set of spectral frames with different combinations of spectral width and fringe visibility randomly adjusted the parameters of the sensor. We then obtained the wavelength resolution of the sensor through Monte Carlo simulations for two different noise levels, which is plotted against $\sqrt[0.57]{\delta\lambda}(1+1/V)/2$, as shown in Fig. 2.8. It is seen that the data points form two clusters according to the noise level and, for each cluster, the data points are distributed along a line, indicating the reliability of the empirical equation in predicting the noise performance of the sensor from the spectral width and the visibility of its reflection fringes.

## 2.4 Conclusion

We presented a model to study the noise performance of fiber-optic extrinsic FP interferometric sensors with planar metal mirrors. In this model, we assumed the sensor is operated in a white noise limited regime, and wavelength interrogation method is applied for the sensor demodulation. To validate our model and simulation method, we use a metal mirrored silicon extrinsic FP interferometric sensor as an example. The simulation and experimental results of the silicon extrinsic FP interferometric sensor agree with each other reasonably well, indicating the validity of the simulation model in the analysis of the noise performance of the extrinsic FP interferometric

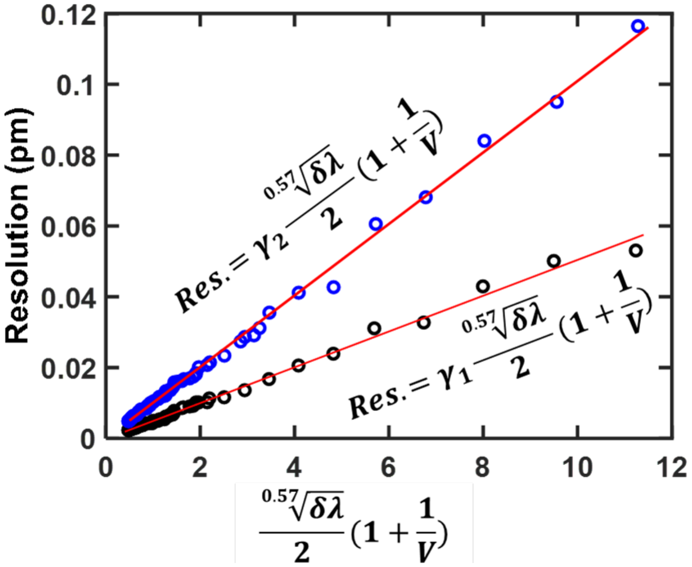

Figure 2.8: Simulated sensor resolution vs. $\sqrt[0.57]{\delta\lambda}(1+1/V)2$ for two different noise levels.

sensor with metal mirrors. Taking advantage of this model, we theoretically studied the effects of key parameters of FP cavity, including the metal mirror thickness, beam width, cavity length, and wedge angle, on the sensor noise performance. Based on the simulation results, we find that the wavelength resolution of the extrinsic FP interferometric sensor is highly dependent on the visibility and the bandwidth of the reflection fringes. We propose an empirical equation for estimating the noise of the sensor system and a formula involving visibility and bandwidth of the reflection notches that can be used as the figure-of-merit to characterize the inherent sensor noise performance. Our work provides a useful tool for designing, constructing, and interrogating fiber-optic extrinsic FP interferometric sensors with metal mirrors.

# CHAPTER 3

# DEVELOPMENT OF FIBER-OPTIC BOLOMETER BASED ON A LOW-FINESSE SILICON FP INTERFEROMETER

*Contents of this chapter have been published in*

- *Q. Sheng, B. Li, N. Uddin, A.F. Mitul, Y. Zhu, Z. Qiu, and M. Han, "High resolution, fast response fiber-optic temperature sensor with reduced end-conduction effect," Optics Letters, vol. 45, pp. 6094-6097, 2020.*
- *Q. Sheng, N. Uddin, and M. Han, "Spurious jumps in wavelength tracking of fiber-optic Fabry-Perot interferometric sensor,"* ***which is currently submitted to Journal of the Optical Society of America B and in the process of peer review****.*

Compared with the high-finesse fiber-optic extrinsic FP interferometric sensor, although the bandwidth of the low-finesse fiber-optic FP interferometric sensor shows a wider bandwidth at FWHM of reflection fringes, the low-finesse fiber-optic FP interferometric sensor is much easier to be fabricated and demodulated, and has lower cost indicating favorable practical application potentials. In this chapter, we mainly focused on the development of fiber-optic bolometer based on a low-finesse silicon FP interferometer.

We first studied the end conduction effect in fiber-optic extrinsic FP interferometric temperature sensors by comparing the performance of two sensor designs. Note that the end-conduction effect has been well studied in the electrical anemometer, but there is no any work being reported in the fiber-optic sensors. In the traditional design, a silicon plate is directly attached to the fiber end face on the large plate surface. We report a new design that has a thin silicon plate with its narrow edge surface standing on the edge of a microtube. Such a design minimizes the heat transfer path to the fiber stub and achieves a long optical path length of the FP cavity while maintaining the small size of the sensing element, resulting in significantly improved measurement speed and resolution. Then we studied the spurious jumps encountering in the wavelength tracking demodulation method.

We report the observation that wavelength-tracking method based on curve fitting and centroid can suffer from random spurious jumps leading to measurement errors in certain conditions. Unlike in the methods to obtain the absolute optical cavity lengths [35,36], these spurious jumps in wavelength tracking are unrelated to the phase ambiguity when the changes of the fringe phase exceed $2\pi$ and little work has been reported to study this research issue. We analyze the origin of the spurious jumps observed in regular wavelength tracking method using Monte Carlo simulations. We show that the jumps are due to the inaccuracy of the fitting function for modeling the measured sensor spectrum and the jumps occur when the pixel set in the spectrum for curve fitting changes. We find that a simple modification of the pixel set for curve fitting can significantly reduce the spurious jumps although it cannot eliminate them. We also show that increasing the density of the pixels for curve fitting can effectively reduce the jumps although this strategy may be impractical in practice as the pixel density is limited in available spectrometers. However, such observation leads us to a modified correlation demodulation method that can effectively remove the spurious jumps without the need to increasing the pixel density. In this method, we calculate the correlation coefficients between the measurement spectral frame and a set of calibration spectral frame, then find the value of the measurand by curve fitting of the correlation coefficients. The calibration frame can be obtained with a high density without much difficulty in practice to remove the spurious jumps from curve fitting. The simulation results and experimental results show that the modified correlation method can effectively eliminate the spurious jumps so that the sensor accuracy is improved.

## 3.1 High resolution, fast response fiber-optic temperature sensor with reduced end conduction effect

### 3.1.1 Sensor simulation and fabrication

An example of the traditional design [25, 37] and the new design of the fiber-optic silicon FP temperature sensors are schematically shown in Fig. 3.1(a) and (b), respectively. In Fig. 3.1(a), a thin silicon plate is directly bonded to the end face of a single-mode fiber. The two large surfaces of the silicon plate form an FP cavity whose cavity length is the thickness of plate. The physical contact between the large plate surface and fiber end face forms an effective heat transfer path between them, resulting in significant end conduction effect. The small cavity length determined by the thickness of the plate leads to coarse spectral fringes of the FP cavity and reduced measurement resolution. Both challenges are addressed in the design in Fig. 3.1(b) where a short section of a fused-silica microtube is sandwiched between the thin silicon plate and the fiber. The silicon plate stands on the edge surface of the microtube with the contact area being the narrow edge surface of the plate. The two opposite narrow edge surfaces of the plate form the FP cavity and the cavity length is the width of the plate, which is much larger than its thickness. The contact area of the silicon plate and the tube in the new design is determined by the thicknesses of the plate and the tube wall, which is significantly smaller than that between the plate and the fiber stub in Fig. 3.1(a) (assuming the plates in both designs are identical), thus effectively reducing the unwanted thermal conduction and suppressing the end conduction effect. The advantage of the new design is further explained through numerical simulation using COMSOL software. We consider identical $130\times25\times5\ \mu\mathrm{m}^3$ silicon plates for the structures shown in Fig. 3.1(a) and (b). The diameter of the solid silica optical fiber is 125 $\mu$m and the inner and outer diameter of the silica tube are 150 and 115 $\mu$m, resulting in contact areas of 3250 and 75 $\mu\mathrm{m}^2$, respectively, for the two designs. Additionally, we consider the case where the plate is directly glued to the fiber on the thin edge with a contact area of 650 $\mu\mathrm{m}^2$. In all cases, the sensor is placed in air and the silicon plate is heated on the top surface with a 2 mW radiation starting at time t=0. The normalized time history of the volume average temperature of the plate is obtained and shown in Fig. 3.1(c). As expected, the new design with the silica tube shows the fast response with a time constant of 19 ms and the traditional design has the slowest response with a time constant of 122 ms, while the case with intermediate contact area shows an intermediate time constant of 103 ms. The simulation proves the importance of minimizing the contact area to reduce end conduction for improved sensor speed and the effectiveness of the new design in achieving this. Besides, using the two edge surfaces of the plate to form the FP cavity also leads to significantly larger cavity length than the traditional design without increasing the overall size of the sensing element, resulting in denser spectral fringes and improved measurement resolution. Note that, in this new design, the plate may be considered as a slab waveguide with lateral confinement to the optical field in one dimension. It is further noted that, another air FP cavity is formed by the end face of the lead-in fiber and the bottom edge surface of the thin silicon plate separated by the fused-silica microtube. As a result, the reflection spectrum of the sensor with the standing plate may have a complicated pattern. However, due to the small thermal expansion coefficient ($5.5 \times 10^{-7} K^{-1}$) of fused silica, the temperature sensitivity of the air FP cavity is negligible compared with the silicon FP cavity (0.85 pm/K vs. 85 pm/K at 1550 nm). Therefore, the fringes from the air cavity can be considered as a static background of the fringes from the silicon FP cavity. It is worth noting that the sensor of the new design may not be suitable for application in liquid environment as the optical signal and thermal transfer may be affected by the liquid trapped in the tube. We fabricated sensors of both designs and compared their performances. The fabrication steps for the new design are outlined in Fig. 3.2 (a)-(f). The fabrication started with the preparation of the silicon comb-teeth by using the deep ion reactive etching. The comb-teeth consist of multiple identical thin silicon cantilevers as shown in Fig. 3.2 (a). Each of the teeth (plates) has a length of 130 $\mu$m, a width of 25 $\mu$m, and a thickness of 5 $\mu$m. An SEM image of multiple successfully etched silicon comb-teeth is shown in the inset of Fig. 3.2 (a). A fused-silica microtube with an outside diameter of 150 $\mu$m and a wall thickness of 35 $\mu$m was spliced to the end face of a SMF; then the microtube was cleaved using a fiber cleaver under a microscope to a short length (110 $\mu$m in this case), resulting a structure as shown in Fig. 3.2 (b). Next, a thin layer of UV glue was spin-coated on a glass slide and a small amount of glue was transferred to the cleaved end face of the microtube by pressing the microtube to the thin glue layer on the glass slide. Note that only half of the end face of microtube was pressed to the glue to prevent the glue from flowing into the microtube, as shown in Fig. 3.2 (c). Next, with the help of a microscope, the end face of microtube with the glue was pressed onto the edge surface of one of the silicon plates shown in Fig. 3.2 (a). In the meantime, the reflection spectrum from the silicon plate was monitored in real time using a broadband light source and a spectrometer. The relative position between the microtube and the silicon plate was carefully adjusted until good fringes from

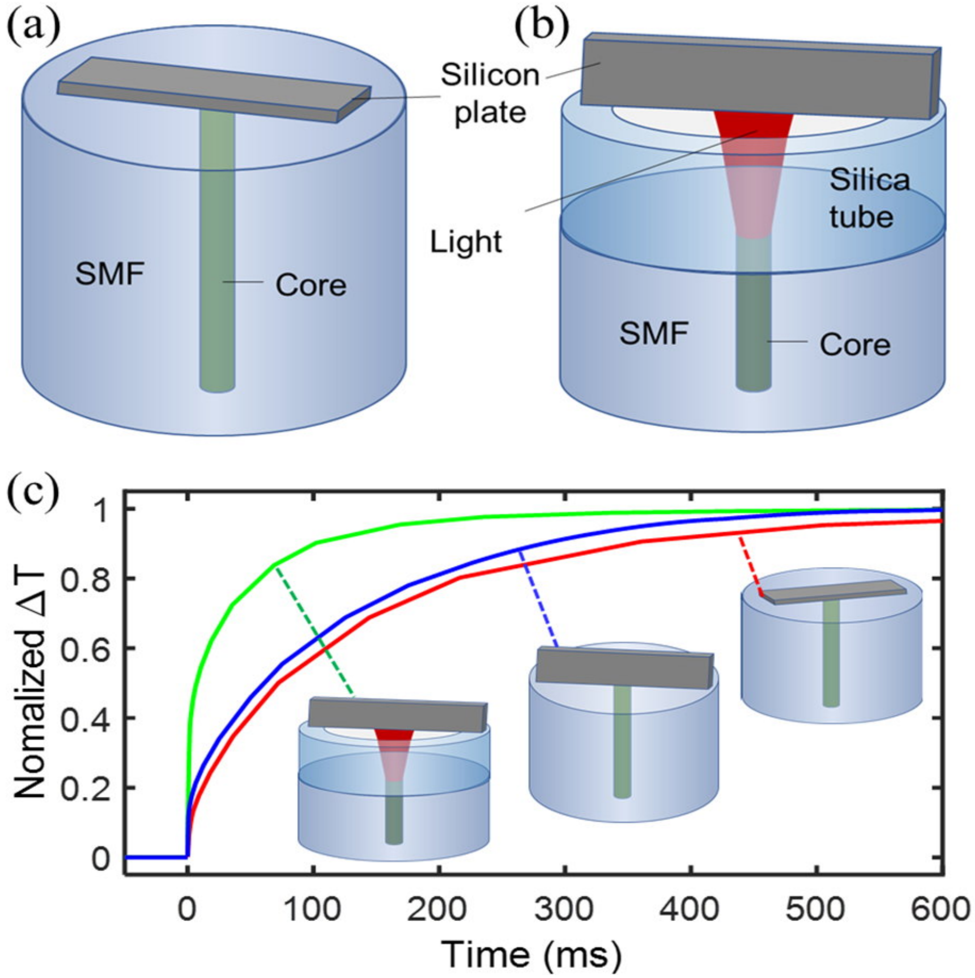

Figure 3.1: Schematics of two FP temperature sensor designs. (a) Traditional design with the silicon plate lying on the fiber end face; (b) new design with the silicon plate standing on the edge of a fused-silica microtube to minimize end conduction and increase the FP cavity length. (c) Numerical result of normalized volume average temperature versus time for three sensor structures with different contact areas.

the silicon plate were obtained by the white light system. The UV glue was cured by applying UV light as shown in Fig. 3.2 (e). After the glue was fully cured, the optical fiber was slowly pressed down to break the suspended silicon cantilever off from its substrate, as shown in Fig. 3.2 (f), to complete the fabrication. An SEM image of a fabricated sensor of the new design is shown in Fig. 3.2(g). For the sensor of the traditional design, several silicon cantilevers shown in Fig. 3.2 (a) were broken off from the substrate. Using similar approaches described above, UV glue was transferred to the end face of the fiber and one of the plates was glued to the fiber end face. An SEM image of the fabricated senor of the traditional design is shown in Fig. 3.2(h).

The red curve in Fig. 3.2 (i) is the measured reflection spectrum of the silicon FP sensor with reduced end conduction, which is a superimposition of the spectra from the cascaded FP cavities of the air gap and the silicon plate. In practice, ultra-short tubes or angle-polished fiber end could be used to reduce the effect on the spectrum from the air gap. The reduced tube length will have additional benefit of increasing the optical coupling between the fiber and the silicon plate. To distinguish the reflection fringes from the silicon FP cavity and the air FP cavity corresponding to the microtube, after the fabrication step shown in Fig. 3.2 (b), we obtained the reflection spectrum of only the air cavity by pressing the end face of the microtube onto a silver mirror and the fringes are shown as the black curve in Fig. 3.2 (i). Note these fringes were being used only for identifying the positions of the valleys and peaks from the air cavity of the sensor. By comparing the fringes of the air FP cavity and the fringes from the overall sensor structure, we can identify fringe features (valleys or peaks) attributed only to the silicon FP cavity for wavelength tracking. We notice the reflection notch closed to the wavelength of 1545 nm on the black curve in Fig. 3.2 (i) (indicated as the "tracking notch") whose shape is largely unaffected by the microtube air cavity. In addition, we notice that the reflection spectrum of the silicon FP cavity has a distortion from the sinusoidal shape, which is attributed to the multimode interference of the silicon FP cavity as the plate functions as a multimode slab waveguide. Such distortion has also been observed in interferometers formed by multimode fibers [38]. The blue curve of Fig. 3.2 (i) is the reflection spectrum of the sensor with the traditional design. Only one broad spectral valley is observed in the measurement wavelength range between 1510-1590 nm due to the small cavity length and this valley was used for wavelength tracking.

### 3.1.2 Sensor response time measurements

We used a high-speed white light system, as shown in Fig. 3.3, to study the step responses and measurement resolutions of the sensors. Through an optical fiber circulator, the light from a superluminescent diode was sent to the sensor and the reflected light was directed to a spectrometer with a frame rate of 3 kHz. Because of the challenges in generating a fast change of the ambient

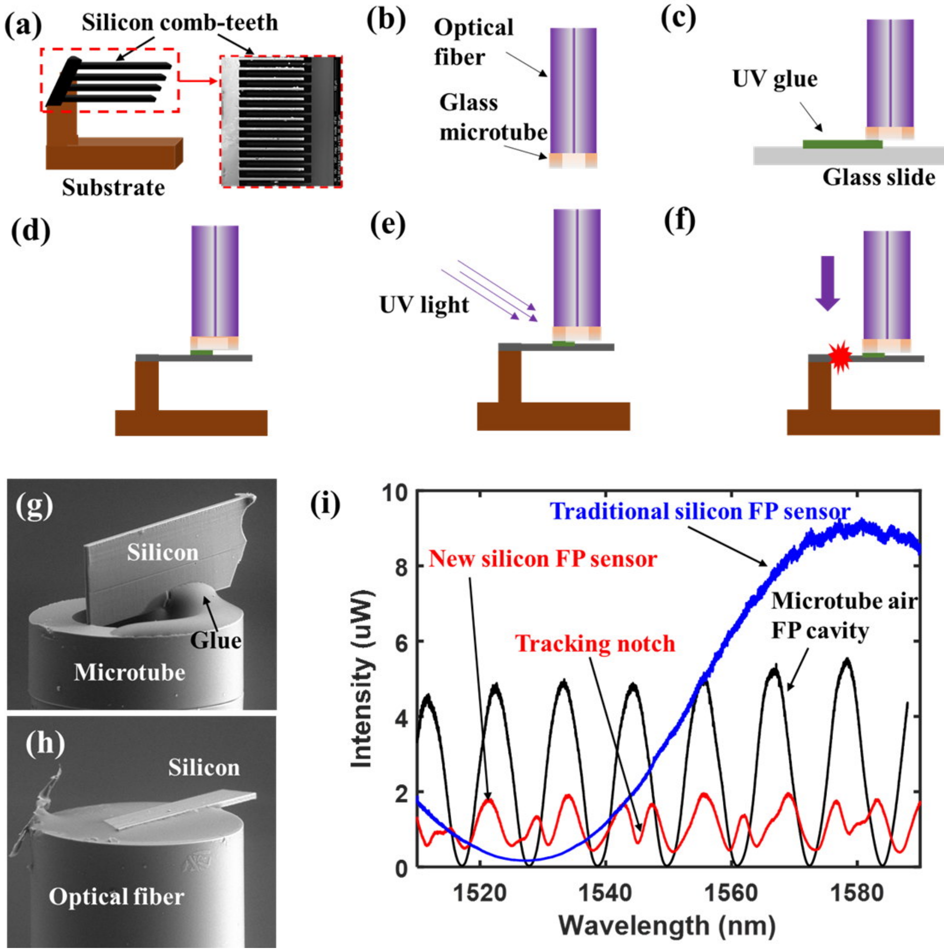

Figure 3.2: (a) – (e) Fabrication processes for the silicon sensor with a standing silicon plate on the microtube. (g) and (h) SEM images of a fabricated silicon FP sensor of the new design (g) and a fabricated traditional silicon FP sensor (h). (i) the reflection spectra of the two sensors and the FP cavity corresponding to the microtube.FP: Fabry-Perot.

temperature in a controllable way for sensor testing, we simulated the step changes in the ambient temperature by heating the sensor with modulated laser radiation. A fiber-pigtailed 980 nm diode laser was used for this purpose to illuminate the sensor head that was placed at a distance of 2 mm to the exit of the fiber. The sensor was heated by the optical absorption of silicon to the laser. For each of the sensors, the position of the fringe valley used for analysis was found by a 2nd-order polynomial fitting. Wavelength shift was transformed to temperature variation using a sensor sensitivity of 84.6 pm/K [25].

Figure 3.4 (a) shows the time history of the step responses for both sensors to the laser radiation

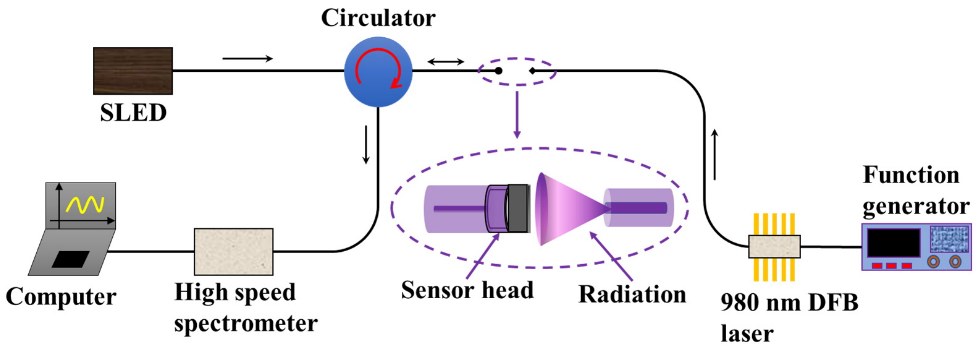

Figure 3.3: Experimental setup to characterize the step responses and measurement resolutions of the silicon FP temperature sensors. FP: Fabry-Perot

modulated with a 0.25 Hz square wave. The laser beam was pointed to the silicon plate of the traditional design at an angle to achieve similar acceptance areas for both sensors; as a result, their temperature rises were similar after reaching thermal equilibrium. To compare the transient response of the two sensor designs, we obtain the normalized signals around the falling edges of step responses and the results are shown in Fig. 3.4 (b). It is seen that the sensor of the new design drops much faster than the sensor of the traditional design due to the reduced end conduction effect. However, the end conduction has not been completely removed in the sensor of the new design as evidenced by the long tail of its step response, which we attribute to the end conduction from the fiber stub that has a much slower thermal response. Although these sensors may not be considered as a simple first order linear system, to numerically compare the speed of the two sensors, we define the characteristic response time as the time needed to reach 63% of the overall signal change. The characteristic response time for the sensor with reduced end conduction is 13 ms, which is more than 6 times faster than the sensor of traditional design (83 ms), proving that the reducing end conduction is critical in improvement of the sensor speed.

Besides faster response, the sensor of the new design is expected to have improved measurement resolution due to its larger FP cavity length. We characterized the noise performance of the sensors by placing the sensors in a sealed box at room temperature and continuously measuring the temperature over a period of 10 s at sampling rate of 3 kHz. The results are shown in Fig. 3.4 (b). The sensor of the traditional design shows a standard deviation value of 0.15 K, while the value for the sensor of the new design is 0.012 K, representing 12 times improvement.

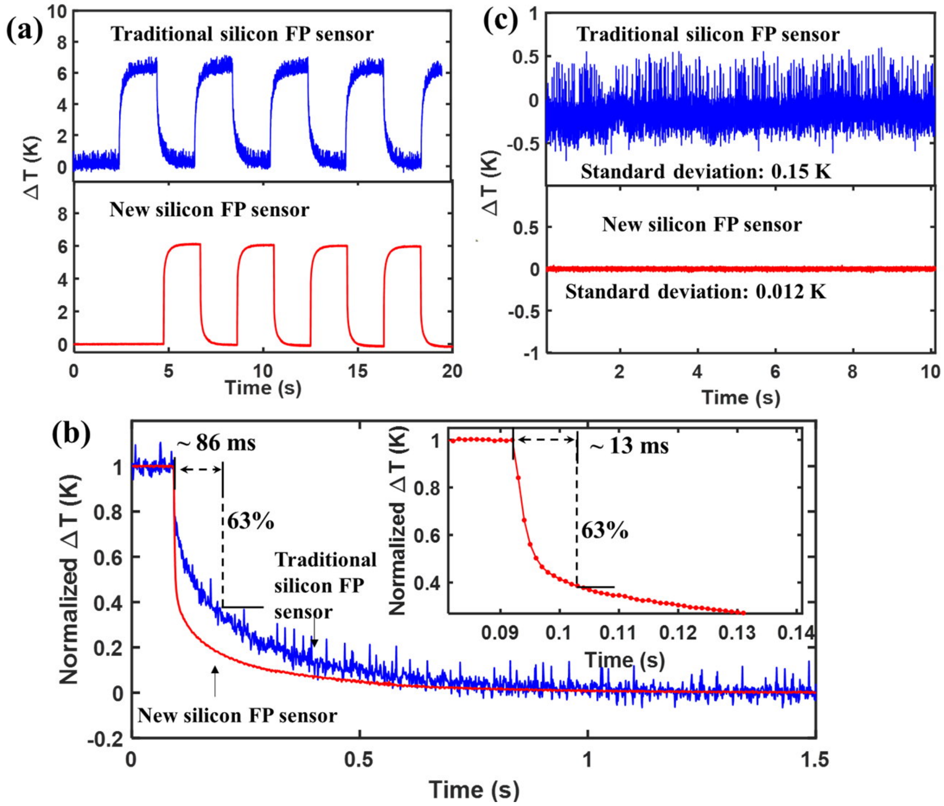

Figure 3.4: (a) Step responses of the two sensors with different designs to the laser radiation modulated by a square wave. (b) Normalized signals of the sensors around the falling edge of the step responses in (a). (c) Noise performance of the sensors.

### 3.1.3 Frequency response measurements

Finally, we characterized the transfer function of the sensors by exciting the sensors with sinusoidally-modulated laser radiation at different frequencies and obtaining the time response of the sensors. Because the limitation in the frame rate of the white light system, intensity interrogation based on a laser and a photodetector, shown in Fig. 3.5, was implemented. We tuned the wavelength of a tunable laser to the spectral slope of the spectral fringes of the sensors. The same reflection notches used in the wavelength interrogation as shown in the inset of Fig. 3.5 were selected. The wavelength shift of the reflection notch caused by the temperature variations of the sensor was converted to intensity variations that were captured by the photodetector. Comparing the modulation signal and the output signal of the system, both the amplitude and the phase of the transfer function of the sensors were obtained. The Bode plot of the transfer function is shown in Fig. 3.6 (a) for amplitude and Fig. 3.6 (b) for phase. The sensor with the reduced end conduction shows a broader bandwidth than the one of the traditional design. Notes that the transfer functions of both sensors differ from those of first order linear systems, indicating that end conduction cannot be ignored even for the sensor of the new design.

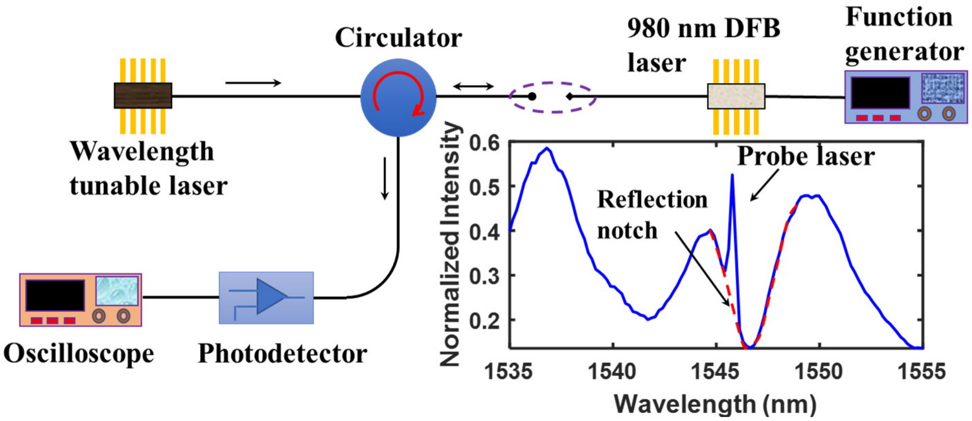

Figure 3.5: Experimental setup to characterize the transfer functions of the sensors. The inset shows the wavelength of the tunable laser relative to the fringes of the sensor with reduced end conduction.

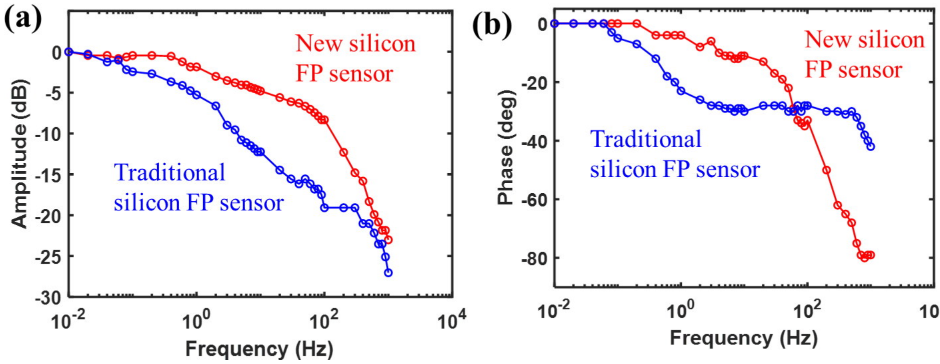

Figure 3.6: (a) Amplitude and (b) phase of the transfer functions of both sensors.

### 3.1.4 Conclusion

In summary, we report a silicon FP temperature sensor with fast response and high resolution by reducing the end conduction and increasing the FP cavity length while maintaining the small size of the sensing element. The sensor is constructed by connecting the narrow edge surface of the silicon plate to the edge of the microtube attached to the fiber tip. Compared to the traditional design where the plate is attached to the fiber end face on its large plate surface, the new sensor minimizes the heat transfer path to the fiber stub and increases the cavity length for improved sensor speed and resolution. Sensors of both designs were fabricated using identical silicon plates, and their performances were compared. We show that, compared to the traditional design, the new design has a characteristic response time that is more than six times faster (13 ms versus 83 ms) and a measurement resolution more than 12 times better (0.012 K versus 0.15 K). Our results show that the end conduction effect, which has not been considered in fiber-optic temperature sensors, is important in the design and application of such sensors for high-speed measurement of temperature.

## 3.2 Spurious jumps in wavelength tracking of fiber-optic FP interferometric sensor

### 3.2.1 Simulation and analysis of demodulation jumps in wavelength tracking method

#### 3.2.1.1 Simulation of reflection spectrum

We consider a low-finesse FP interferometric sensor with a cavity length $L$ and cavity refractive index $n$ interrogated by an incoherent light source, such as a superluminescent diode or a fiber amplified spontaneous emission source, along with a spectrometer consisting of a diffraction grating and a linear photodiode array. Assuming the photodiode array has $N$ pixels and the output from each of the pixels can be expressed as

$$F\left(\lambda_i\right) = \left(I_0 + \Delta I\right)\left[1 + \nu \cdot sin\left(\frac{4\pi nL}{\lambda_i}\right)\right], i = 1, 2, \cdots, N, \tag{3.1}$$

where $I_0$ is proportional to the power spectral density of the light source, $\Delta I$ represents the noise, $\lambda_i$ is the optical wavelength of light illuminating the $i^{th}$ pixel, and $\nu$ refers to the visibility of reflection fringes of the FP sensor. For convenience, we assume that the light source has a uniform spectral profile so that $I_0$ is a constant. The noise properties of superluminescent diode and the fiber amplified spontaneous emission source resemble those of a thermal source and the noise of the photodiode output, $\Delta I_i$ can be modeled by a white Gaussian random process with zero mean [39]. In the simulation, the values of the parameters in the model were set to be consistent with those observed in experiment. Specifically, the spectrometer (Model: I-MON 512 USB, Ibsen Photonics) used in the experiment has $N = 512$ pixels approximately evenly distributed over the wavelength range from 1510-1595 nm; the standard deviation of $\Delta I_i/I_0$ is set to $1.1 \times 10^{-3}$; and the FP sensor is a silicon pillar with $n = 3.4$ and $L = 40\mu m$ ($nL = 136\mu m$) attached to the end of a fiber.

#### 3.2.1.2 Spurious jumps analysis

For simulation of the regular wavelength tracking method, the wavelength position of a fringe valley is obtained by fitting the measured spectrum. Note that, although a sinusoidal function with a constant amplitude [Eq. (3.1))] is used for modeling the reflection spectrum of the sensor, in practice, it is difficult to obtain a mathematical model that can accurately describe the measured reflection spectrum. Measured spectral fringes of a sensor can be complicated by many factors such as the non-uniform spectral profile of the light source, the multi-path interference in the FP cavity, fiber bending, and spectral modulations from other optical devices in the optical path. As a result, the measured spectrum can significantly deviate from a sinusoidal form. Here, we use a polynomial function, which has been widely used in wavelength tracking method, to fit the spectrum simulated using Eq. (3.1). The difference between the fitting function (polynomial) and the function used to generate the spectrum (sinusoidal) represents the systematic errors of modeling the measured spectrum in practice. The polynomial fitting was implemented in two slightly different ways (referred to as "without interpolation" and "with interpolation). In both ways, a threshold for the valley depth is set and the pixel points around the valley whose intensity readings are below the threshold are processed. For the curve fitting without interpolation, second-order polynomial fitting is directly applied to the selected set of pixels to find the valley position. For the curve fitting with interpolation, linear interpolation is used on the first pixel below the threshold and the adjacent pixel above the threshold to generate a new pixel whose intensity equals the threshold, and this new pixel replaces the first pixel in the original set. Similarly, linear interpolation of the last pixel below the threshold in the original set and the adjacent one above the threshold is used to generate a pixel with intensity equal to the threshold to replace the last pixel in the original set. The process ensures that the pixel sets used for curve fitting will have the same range of intensity. As shown below, the curving fitting with interpolation can significantly reduce the spurious jumps compared with the case without interpolation. However, curve fitting with interpolation cannot eliminate the jumps. The choice of the threshold needs to have a good number of data points for curve fitting. In the simulation, the threshold was set at approximately half the maximum intensity of the fringes. In general, the resolution is not sensitive to the threshold over a large range. Figure 3.7 (a) shows a spectral frame simulated using Eq. (3.1) and the pixels used for the polynomial fitting to find the wavelength position of a fringe valley. Figure 3.7(b) shows an example of the pixels around the valley being used for curve fitting (with or without interpolation). In this case, a total of 25 pixels (from #226 to #250) are below the threshold and selected to obtain the valley position. For curve fitting with interpolation, linear interpolation of pixels 225 and 226 in the original set is used to generate a new pixel (red dot 226) on the threshold line that replaces the first pixel in the original set (blue circle 226). Similarly, linear interpolation of pixels 250 and 251 in the original set lead to a new pixel (red dot 250) on the threshold line to replace the last pixel in the original set (blue circle 250). We carried out Monte Carlo simulations for the case where the sensor is under a static state where the cavity length of the sensor is constant. To study the effect of changes in the selected pixels for curve fitting, we intentionally set the threshold for selecting the pixels for curve fitting close to the intensity measured by one of the pixels. As a result, intensity variations from the noise could cause the pixel to cross the threshold line and changes the selected pixels in the set for curve fitting. Figure 3.7 (c) shows the results of the wavelength shifts obtained from curving fitting with (black) and without (blue) interpolations from 500 continuous iterations. The results show a pattern of small fluctuations around the zero line within 1 pm with a few random large jumps of ∼2 pm for curving fitting with interpolation and of ∼6 pm for curve fitting without interpolation. Although curve fitting with interpolation can greatly suppress the spurious jumps, it cannot eliminate the problem as these jumps are still a factor-of-two higher than the fluctuation range absent these jumps

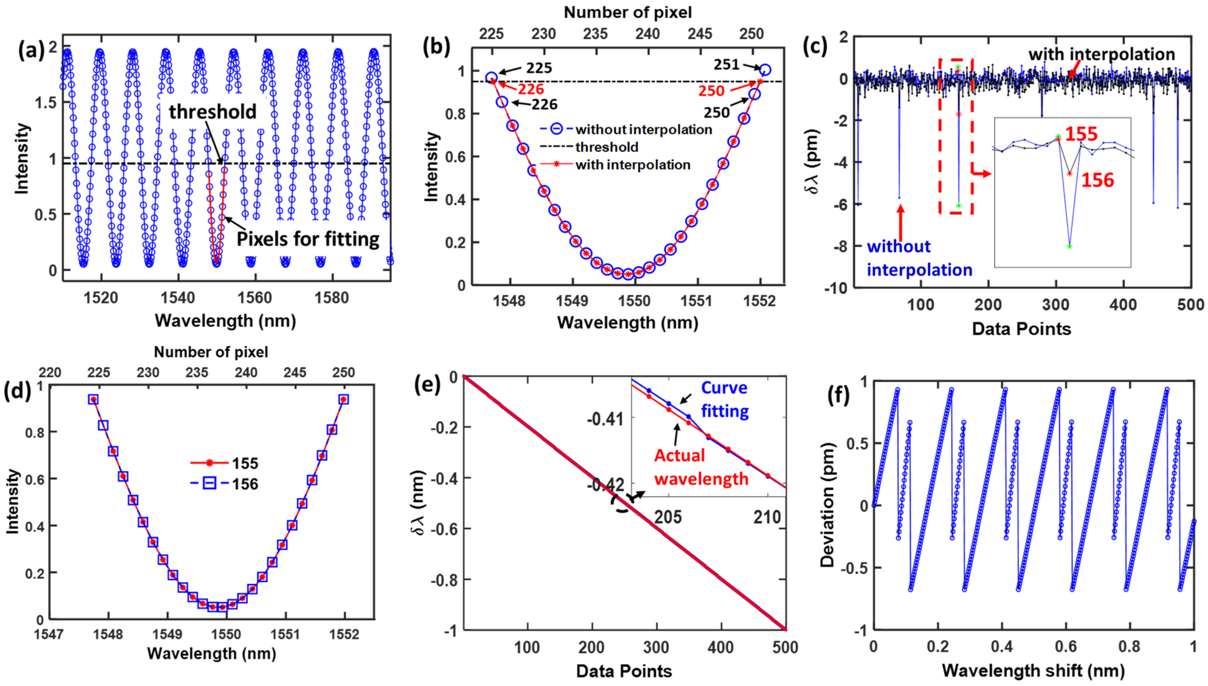

Figure 3.7: (a) Simulated spectral fringes from a sensor with optical cavity length of 136 $\mu$m (red curve shows the pixels used to find the wavelength of fringe valley used in wavelength-tracking method). (b) Pixel set used for wavelength tracking with interpolation (red dots) and without interpolation (blue circles). (c) Relative wavelength of the fringe valley obtained by curve fitting with interpolation (black dots) and without interpolation (blue dots) when the sensor is under static state. (d) Pixel sets used for the curve fitting for the signal jumps shown in the insets of (c). (e) Demodulated wavelength shift and actual wavelength shift when the sensor is under a dynamic state. Inset: enlarged view of a small wavelength deviation. (f) Demodulation error vs. wavelength shift.

(baseline noise). The baseline noise is due to the intensity noise of the light source, while the large jumps are mainly from the changes in the pixel sets used for curving fitting. For example, a jump occurs between data points 155 and 156 [see inset of Fig. 3.7 (c)], and the pixel sets to obtain the two data points are shown in Fig. 3.7 (d). Specifically, for data point 155, the intensities measured by pixels 225-250 are below the threshold, and therefore are used for curve fitting (with interpolation) to obtain that data point 155. It shows a relative wavelength shift less than ∽1 pm from the zero baseline. However, for the spectral frame to obtain data point 156, due to the intensity noise, pixel 224 crosses the threshold and is excluded in the set for curve fitting. Because of the inaccuracy of the fitting function for modeling the spectrum (the polynomial function does not match exactly the actual spectrum), the change in the pixel set for curve fitting leads to a relatively large change in the valley position of the fitting function with a relative wavelength shift of ∽2 pm from the zero baseline.

In the static state, the large jumps only occur when the threshold intensity is close to the intensity measured by a pixel so that the intensity noise can cause the changes in the pixel set for curve fitting. It should be noted that, for measurement of dynamic signals, large jumps can occur even without noise. As the spectral fringes of the sensor shift with the signal, the light intensity measured by a pixel varies and may cross the threshold to change the pixel set for curve fitting. We simulated this scenario by assuming that the sensor fringes shift toward the lower end by 1 nm with a step of 2 pm. Figure 3.7 (e) shows the relative wavelength shifts demodulated from a fringe valley by using the wavelength tracking method (polynomial fitting with interpolation) for the case without noise (blue dots). The red dotted line is the actual wavelength shifts assigned in the simulations. An enlarged view shown in the inset of Fig. 3.7 (e) clearly shows the deviation of the demodulated wavelength shift from the actual wavelength shift. Figure 3.7 (f) shows the difference between the demodulated wavelength shift and the actual wavelength shift as a function of the actual wavelength shift, which reveals the periodic nature of the spurious jumps. The jumps have a period of ∽0.167 nm, consistent with the pixel wavelength spacing (86 nm / 512 pixels), which verifies that the jumps are due to systematic errors of curve fitting function manifested by the changes in the pixel sets for curve fitting.

In general, the change in the pixel set involves the addition and/or removal of a single pixel at either or both edges of the set. Intuitively, the signal jumps caused by these changes may be reduced by increasing the pixel density of the spectral frame to increase the number of pixels in the set for curve fitting, because the effect of adding and/or removing a single pixel has less effect on the fitting results in a set with denser and larger number of pixels. Using the Monte Carlo simulations, we studied the relationship between the standard deviation of the fitting results (a measure of sensor resolution) and the pixel density in two extreme conditions. In one of them, the pixels in the set for curve fitting are fixed, giving rise to the smallest standard deviation (highest resolution) without any spurious jumps. The resolution is determined only by the intensity noise of the light source.

In the other condition, the set for curve fitting changes by a single pixel for each iteration, resulting in the highest standard deviation (lowest resolution) from the large spurious jumps. The results are shown in Fig. 3.8. It is seen that the standard deviation of the fitting results reduces as the pixel density increases in both conditions. When the pixel density is low, the standard deviation from the spurious jumps is much larger than that from the intensity noise. As the pixel density increases, the differences become smaller and eventually the two curves converge, indicating that the effect of changes in the pixel set on the fitting results becomes negligible compared with effect of the intensity noise. Note that irregular pattern observed in the curve for the spurious jumps (blue circles) toward the lower end of the pixel density (in terms of pixel number per unit free spectrum range) is attributed to the variations of the pixel distribution relative to the fringe valley position.

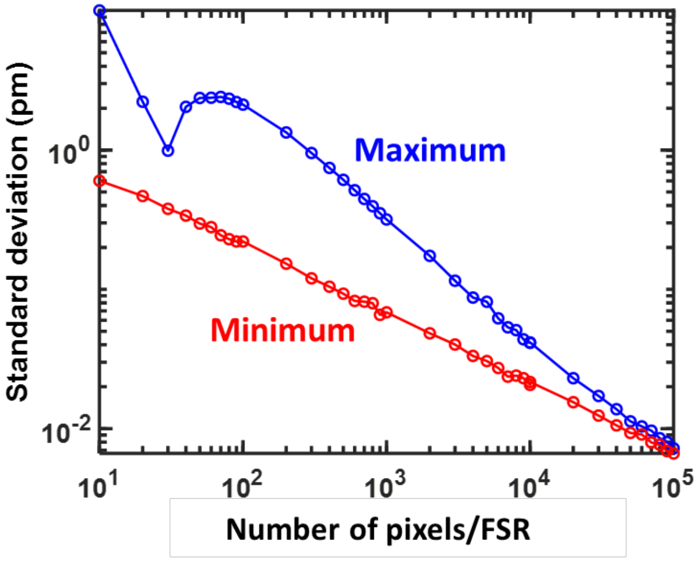

Figure 3.8: Standard deviation due to the intensity noise only (red) and the signal jumps only (blue) vs. pixel density. FSR:free spectrum range.

### 3.2.2 Modified correlation demodulation

Although the spurious jumps may be reduced to a negligible level by increasing the pixel density for curve fitting to a sufficient level, the pixel density of practical spectrometers is limited and usually far from reaching the required density level (e.g. the spectrometer used in our experiment has a pixel interval of 168 pm). Here, we propose and demonstrate a signal demodulation method that does not have spurious jumps even for spectral frames with relatively sparse pixels. It is a modified version of the correlation demodulation methods reported previously. Briefly, the method involves first obtaining a series of calibration spectral frames of the sensor with respect to the measurand, then calculating the similarity between a measured spectral frame and the calibration spectral frames using the correlation coefficient as a function of the measurand; and finally find the peak position of the correlation using curve fitting to obtain the value of the measurand. As the number of the calibration frames in a given range of the measurand can be made sufficiently high without much difficulty in practice, spurious jumps from the change in the data set for curve fitting can be eliminated, as verified by both the simulation and the experimental results. The results also show that the modified correlation demodulation method can also provide a higher resolution comparing with the regular wavelength tracking method in many cases.

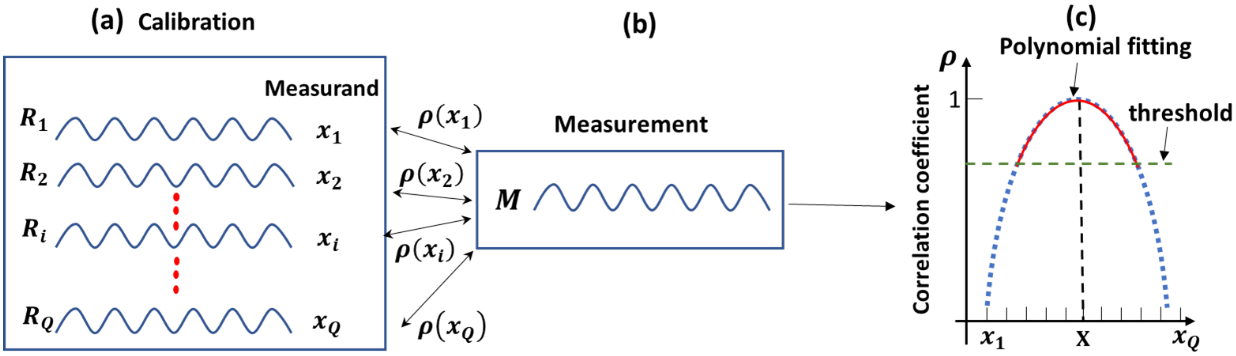

Figure 3.9: Signal processing process of the proposed correlation demodulation method. (a) Obtain calibration spectral frames with sufficient density over a specified range of the measurand; (b) take a measurement frame and calculate its correlation coefficients with the calibration frames; and (c) find the peak position of the correlation coefficient vs. measurand.

#### 3.2.2.1 Demodulation process and algorithm

The demodulation process and algorithm are illustrated with the help of Fig. 3.9. The modified correlation demodulation method requires the calibration of the sensor by recording a series of reflection spectral frames of the sensor as the measurand, denoted by $x$, is varied over a specified range. Assume that the set of calibration spectra contain a total of $Q$ frames, denoted by $R_i$

$(i = 1, 2, \cdots, Q)$ measured at $x = x_i$. Each spectral frame has $N$ pixels so that we can write $R_i = [R_{i1} R_{i2}, \cdots, R_{iN}]$, where $R_{i,j} (j = 1, 2, \cdots, N)$ denotes the light intensity measured by the $j^{th}$ pixel in the $i^{th}$ calibration frame. Figure 3.9 (a) depicts such a set of calibration frames.After the calibration, the sensor is ready for measurement of the intended parameter. Assume that, during the measurement, the sensor system obtains a spectral frame, denoted by $M = [M_1, M_2, \cdots, M_N]$ as shown in Fig. 3.9 (b), from which the value of the measurand,$X$, need to be extracted. To do so, we obtain the correlation coefficients between the measured frame, $M$, and the each of the calibration frames, $R_i$,defined as

$$\rho\left(M, R_i\right) = \frac{1}{N-1} \sum_{j=1}^{N} \frac{\left(R_{ij} - \bar{R}_i\right)\left(M_j - \bar{M}\right)}{\sigma_i \sigma} \left(i = 1, 2, \cdots, Q\right), \tag{3.2}$$

where $\bar{R}_i$ and $\sigma_i$ are, respectively, the mean and standard deviation of $i^{th}$ calibration frame $(R_i)$; and $\bar{M}$ and $\sigma$ are, respectively, the mean and the standard deviation of measured spectral frame $(M)$. Therefore, for a single spectrum of measurement spectral, a total of $Q$ correlation coefficients can be obtained following a parabolic distribution. The value of $\rho\left(M, R_i\right)$ quantifies the similarity between the measured frame, $M$, and calibration frame, $R_i$. Noting that $R_i$ is the spectral frame obtained when the measurand $x = x_i$, we can consider $\rho$ as a function of $x$ given at discrete values of $x_i$ $(i = 1, 2, \cdots, Q)$ as shown in Fig. 3.9 (c). The value of the measurand $(X)$ corresponding to the measured frame is the value of $x$ at which $\rho(x)$ is maximum. The peak position can be found by the curve fitting of $\rho\ (x)$ using, e.g., a polynomial function [also shown in Fig. 3.9 (c)]. Compared with the curve fitting method, the demodulation method proposed here used the discrete correlation coefficients for curve fitting instead of the pixel points around the valley in the measured spectra frame. The density of the data points for curve fitting in this method can be controlled and increased during the calibration process (e.g. by manipulating the sampling rate and/or the change rate of the measurand). As a result, the spurious jumps from the modeling error in the curve fitting can be reduced.

The outline of the demodulation process is shown below.

*Step 1*: Obtain a set of calibration spectral frames, $R_i$, of the sensor corresponding to the values of the measurand,$x_i (i = 1, 2, \cdots, Q)$. The number of the calibration frames in a given range of the measurand need to be sufficiently large to avoid the spurious jumps.

*Step 2*: Take the measurement and obtain the sensor spectra. Assume $M$ is one of the measurement frames from which we need to find the value of the measurand.

*Step 3*: Calculate the correlation coefficients between $M$ and $C$ and the result is a set of $Q$ numbers, $[\rho_1, \rho_2, \cdots, \rho_Q]$, representing the function of $\rho(x)$ evaluated at $x_i (i = 1, 2, \cdots, Q)$.

*Step 4*: Find the peak position of $\rho(x)$ using curve fitting and the peak position is the value of the measurand corresponding to the measured spectral frame $M$.

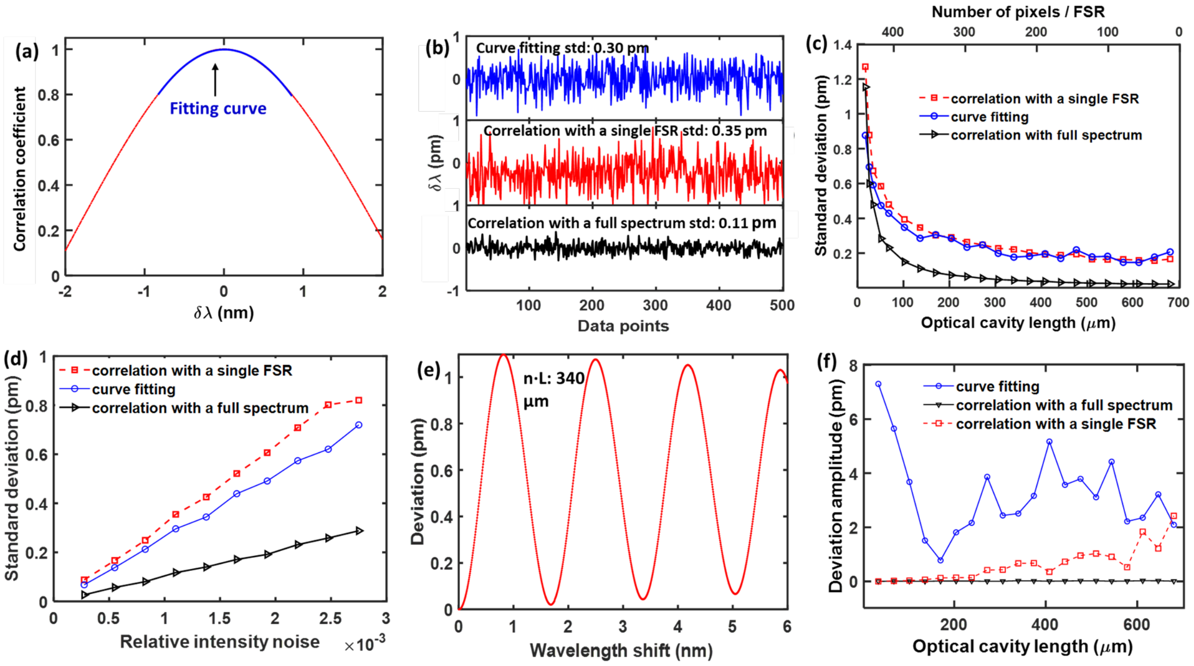

Figure 3.10: (a) correlation coefficients as function of relative wavelength shifts. (b), (c), and (d) are, respectively, the relative wavelength shifts demodulated using the curve fitting method (blue curve), correlation method with a single FSR (red curve), and correlation method with a full spectrum (black curve). (e) An example of wavelength deviation when the optical cavity length is 340 $\mu$m. (f) Wavelength deviation amplitude demodulated by the curve fitting method (blue curve), correlation method with a single FSR (red curve), and correlation method with a full spectrum (black curve). L: optical cavity length; n: refractive index of cavity; and FSR: free spectrum range.

#### 3.2.2.2 Simulation

We simulated the proposed demodulation process using Monte Carlo method for a sensor and interrogation system identical to those given in *Section 3.2.2*. The calibration spectral frames and measurement frames were obtained using Eq. (3.1). For calibration, varying the value of the measurand is equivalent to shifting the wavelength of a fringe valley. By changing the wavelength over a 4 nm range with a step of 0.4 pm, we obtained a set of calibration spectra with $Q = 1 \times 10^4$ frames, each having $N$=512 pixels approximately equally spaced between 1510-1595 nm. Similar to the analysis of spurious jumps in *Section 3.2.2.2*, we studied the performance of the demodulation for both static and dynamic measurements. For the static case, 500 measurement frames were obtained for simulation when the optical cavity length was 136 $\mu$m. For each frame, its correlation coefficient with each of the calibration frame was calculated and a total of $1 \times 10^4$ correlation coefficients over the 4 nm wavelength range were obtained. Figure 3.10 (a) is an example of the correlation coefficient vs. relative wavelength shift from a measurement. The peak position of the correlation coefficient, which was obtained by applying a polynomial fitting, is the relative wavelength shift of the fringe valley in the measured spectral frame. Figure 3.10 (b) shows the result for 500 measurement spectral frames (red curve). For comparison, results from curve fitting method (blue curve), are also shown. Note that no spurious jumps are observed in this case because the threshold was chosen so that the pixel set for curve fitting remained unchanged. The fluctuations in the results are due to the intensity noise of the light source. We point out that only the pixels within a wavelength range equal to the free spectrum range were used in the correlation demodulation, and a single valley was used in the curve fitting demodulation. In this case, the curve fitting method shows slightly better performance than the modified correlation method (standard deviation: 0.30 vs. 0.35 pm). We found that the noise performance of the modified correlation method can be improved by increasing the number of pixels being used for obtaining the correlation coefficients. The noise performance obtained by using the full spectrum (black curve) is also shown in Fig. 3.10 (b) (black curve). Compared with the case of using the pixels in a free spectrum range, the full spectrum demodulation shows a much better noise performance (0.11 vs. 0.35 pm).

We then studied the effect of sensor cavity length and laser intensity noise level on the sensor noise performance for both the curving fitting method and the modified correlation method (including one FSR demodulation and full spectral demodulation). We started with a static test where there are no spurious jumps. Figure 3.10 (d) shows the sensor resolution (standard deviation) as a function of the optical cavity length (lower horizontal axis) or pixel density (upper horizontal axis) when the relative intensity noise was $1.1 \times 10^{-3}$. The standard demodulation decreases as the optical cavity length increases in the simulated range of 17-680 $\mu$m. Compared with the curve fitting demodulation, the one free spectrum range correlation demodulation shows slightly worse noise performance at shorter cavity lengths and comparable performance at longer cavity lengths, while the full-spectrum correlation demodulation exhibits significantly improved noise performance that is consistently better than the curve fitting method throughout the cavity length range. Figure 3.10 (d) shows the sensor resolution as a function of the relative intensity noise when the optical civility length is 136 $\mu$m. As expected, the standard deviation increases linearly with the relative intensity noise for both demodulation methods. Again, the full-spectrum correlation demodulation shows the best noise performance, while the performance of the curve-fitting demodulation is slightly better than the one free spectrum range correlation method. We then simulated a dynamic case where the

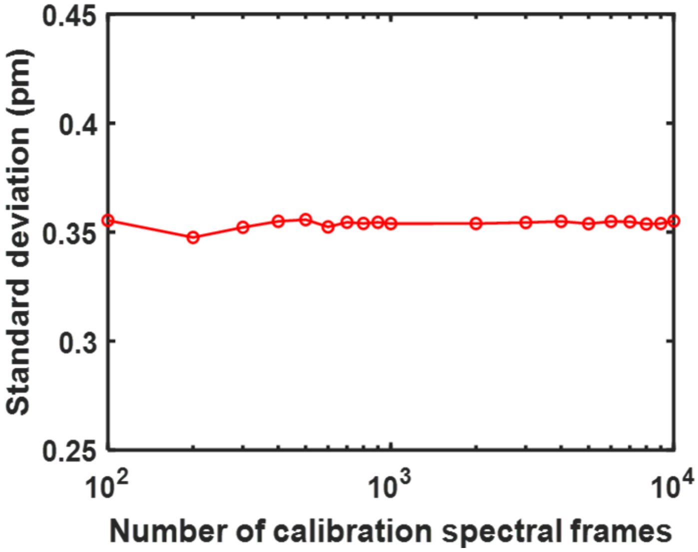

Figure 3.11: Standard deviation (std) vs. number of calibration spectral frames.

spectrum of a noise-free sensor with an optical cavity length of 340 $\mu$m shifted toward the longer wavelength by 6 nm with a step change of 6 pm, giving rise to 1000 measurement spectral frames. Figure 3.10(e) shows the deviation of the demodulated wavelength shift from the actual wavelength shift from the results of one free spectrum range correlation demodulation. The deviation is a smooth and sinusoidal-like form, as opposed to the abrupt jumps from the curve fitting method [see Fig. 3.7(f)]. The period of the deviation from the correlation method corresponds to the free spectrum range of the sensor, rather than the pixel wavelength spacing as in the curve-fitting method. The deviation would be translated to measurement errors in practical applications. Fig. 3.10 (f) shows the deviation amplitude, defined as the peak-to-peak wavelength deviation and representing the maximum measurement error, as a function of the optical cavity length. It is seen that, in general, the deviation from the single free spectrum range correlation method is much smaller than that from the curve fitting method, and the full-spectrum correlation shows further significantly reduced deviation amplitude throughout the cavity length range, indicating that, compared with the curve fitting method, the modified correlation demodulation not only eliminates the spurious jump, but also has inherently higher accuracy.

As shown in Fig. 3.8, the noise of the results from the curve fitting in the regular curve fitting method can be reduced by increasing the pixel density in the curve fitting. One may wonder whether the noise of the results from the correlation method could be reduced by increasing density of the calibration spectral frames. Figure 3.11 shows the simulation results for the standard deviation of the results from correlation method as a function of the number of calibration spectral frames in a static test. Note that the data point set for curve fitting remained unchanged in the simulation so that we only consider the effect of the intensity noise from the light source. The results show that that the standard deviation remains to be a constant except for some small excursions as the density of the calibration spectral frames increases. The observation can be explained by a simple noise analysis of the correlation coefficients as follows.

Both the calibration and measurement spectral frames ($R_i$ and $M$) contain the intensity noise from the light source. The light intensity measured by the $j^{th}$ pixel in the calibration and measurement spectral frames can be written, respectively, as $R_{ij} = R_{ij0} + r_{ij}$ and $M_j = M_{j0} + m_j$, where $R_{ij0}$ and $M_{j0}$ are the expected values of the intensities measured by the pixels, and $r_{ij}$ and $m_j$ are the corresponding fluctuations due to the intensity noise. Plugging them into Eq.(3.2) and after some straightforward algebra, we found that the correlation coefficient between $R_i$ and $M$ can be expressed as

$$\rho\left(M, R_i\right) = \frac{1}{N-1}\frac{1}{\sigma_i \sigma}\sum_{j=1}^{N}\left(R_{ij0}M_{j0} + R_{ij0}m_j + r_{ij}M_{j0} + r_{ij}m_j - \bar{R}_i\bar{M}\right), \tag{3.3}$$

In fitting the correlation coefficients to find the measurand, the effect of the noise terms involving $r_{ij}$ in Eq. (3.3) can be effectively suppressed by increasing the density of the calibration frames used for curve fitting. However, the second term of the sum on the right side of Eq. (3.3), $\sum_{j=1}^{N} R_{ij0}m_j$, is independent on $i$ and can be considered as a systematic noise uniformly imposed onto the correlation coefficients for all calibration frames. As a result, the noise contribution from this term cannot be suppressed by increasing the data point density for curve fitting, as shown in Fig. 3.10. In other words, the noise of the measurement frame set a limit to the standard deviation of the curve fitting results.

#### 3.2.2.3 Experiments

Experiments were carried out to demonstrate the modified correlation demodulation method and compare its performance with other methods. The experimental setup is schematically shown in Fig. 3.12. Two fiber-optic temperature sensors with two different optical cavity lengths were fabricated for the demonstration. Each of them consists of a double-side polished silicon pillar attached to the end face of a single mode fiber. The thicknesses of the silicon pillars in the two sensors are 40 and 200 $\mu$m, corresponding to optical cavity lengths of 136 and 680 $\mu$m at 1550 nm, respectively. Both silicon pillars have a same diameter of 100 $\mu$m. The detailed fabrication process of the sensor can be found in Ref. [25]. The light output from a SLED passes through a fiber-optic circulator before reaching the sensor head, and the light reflected from the sensor head was directed to a high-speed spectrometer (Model: I-MON 512 USB, Ibsen Photonics) for spectral measurement by the circulator. The spectrometer has a maximum frame rate of 3 kHz with 512 pixels in each frame approximately equally distributed over the wavelength range between 1510-1595 nm. The sensor head was placed in an environmental chamber with controlled temperature. We obtained the calibration spectral frames by continuously recording the reflection spectrum at a frame rate of 500 Hz as the temperature of the sensor while the sensor was cooled down in the environmental chamber from 80 °C to 10 °C. The process took slightly over 6 minutes to complete. Note that, in practice, obtaining the calibration frames requires an independent temperature sensor. For convenience, the temperature was measured from the sensor spectrum using the wavelength tracking method with the spurious jumps eliminated by a polynomial curve fitting of the results over the time range. Figure 3.13 (a) shows the obtained relative temperature variation of sensor as a function of time. We compared the noise performance of the correlation method and the regular curve fitting method by placing the sensor at a constant temperature of 22 °C, and continuously recorded the sensor spectrum for 8 s with a spectral frame rate of 3 kHz. Fig. 3.13 (b) shows the temperature results demodulated by the curve-fitting method (blue), the correlation method with a single free spectrum range (red), and correlation method with a full spectrum (black) for the sensor with 136 $\mu$m optical cavity length. The correlation method with a single free spectrum range

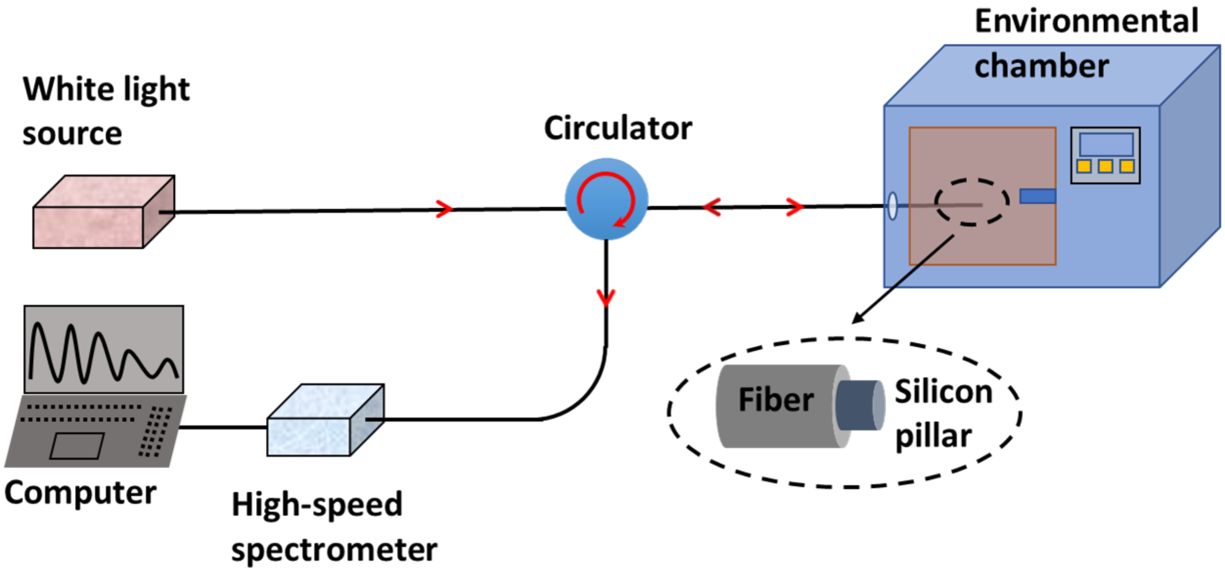

Figure 3.12: Experimental setup for demonstration using a temperature sensor system.

resulted in a standard deviation (4.90 mK) that is slightly larger than the curve-fitting method (4.37 mK). Note that the results from the curve fitting method show no spurious jumps because the pixel set used for curve fitting remain unchanged during the demodulation. The correlation method with a full spectrum shows a much higher resolution than the curve fitting method (1.82 mK vs. 4.37 mK). We then compared the performance of both methods for measurement of dynamic temperature. In this experiment, we reduced the sensor temperature from 40 °C to 30 °C and the results from both methods over a span of 12 °C change are shown in Fig. 3.13 (c). It is seen that the results from the correlation method (red curve) show a smooth response of the sensor to the temperature variation, while the results from the curve fitting method have several large spurious jumps [details of the results around the spurious jumps are shown in the inset of Fig. 3.13 (c)]. Aside from the absence of the jumps, the results from the correlation method appears to have slightly larger fluctuation (noise) than the curve fitting method consistent with the noise performance in Fig. 3.13 (b). Finally, we studied effect the of the calibration spectral frame density on the standard deviation of the sensor, and the results are shown in Fig. 3.13 (d). The standard deviation appears to be a constant with small fluctuations, which is consistent with the simulation results shown in Fig. 3.11. For the sensor with 680 $\mu$m optical cavity length, Figure 3.14 (a) shows the noise performance of correlation and curve fitting demodulation methods when the sensor was at constant temperature (static test). The correlation method with a single free spectrum range leads to a standard deviation of 1.39 mK (red curve), which is slightly smaller than the curve fitting method (2.40 mK, blue curve). A resolution as high as 0.27 mK was obtained by using a correlation demodulation with a full spectrum. Figure 3.14 (b) shows the experimental results demodulated by these two methods in a dynamic test where the temperature of the sensor was varied by 10 °C. The correlation method shows a smooth temperature response curve with smaller temperature fluctuations, while the curve fitting method shows multiple spurious jumps. An enlarged view of a single jump is showed in the inset of Fig. 3.14 (b).

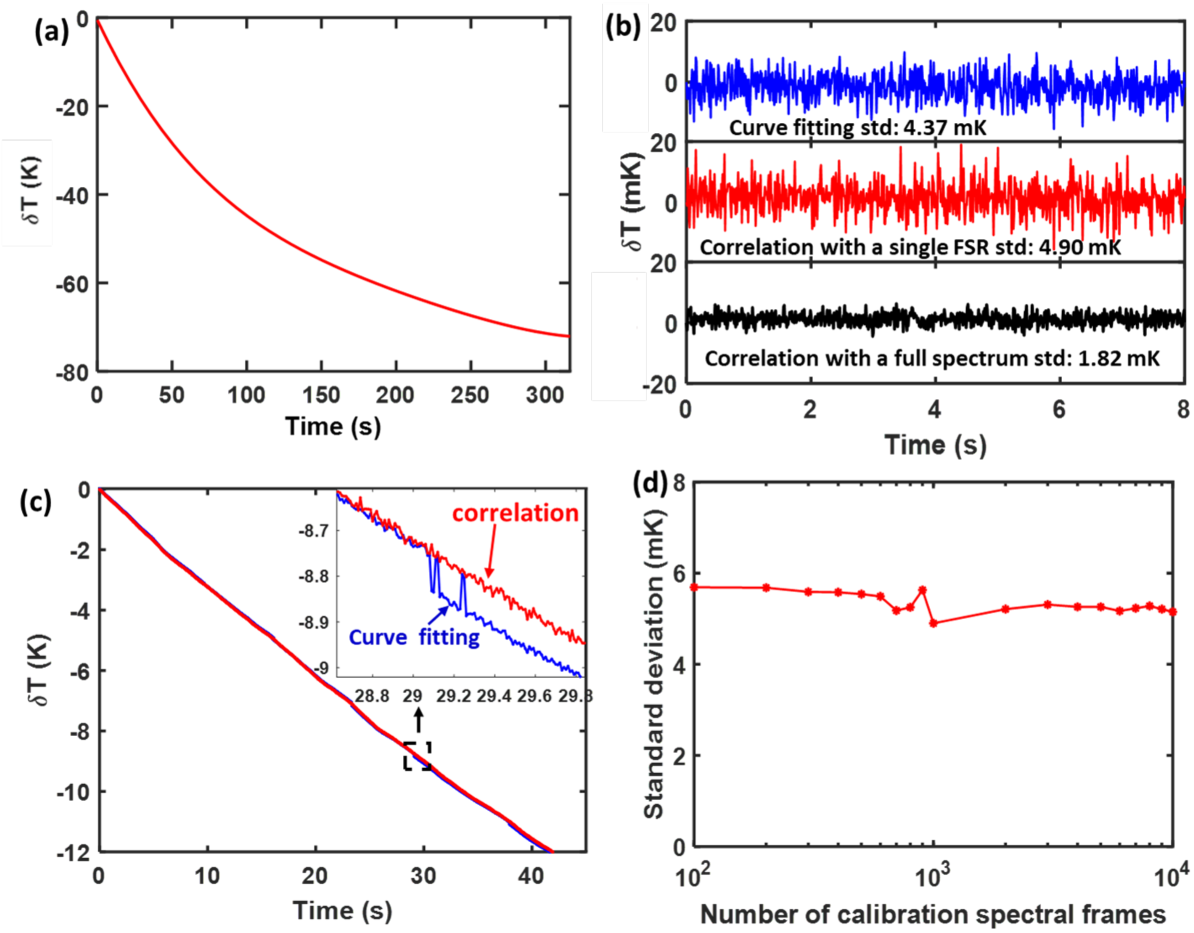

Figure 3.13: (a) Relative temperature variation versus time. (b) and (c) show, respectively, the temperature variation as function of time. The insets of (c) is a close view of the spurious jumps in the results from the regular curve fitting method. (d) Standard deviation (std) vs. number of calibration spectral frames.

#### 3.2.2.4 Centroid demodulation

Centroid demodulation is another simple method used for wavelength tracking of fiber-optic interferometric sensors. Because the implementation of the centroid method does not rely on any specific mathematic model for the spectral fringes, it is worth studying its performances regarding spurious jumps. This method calculates the centroid of the spectral feature, $\lambda_c$ , using [40]

$$\lambda_c = \sum_i S_i\lambda_i / \sum_i S_i, \tag{3.4}$$

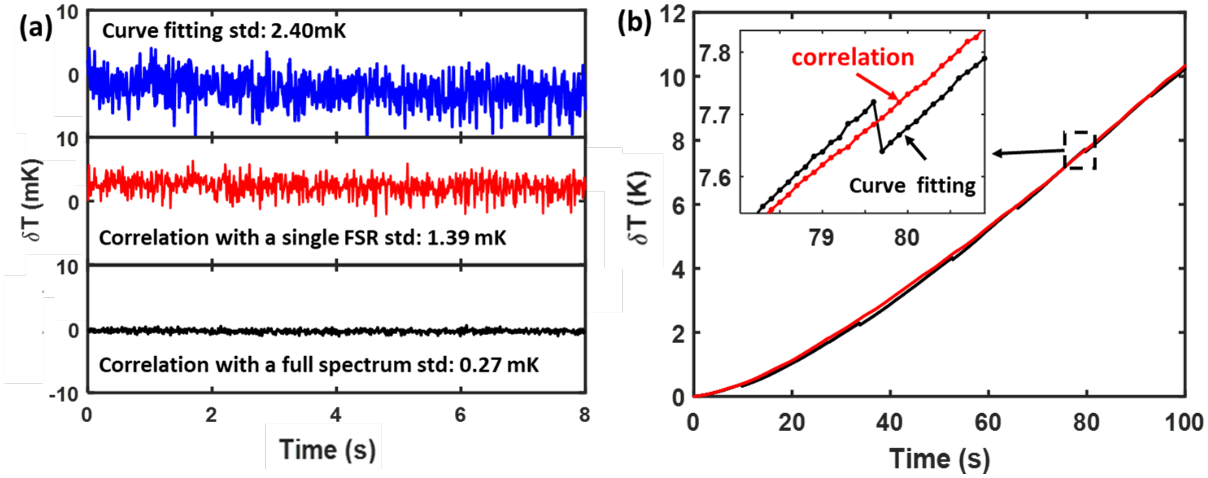

Figure 3.14: (a) and (b) show, respectively, the temperature variation as function of time. The insets of (b) is a close view of the spurious jumps in the results from the regular wavelength-tracking method.

where $S$ and $\lambda_i$ are, respectively, the intensity and wavelength of the $i^{th}$ pixel. We carried out the method on the data obtained from both the static and dynamic tests of the temperature sensor with an optical cavity length of 136 $\mu$m. The pixel sets being used to calculate the centroid of fringe valleys are identical to those used for the curve fitting method with interpolation [see Fig. 3.13 (c)]. Figure 3.15 (a) is the measured temperature variations from a static test where the temperature was kept constant. Compared with the correlation method [Fig. 3.13 (b)], the centroid method exhibits similar noise performance (4.90 vs. 4.50 mK). Figure 3.15 (b) is the temperature response from a dynamic test where the temperature decreased demodulated by the centroid method (black curve). For comparison, the results from the correlation method are also shown (red curve). It is seen that the centroid method shows multiple large jumps. For example, a jump of 1.4 K occurs between data points $T_1$ (pink dot) and $T_2$ (red dot). The pixel sets used to calculate the centroids corresponding to these two data points are shown in Fig. 3.15 (c), indicating that the jumps arise from the changes in the pixel set for centroid computation. In addition to the jumps, we noticed that, in the time between jumps, the temperature reading from the centroid method shows unexpected temperature rises inconsistent with the actual temperature change that decreased monotonically during the testing. For example, a temperature rise of 0.8 K was obtained from $T_2$ (red dot) to

$T_3$ (blue dot) [see Fig. 3.15 (b)]. The pixel sets used to calculate the centroid corresponding to these two data points $T_2$ and $T_3$ are shown in Fig. 3.15 (d). Although the pixel sets for obtaining these two data points were unchanged and an apparent shift to the lower wavelength was observed, the distribution variations of pixels on the fringes leads to the shifts of centroid of these pixel sets toward longer wavelength, resulting in the incorrect changes of measured temperature from the centroid method. These results highlight the excellent performance of the modified correlation method in eliminating the spurious jumps and achieving high measurement accuracy of fiber-optic interferometric sensors.

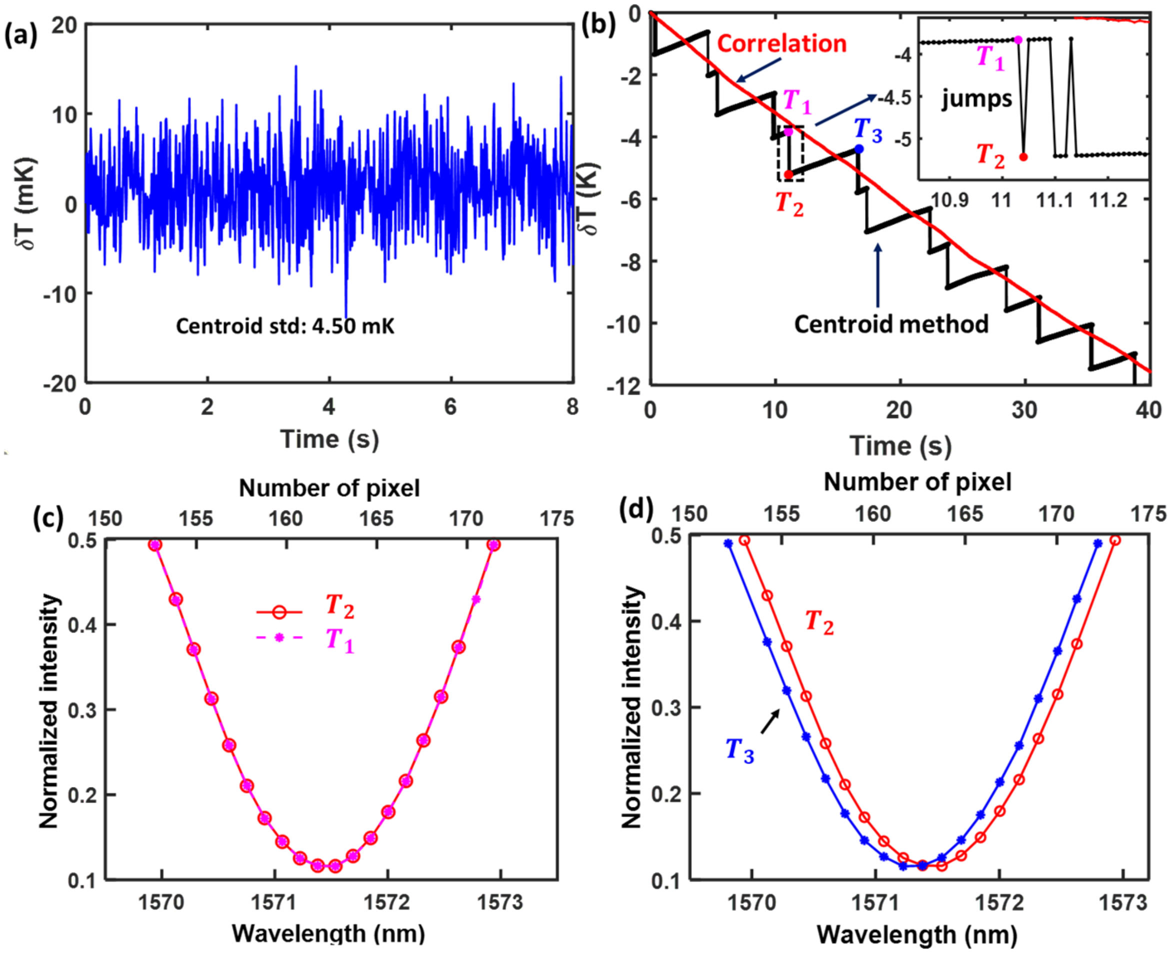

Figure 3.15: Variations of temperature reading with time from centroid method under (a) static test and (b) dynamic test. The reading from the modified correlation method is also shown in (b). The inset of (b) shows an enlarged view of jumps.

### 3.2.3 Conclusion

Wavelength-tracking method based on curve fitting is commonly used for the demodulation of fiber-optic sensors interrogated by a white-light system. However, the signal demodulated by the method can exhibit spurious jumps. Employing Monte Carlo simulation, we found that these jumps originate from the inaccuracy of the mathematical model for fitting the measured sensor spectrum and manifested by the changes in the pixel set for curve fitting. Although our simulation shows that increasing the density of pixels for curve fitting can effectively reduce the spurious jumps, in practice, this strategy is limited by the finite pixel numbers of available spectrometers. The spurious jumps are not unique to curve fitting method. We found that centroid method is also susceptible to the jumps from the pixel set changes used for calculating the centroid. We proposed and demonstrated a modified correlation method that can effectively remove the spurious jumps without the need to increasing the pixel density of the spectrometer. In this method, the measurand is found by curve fitting of the correlation coefficients between the measurement spectral frame and a set of calibration spectral frames of the sensor. The calibration frame can be made sufficiently dense in practice, so that there is no spurious jump from curve fitting. The method was demonstrated both numerically through Monte Carlo simulations and experimentally using a fiber-tipped silicon temperature sensor. The results from the numerical simulation and experiment are consistent, both indicating that the correlation method can efficiently eliminate spurious jumps giving rise to a higher accuracy sensor reading. In addition, much higher resolution can be obtained by using a full spectrum demodulation. The correlation method can also be used for other types of fiber-optic sensors.

# CHAPTER 4

# DEVELOPMENT OF FIBER-OPTIC BOLOMETER BASED ON A HIGH-FINESSE SILICON FP INTERFEROMETER

*Contents of this chapter have been published in*

- *Reproduced from [Q. Sheng, G. Liu, N. Uddin, M. L. Reinke, and M. Han, "A fiber-optic bolometer based on a high-finesse silicon Fabry-Perot interferometer," Review of Scientific Instrument, vol. 89, 065002, 2018],with the permission of AIP Publishing.*
- *Q. Sheng, G. Liu, N. Uddin, M. L. Reinke, and M. Han, "Fiber-optic silicon Fabry-Perot Interferometric bolometer: the influence of mechanical vibration and magnetic field," Jounral of Lightwave Technology, vol. 38, pp. 2547-2554, 2020.*

In this chapter, we pay attention to the development of high-finesse fiber-optic bolometer. We first report a fiber-optic bolometer that can achieve a much lower noise equivalent power density by reducing the FP interferometer length and increasing the finesse of the silicon FP interferometer using high-reflectivity coatings. Reducing the FP interferometer length will lead to a higher temperature responsivity owing to the reduced thermal mass. In the meantime, a high-finesse FP interferometer features much narrower spectral features in its reflection spectrum resulting in a lower noise in temperature sensing. We show that the increased responsivity and reduced noise lead to a noise equivalent power density of 0.27 W/m$^2$, a 35 times reduction compared to the fiber-optic bolometer reported previously.

We then study the influences of mechanical vibration and magnetic field on the performance of fiber-optic bolometers and the mitigation of the influences. Specifically, based on an fiber-optic bolometer that we demonstrated above, we characterized the noise performance of the fiber-optic bolometer when the fiber with the bolometer was vibrated by an electromagnetic shaker. The experimental results showed that the vibration significantly increases the noise of the fiber-optic bolometer system. We also characterized the effect on the performance of the fiber-optic bolometer from quasi-dc magnetic field generated from a solenoid applied on the fiber. We found that the change of the magnetic field along the axial direction of the fiber also led to signal variations of the fiber-optic bolometer. The sensitivity of the fiber-optic bolometer to mechanical vibration and magnetic field can both be attributed to the birefringence of the silicon sensor head. We show that two methods can be effective in mitigating the effect caused by the sensor birefringence: (1) replacing the regular SMF in the fiber-optic bolometer with polarization-maintaining fiber and (2) using a polarization scrambler after the laser source. For both methods, no significant increase in the noise was observed in the vibration and magnetic field tests. Our research highlights the importance of the polarization management for the fiber-optic bolometer systems toward their practical applications in MCF systems.

## 4.1 A fiber-optic bolometer based on a high-finesse silicon FP interferometer

### 4.1.1 Bolometer design and fabrication

Schematic of the fiber-optic bolometer is shown in Fig 4.1 (a). The top surface of the silicon pillar is coated with a thin layer of gold which functions as both a high-reflectivity mirror and an effective broad-bandwidth absorption layer for the incident radiation flux. The bottom surface of the silicon pillar is coated with HR dielectric multi-layers for the probing light at around 1550 nm. These high reflection mirrors make the silicon pillar act potentially as a high-finesse FP interferometer. To reduce the diffraction round-trip loss of the light beam from the single-mode fiber, a section of graded-index multimode optical fiber, which acts as a collimator [29, 41], is sandwiched between the FP interferometer and the single-mode fiber. The length of the graded-index multimode fiber is chosen to be a quarter of the period of the ray trajectory within the multimode fiber [29, 41],.

The theoretical reflection spectrum of a 75 $\mu$m thick silicon FP interferometer with different mirror reflectivity is shown in Fig. 4.1 (b), which is calculated from [42]

$$F(\lambda) = \frac{R_1 + R_2 - 2\sqrt{R_1 R_2}\cos\left(2\pi \frac{2n_{si}d}{\lambda}\right)}{1 + R_1 R_2 - 2\sqrt{R_1 R_2}\cos\left(2\pi \frac{2n_{si}d}{\lambda}\right)}, \tag{4.1}$$

where $R_1$ and $R_2$ are, respectively, the reflectivity of the front and back mirrors of the FP interferometer; $\lambda$ is wavelength; $d$ is the thickness of the FP interferometer; and $n_{si}$ is the refractive index of silicon (around 3.4 at 1550 nm). It shows that the full width at half maximum is reduced from around 1.5 nm of the initial low-finesse silicon FP interferometer without high reflection coatings (blue curve) to only 30 pm of the high-finesse FP interferometer with two 98% high reflection mirrors (black curve). With the small full width at half maximum of the high-finesse FP interferometer, the FP interferometer can be demodulated by a narrow linewidth DFB laser whose wavelength is scanned through injection current modulation.

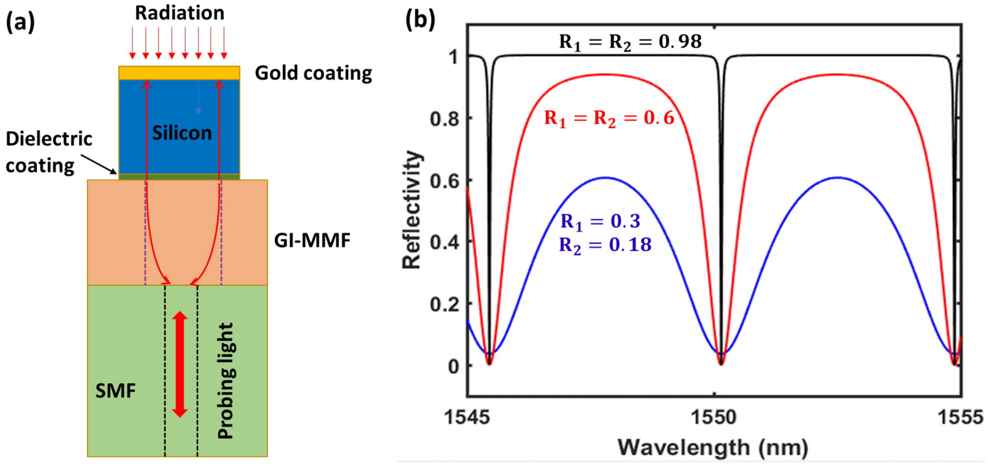

Figure 4.1: (a)Schematic of the fiber-optic bolometer. (b) Simulated reflection spectrum of a 75 $\mu m$ thick silicon FP interferometer with different mirror reflectivities.

To fabricate the bolometer, the silicon pillar was prepared first. A 75 $\mu m$-thick silicon wafer was coated with high reflection dielectric coating on one side and with 150 nm-thick gold coating on the other side. Note that the gold coating is unlikely to induce electromagnetic interference to the sensor system because of the optical operation of the system. The coated silicon wafer was then broken into small fragments. A graded-index multimode fiber (Corning, InfiniCor 300) was spliced to the end face of a single-mode fiber and was cut to an appropriate length so that it functions as a collimator, as shown in Fig. 4.2 (a). More specifically, the period of the ray trajectory was estimated based on the index profile of the graded-index multimode fiber using the methods detailed in Refs. [29, 41]; then the length of the multimode fiber was cut to a quarter of the period using a fiber cleaver under a microscope so it functioned as a collimator (see Fig. 4.2 (a)). The length of the multimode fiber was 250 $\mu m$ in this case. Next, facilitated by an optical microscope, the lead-in fiber with a thin layer of glue attached to its end face was pressed against the side of the fragmented silicon with the dielectric coating, as shown in Fig. 4.2 (b). The reflection spectrum of the FP interferometer was monitored by an optical spectrum analyzer as the position of the fiber was adjusted carefully to achieve a satisfactory visibility before the glue was cured in air and the FP interferometer was attached to the fiber end face, as shown in Fig. 4.2 (c). Finally, since the fragmented silicon had an irregular shape and large size leading to a long response time. After this polishing process, a silicon pillar with smaller size and more regular shape was obtained as shown in Fig. 4.2 (c), a polishing machine was used to polish the edges of the silicon pillar, giving the final shape and size of each individual bolometer. Figure 4.2 (d) and 4.2 (e) are, respectively, the side-view and top-view images of a fabricated bolometer. Note that the diameter of the silicon pillar was 300 $\mu m$, which is larger than that of the lead-in fiber (125 $\mu m$). A larger diameter of the FP interferometer increases the sensitivity by reducing the heat loss through conduction to the fiber but with the sacrifice of an increase in the response time [25, 43].

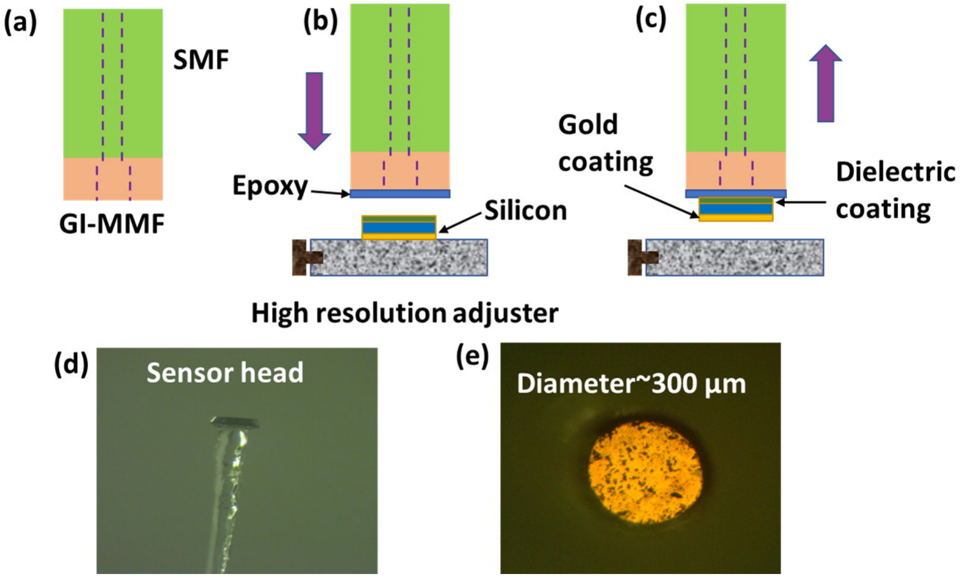

Figure 4.2: [(a)-(c)] Schematics of the fabrication steps for the fiber-optic bolometers. (d) Side-view and (e) top-view images of a fabricated fiber-optic bolometer sensor head. The diameter of the sensor head is around 300 $\mu$m and the thickness of the silicon pillar and the gold coating is 75 $\mu$m and 150 nm, respectively.

The reflection spectrum of a fabricated bolometer measured by the optical spectrum analyzer is shown in Fig. 4.3 (a), which indicates a fringe visibility of >7 dB and a free spectrum range of 5 nm. Figure 4.3 (b) shows an enlarged view of one reflection notch with a full width at half maximum of around 140 pm, indicating that the finesse of the FP cavity was > 35. It is seen from Fig. 4.3 (a) and 4.3 (b) that there are "bumps" on both shoulders of the reflection notches. The origins of this unexpected spectral feature are unknown and under investigation.

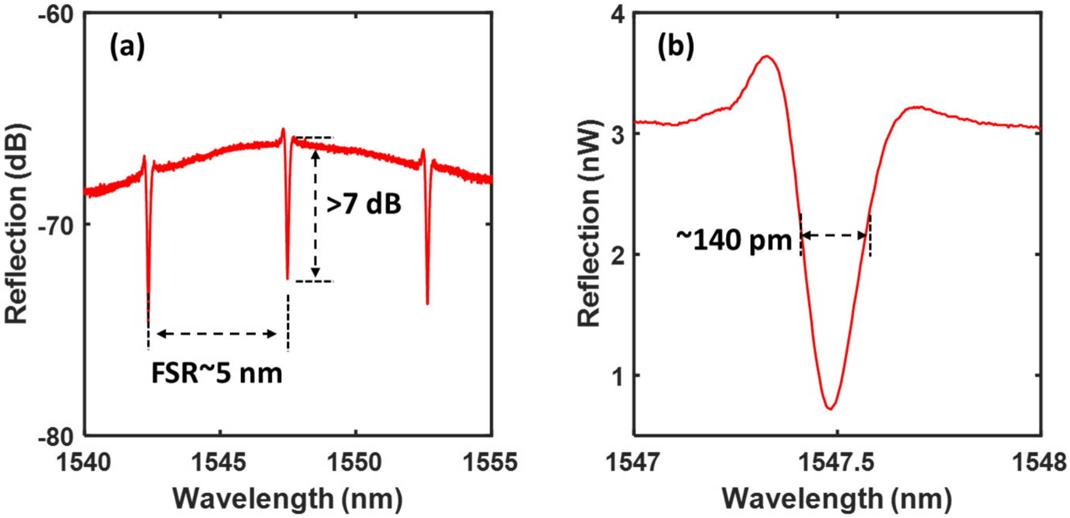

Figure 4.3: (a) Reflection spectrum of a fabricated fiber-optic bolometer. (b) Englarged view of a reflection notch.

### 4.1.2 Experiment and results

We demonstrated the proposed bolometer and characterized its performance using an experimental setup schematically shown in Fig. 4.4 As aforementioned, the considerably narrow notch width of the bolometer allows us to use a narrow-linewidth distributed feedback diode laser (Model: CQF975, JDSU) for demodulation. The center wavelength of the distributed feedback laser can be slowly tuned over a large range of > 2 nm through its temperature controller; while high-speed wavelength scanning can be achieved through injection current modulation over a smaller wavelength range of 300 pm. In the experiment, the laser wavelength was first tuned close to one of the spectral notches ( around 1547.5 nm) by controlling the laser temperature and then the laser wavelength was scanned by modulating the injection current with a triangle wave with a frequency of 2 kHz and a peak-to-peak current of 200 mA (corresponding to wavelength scanning range of 280 pm) . To remove the common noise resulting from environmental temperature variations and laser wavelength drift, a dummy fiber-optic bolometer, which was blocked from the radiation, was incorporated in the system. The light from the distributed feedback laser was split into two paths with a 33/67 coupler. The path with the low power went into the dummy bolometer via a circulator, while the other part was delivered to the sensing bolometer via an attenuator and a circulator. The returned signal was received by a photodetector and then recorded by a data acquisition module with a sampling rate of 2 M/s. A 405 nm diode laser, whose intensity was modulated by a square wave with a frequency of 0.1 Hz, was used to simulate the radiation from the plasma. A photodetector with a known active area (Model: PDA36A-EC, Thorlabs) was used to measure the radiation power density where the bolometer sensor head was located. Two irises were applied to prevent the simulated radiation from reaching the dummy bolometer. Spacing between the dummy and sensing bolometers was around 5 mm.

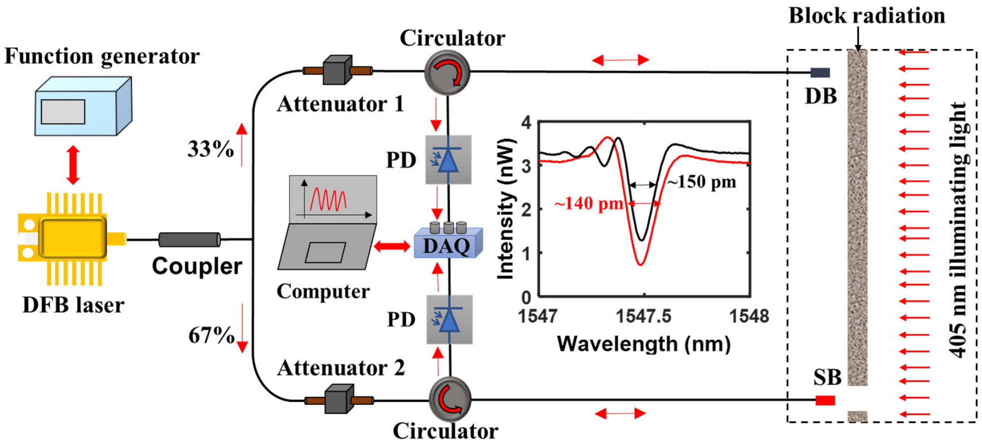

Figure 4.4: Experimental setup. The inset (red desh line) shows spectra of the sensing bolometer and the dummy bolometer at room temperature.

Due to the small wavelength tuning range (< 300 pm) of the distributed feedback laser through current injection, the spectral notches from these two bolometers need to be close to each other. An attenuator was included in path for the sensing bolometer to fine tune the wavelength of the sensing bolometer. A small fraction (∽ 2%) of the laser delivered to the bolometer was absorbed by the gold coating on the bolometer. This residual absorption provides a convenient way to fine-tune the wavelength position of the spectral notch of the bolometer to match that of the other bolometer through the attenuator. The reflection notches for both bolometers are shown in the inset of Fig 4.4. The separation of the two spectral notches was around 20 pm at room temperature.

Using the experimental setup and method described above, we first characterized the noise level of the bolometers. The noise level was obtained by calculating the standard deviation of the relative temperature variations which were retrieved from the wavelength variations in the absence of radiation and then converted using a temperature sensitivity of 84.5 pm/°C [25]. The standard deviation was calculated using data obtain during a period of 50 s, which was chosen to be much larger than the repetition period of 10 s of the radiation laser (405 nm). Figure 4.5 (a) shows one frame of the original data that were used to track the relative wavelength variation. The wavelength tuning range was about 280 pm for both the rising ramp (0-0.25 ms) and falling ramp (0.25-0.5 ms), measured by a Mach-Zehnder interferometer with known free spectrum range. The relative wavelengths for the sensing bolometer and the dummy bolometer were calculated by fitting the notch positions using a third-order polynomial function. After converting the fitted notch wavelength into temperature variation, the results are shown in Fig. 4.5 (b). The perfect overlap of the curves for both the sensing bolometer (red) and dummy bolometer (black) testifies that the two bolometers had common noise sources. We found that the dominant noise source in this case was the laser wavelength drift. A moving average over 400 consecutive data points were performed to the data of the dummy bolometer, which removes the high-frequency noise unrelated to the laser drift. The result is shown as the smoother green curve in Fig. 4.5 (b). By subtracting the time-averaged reading of dummy bolometer from the reading of the sensor bolometer, the common noise was substantially removed. The noise level of sensing bolometer with common noise subtracted is shown as the blue curve in Fig. 4.5 (b). The relative temperature shows a standard deviation of $1.2 \times 10^{-4}$ °C, which was 5 times lower than that of the fiber-optic bolometer demonstrated previously using a spectrometer [25, 26]. To characterize the resolution of the bolometer, we

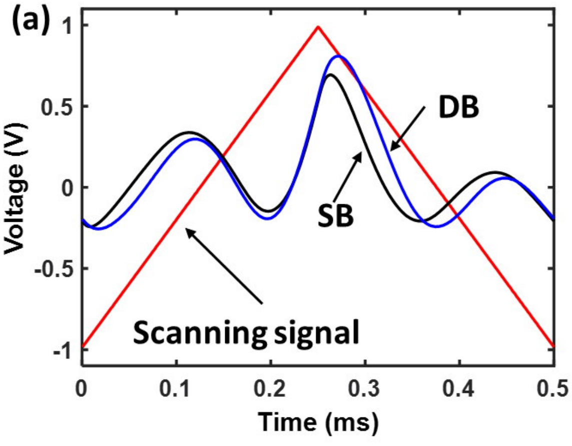

Figure 4.5: (a) A typical frame of the original data obtained by the data acquisition system. (b) Relative temperature variation in the absense of radiation laser. SB: sensing bolometer; DB: dummy bolometer.

measured the response to radiation power density as low as 0.8 W/m$^2$ and the results are shown in Fig.4.6. Before the removal of the common noise, the signal from the sensing bolometer (red curve) is buried in the large common noise. The blue curve is the signal after the common noise is removed using the time-averaged response from the dummy bolometer. The much cleaner signal proves the effectiveness of using a dummy bolometer to remove the common noise. Then we characterized

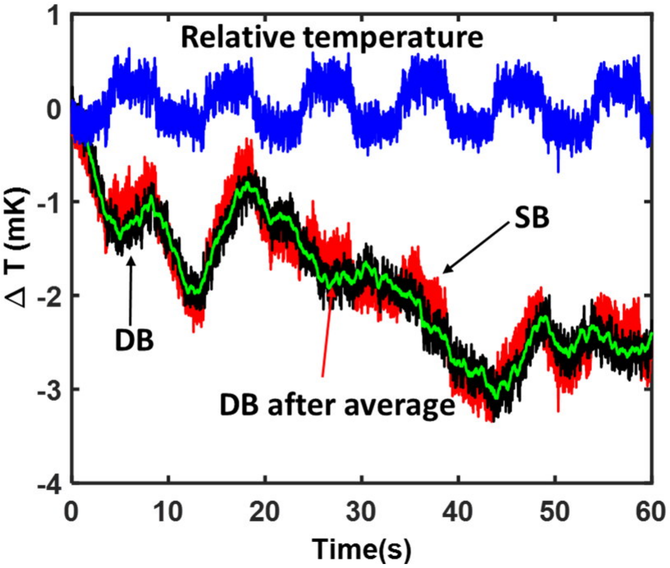

Figure 4.6: Relative temperature variation with a relative low radiation. SB: sensing bolometer; DB: dummy bolometer

the responsivity and response time of the bolometer. Figure 4.7 (a) shows the response of the bolometer to radiations with much higher power density. Compared with the fiber-optic bolometer reported previously [26], which had a temperature rise of 4 mK in response to an illuminating power density of 40 W/m$^2$, the bolometer reported here showed a temperature rise of 28 mK in response to an illuminating power density of 38 W/m$^2$, indicating a 7-time increase in responsivity. As aforementioned, this responsivity enhancement is attributed to the reduced length of the silicon FP interferometer that reduces the thermal mass and the increased diameter that decreases the heat loss rate to the lead-in fiber and the environment. Response time of the bolometer, defined as the time needed to reach 63 of the overall signal change, is found to be 400 ms from Fig. 4.7 (b) that shows the response in one cycle in more detail. The response time of the fiber-optic bolometer was more than double that of the previous one ( 150 ms). The increase in response time was mainly a result of the increased diameter of the FP interferometer of the bolometer. The response time of the bolometer is inversely proportional to the surface-to-volume ratio of the silicon pillar [25]. The increase of the diameter of the silicon pillar decreases the surface-to-volume ratio which in turn increases the response time. Note that the maximal temperature rise for each cycle exhibited a slow drift as shown by the red dashed curve in Fig.4.7 (a), which is believed to arise from the instability of the illuminating laser.

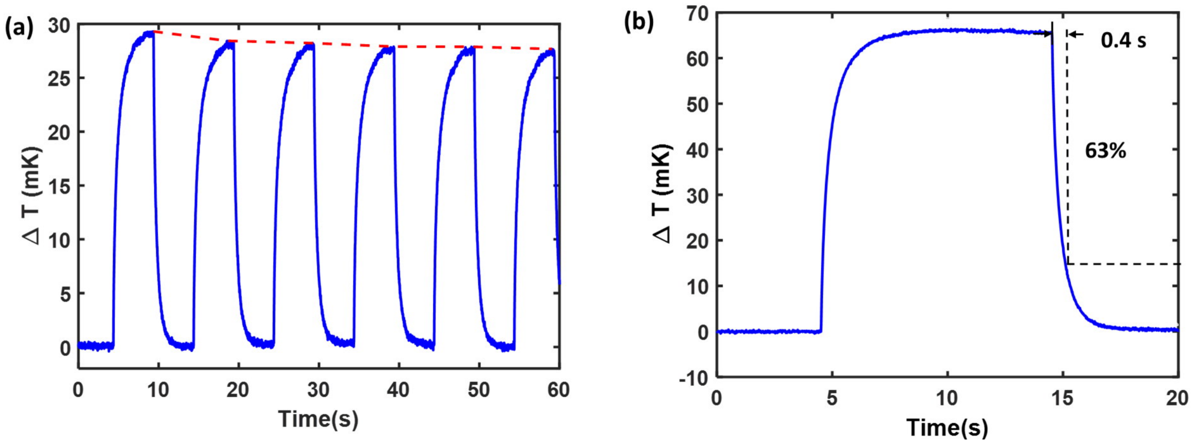

Figure 4.7: (a) Relative temperature variation with a relative high radiation power density. (b) Close-up view of a response circle.

Finally, we characterized the signal to noise ratio of the bolometer, defined by the temperature rise divided by $\sqrt{2}\sigma_T$, where $\sigma_T$ is the standard deviation of the noise (blue curve in Fig. 4.5 (b)). Signal to noise ratio was calculated at different power density levels of the radiation ranging from 0.8-100 W/m$^2$. The results are shown in Fig. 4.5. Compared with the signal to noise ratio of the previous bolometer, a 35-time improvement in signal to noise ratio has been achieved. Using a linear fitting line, the noise equivalent power density value is estimated to be less than 0.3 W/m$^2$, which is close to the noise equivalent power density of state-of-the-art resistive bolometers tested in a laboratory environment.

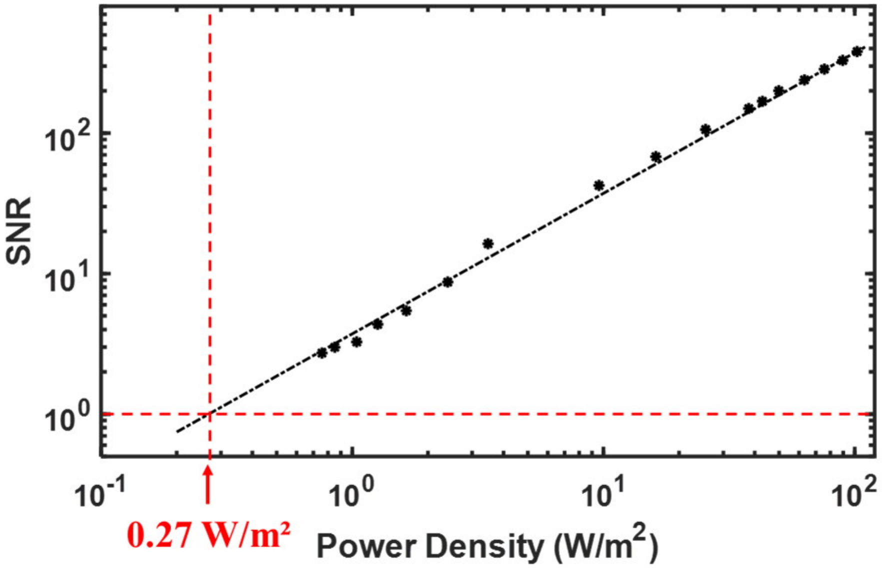

Figure 4.8: Measured signal to noise ratio versus power density. The noise equivalent power density of the bolometer corresponds to the power density level when SNR = 1. SNR: signal to noise ratio.

We note that the wavelength scanning range of the laser used here was 280 pm, equivalent to the wavelength shift caused by a temperature rise of 3.3 °C or a power density of >4000 W/m$^2$, which is sufficient for most bolometer applications in magnetic confinement fusion reactors. The bolometer was tested only under the conditions where the radiation flux is normal to the end face of the bolometer. The sensor response is expected to be dependent on the radiation direction. Therefore, the bolometer in its current configuration is intended to be used under conditions with known radiation direction, such as in a pin-hole camera for plasma imaging.

### 4.1.3 Conclusion

A fiber-optic bolometer based on a silicon FP interferometer with high-reflectivity coatings was demonstrated. The high-reflectivity coatings generate a high-finesses FP interferometer and thus reduce the wavelength demodulation noise along with a scanning laser. In the meantime, the sensitivity is increased by reducing the thermal mass via reducing the cavity length, the sensitivity is also increased by increasing the silicon diameter which reduces the heat dissipation rate to the lead-in fiber. The noise is significantly reduced through a dummy bolometer that is placed close to the sensing bolometer but blocked from the radiation being measured. Experimental results show that, compared to a previously reported fiber-optic bolometer, the bolometer reported here showed a 5-fold decrease in noise and 7-fold increase in responsivity, leading to an estimated noise equivalent power density of 0.3 W/m$^2$, comparable to the noise equivalent power density of the state-of-the-art resistive bolometers tested in a laboratory environment. Due to the immunity to electromagnetic interference, the fiber-optic bolometer is expected to outperform resistive bolometers in field applications.

## 4.2 Fiber-optic silicon FP interferometric bolometer: the influence of mechanical vibration and magnetic field

### 4.2.1 Fiber-optic bolometer preparation and birefringence characterization

#### 4.2.1.1 Fiber-optic bolometer preparation

Figure 4.9 (a) schematically shows the structure of the fiber-optic bolometer head used in the study [44]. It consisted of a lead-in single-mode fiber, a small section of graded-index multimode fiber serving as a collimator [29, 41, 45], and a 75 $\mu$m thick double-side polished silicon pillar attached to the end face of the graded-index multimode fiebr collimator. The silicon pillar was coated with a high reflection dielectric thin film on the surface glued to the graded-index multimode fiber collimator and a 150-nm thick gold layer on the front surface, which form a high-finesse planar silicon FP interferometer. The plasma radiation impinging onto the front surface increases the temperature of the silicon FP interferometer, which is deduced by the fringe shift of reflection spectrum of the silicon FP interferometer. The fiber-optic bolometers used in the experiment were fabricated following the process described in Ref. [44]. Figs. 4.9 (b) and (c) show, respectively, a picture of a fabricated fiber-optic bolometer head and its reflection spectrum measured by a white light source and an optical spectrum analyzer with a spectral resolution of 20 pm. It shows that the free spectrum range) of the FP interferometer is 5 nm and the full width at half maximum of the resonant notch is 140 pm, corresponding to a finesse of 35 for the FP interferometer. Two "bumps" are found on the shoulders of the resonant notches with the one on the shorter-wavelength side is more prominent, as shown more clearly in Fig. 4.9 (d). These bumps are believed to arise from the imperfect parallelism of the two surfaces of the FP interferometer as well as the non-normal incidence of the light to the FP interferometer [46]. They typically have little negative effect on the operation of the bolometer.

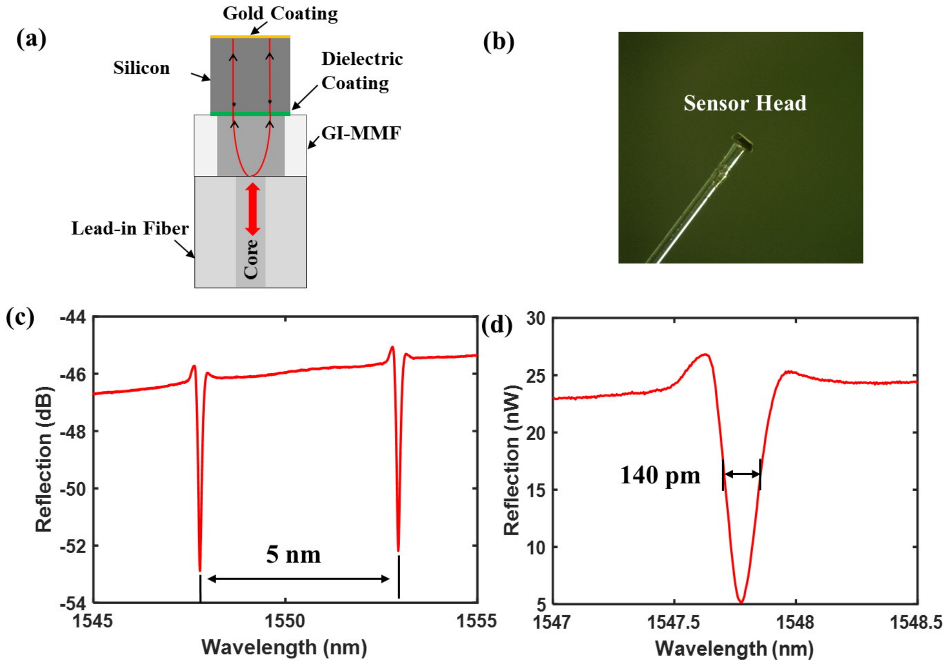

Figure 4.9: (a) Schematic of the fiber-optic bolometer head. (b) Side view of an fiber-optic bolometer head. (c) Reflection spectrum of the fiber-optic bolometer measured by an optical spectrum analyzer. (d) Enlarged view of a spectral notch.

#### 4.2.1.2 Fiber-optic bolometer birefringence characterization

The birefringence of the silicon element in our fiber-optic bolometer structure has been observed and studied. Although crystalline silicon has a cubic structure that should be optically isotropic, birefringence may be present in the silicon wafers used for fiber-optic bolometer fabrication due to the thermal and elastic strains induced during the manufacturing of silicon wafers [47]. In our case, the processes involved in fabricating silicon pillars from the silicon wafers and depositing the multilayer dielectric film on the silicon pillar can also introduce strain to the silicon pillar, giving rise to additional birefringence to the fiber-optic bolometer head. The birefringence of the fiber-optic bolometer head was characterized by looking at the responses, in terms of resonant wavelength shift $d\lambda$ and equivalent temperature change $dT$ , of the fiber-optic bolometer as the polarization of the source laser was changed, using an experiment setup schematically shown in Fig. 4.10. A distributed feedback diode laser with a regular single-mode fiber pigtail that emits linearly polarized light around 1550 nm was used as the light source. The central wavelength of the distributed feedback laser was tuned to be close to one of the resonances of the fiber-optic bolometer by controlling the temperature of the distributed feedback laser. Then, an external

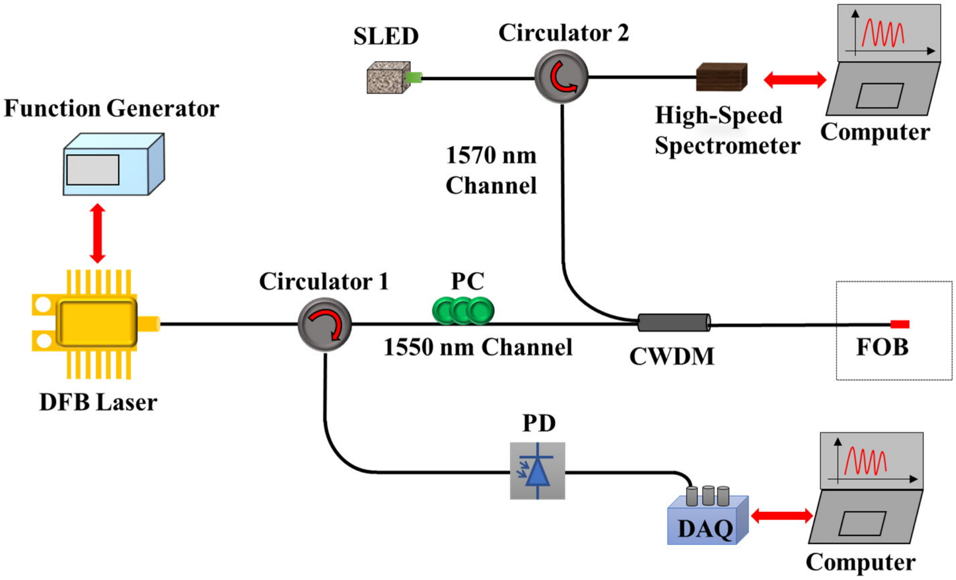

Figure 4.10: Experimental setup to characterize the sensitivity of fiber-optic bolometer to the light polarization variation.

triangle current waveform was used to scan wavelength of the distributed feedback laser with a frequency of 2 kHz over a wavelength range of 240 pm. Through a circulator (Circulator 1), the light from the distributed feedback laser was directed to the fiber-optic bolometer head (with 1.5 mW laser power reaching the fiber-optic bolometer head) and the light reflected back by the fiber-optic bolometer was received by a photodetector. The signal from the photodetector was recorded using a data acquisition system with a sampling rate of 2 MHz. A mechanical polarization controller was placed after the Circulator 1 to manually adjust the polarization state of the light from the distributed feedback laser injected into the fiber-optic bolometer.

The fiber-optic bolometer will respond to ambient temperature variations. In addition, the manual tuning of the polarization controller may introduce variations of the laser power injected to the fiber-optic bolometer and the gold mirror on the sensor head has a 2% absorption to the laser light, giving rise to potential temperature variations of the fiber-optic bolometers when the polarization controller was tuned to alter the polarization. The responses of fiber-optic bolometer to the ambient temperature change and the intensity variation are irrelevant to laser polarization and need to be separated from the overall response of the fiber-optic bolometer. To measure the temperature variation arising from ambient temperature variations and the laser intensity variations, a white-light system, including a superluminescent diode source, another circulator (Circulator 2), and a high-speed spectrometer, was included in the system through a coarse wavelength division multiplexers. The distributed feedback laser used the 1550 nm channel of coarse wavelength division multiplexers, while the white light system measured the reflection spectrum of the fiber-optic bolometer over the 20 nm wavelength range of the 1570 nm channel of the coarse wavelength division multiplexers. The transmission spectra of both distributed feedback laser and the white light source after the coarse wavelength division multiplexer are shown in Fig. 4.11. The power of the superluminescent emission diode that reach the fiber-optic bolometer was on the order of 1 mW. Figure 4.12 shows the reflection spectrum of the bolometer obtained by using the high-speed spectrometer. Apparently, the two interrogation systems were separated and independent. Note that the coarse wavelength division multiplexer was placed after the polarization controller so that

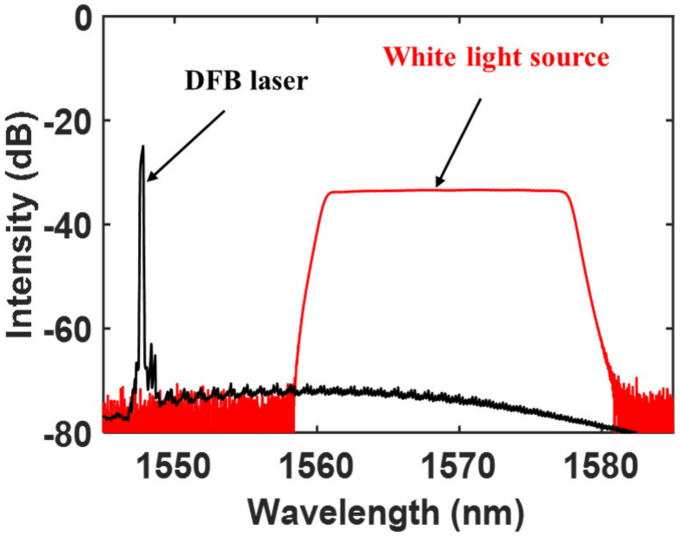

Figure 4.11: Spectra of the distributed feedback laser and the superluminescent emission diode white-light source after passing through the coase wavelength division multiplexer obtained by the optical spectrum analyzer.

the tuning of the polarization controller would not affect either the polarization state or the power of the white-light source. As a result, any wavelength shift recorded by the white-light system is expected to be from the ambient temperature variations and/or the distributed feedback laser power fluctuations. The wavelength shifts of the silicon FP interferometer measured by both systems were converted to equivalent temperature changes using the coefficient of $d\lambda/dT$ = 84.6 pm/K reported in our previous work [25]. As the polarization state was randomly changed by tuning the polarization controller, the wavelength shift and equivalent relative temperature variations were interrogated from both the distributed feedback laser and the white-light system and the results are shown in the upper figure of Fig. 4.13. It can be seen that response of white-light system gives a relatively small response that is synchronized with the change of the polarization, showing that the tuning the polarization controller indeed changed the intensity of the laser injected to the fiber-optic bolometer, which in turn varied its temperature. The laser intensity fluctuations were also obtained from the output of the photodetector, as shown in the lower figure in Fig. 4.13. It is seen that tuning the polarization controller caused a maximum of 10% round-trip change of the laser intensity. The good correlation between the temperature interrogated from the white-light system and the

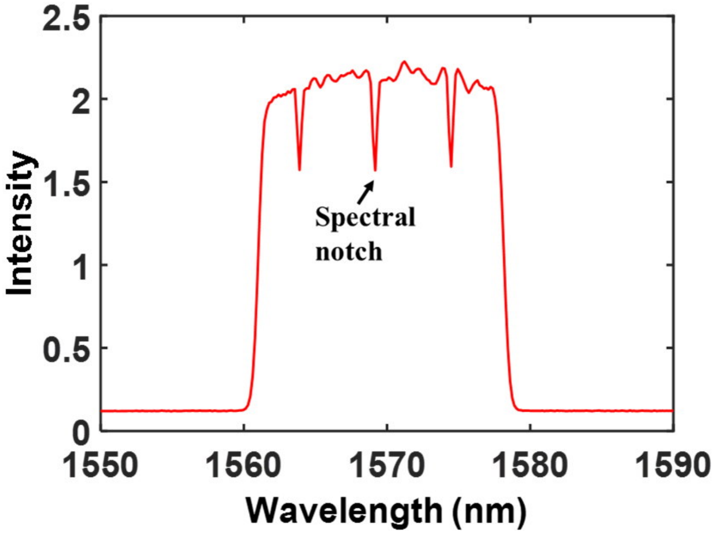

Figure 4.12: Reflection spectrum of bolometer obtained by the high-speed spectrometer.

laser intensity fluctuation further verifies that the tuning the polarization controller led to changes in laser intensity and consequent changes in fiber-optic bolometer temperature. The wavelength shift demodulated from the distributed feedback laser is much larger than the white-light system, indicating that the silicon fiber-optic bolometer has a large sensitivity to the variation of the light polarization due to the birefringence of silicon FP interferometer. To quantify the birefringence of the fiber-optic bolometer, the polarization controller was tuned with an attempt to cover all possible polarization states.

Figure 4.14 shows the two extreme cases where the resonant notch being monitored was at its shortest and longest positions with a wavelength separation of $\Delta\lambda = 13$ pm. Ignoring the temperature variations resulting from the intensity changes of the distributed feedback laser light, these cases was obtained when the laser light was linearly polarized and the polarization was aligned with each of the two principle axes of birefringence. The wavelength separation of 13 pm, corresponds to a birefringence of $\Delta n = n_x - n_y = \mathrm{n}\Delta\lambda \ / \ \lambda = 3.0 \times 10^{-5}$, where $n_x$ and $n_y$ are the refractive indices along the two principle axes of the fiber-optic bolometer, $n = 3.48$ is the refractive index of silicon, and $\lambda$ is optical wavelength of operation. This wavelength separation is equivalent to a temperature change of 150 mK. Note that the experimental setup shown in Fig. 4.10 is intended only for the study of the birefringence of the fiber-optic bolometer and the setup

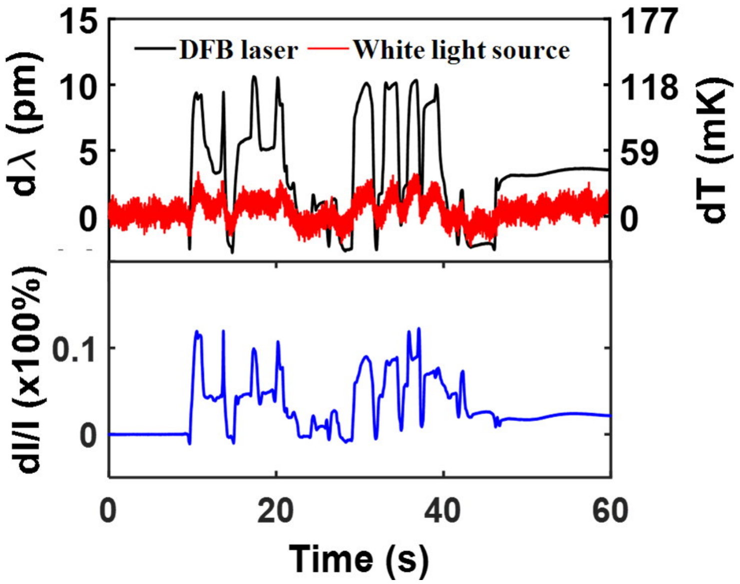

Figure 4.13: Upper: fiber-optic bolometer signals interrogated by wavelength-scanning distributed feedback laser (black) and white-light system (red) when the polarization was changed by tuning the polarization controller; lower: distributed feedback laser intensity fluctuations (*dI/I*) derived from the output of the photodetector.

for measurement of plasma radiation is different and is shown in Fig. 4.16 below.

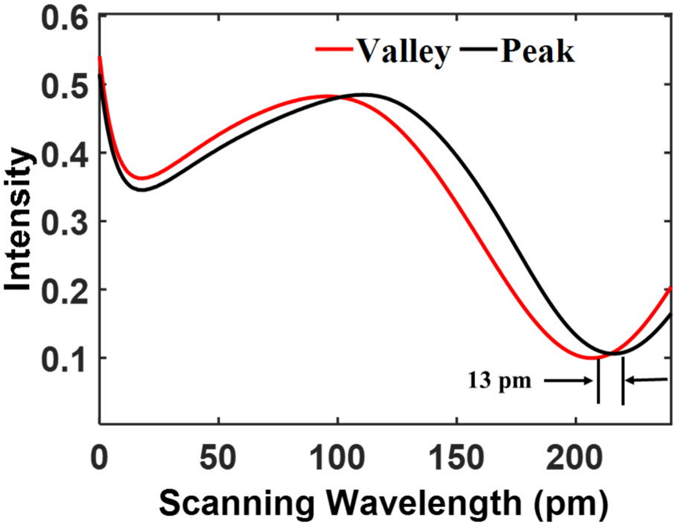

Figure 4.14: Normalized spectrum of the notch when it was at its shortest (red) and longest (black) wavelength positions.

#### 4.2.1.3 Fiber-optic bolometer sensitivity to small polarization variations

In many cases, laser polarization changes over a small range and the response of the fiber-optic bolometer to polarization fluctuations is complicated. It is dependent on the exact polarization state of the light arriving at the fiber-optic bolometer as well as how the polarization state is changed. In this section, we will consider a simple case where the light arriving at the fiber-optic bolometer is linearly polarized at an angle of $\theta$ with respect to the slow axis of the fiber-optic bolometer, as shown in Fig. 4.15 (a), and the perturbation to the polarization state is to cause a small rotation of the polarization direction. The measured reflection spectrum of the fiber-optic bolometer is the superposition of the reflection spectra measured by the light at the two principle axes of the fiber-optic bolometer, as shown in Fig. 4.15 (b). The spectra around the vicinity of the notch positions can be approximated by two quadratic functions, and, assuming the separation of the spectral notches caused by the fiber-optic bolometer birefringence, $\Delta\lambda$, is much smaller than the width of the spectral notch, the overall reflection spectrum can be written as

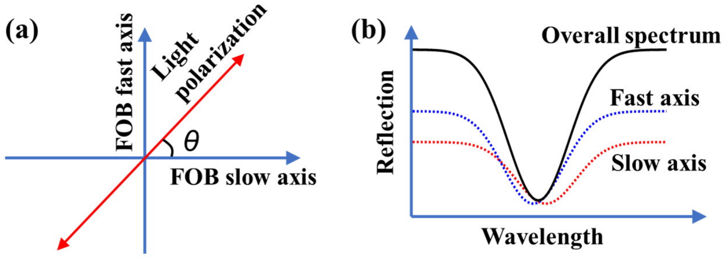

Figure 4.15: (a) Light polarization with respect to the principle axes of the fiber-optic bolometer; (b) Illustration of the measured fiber-optic bolometer spectrum, which is a superposition of the spectra measured by the fast- and slow-axis components of the light.

$$R(\lambda) = I_0 p \left[ \cos^2\theta \left(\lambda - \frac{\Delta\lambda}{2}\right)^2 + \sin^2\theta \left(\lambda + \frac{\Delta\lambda}{2}\right)^2 \right], \tag{4.2}$$

where $I_0$ is the overall intensity of the light arriving at the fiber-optic bolometer and $p$ is the fitting coefficient for the quadrature functions. Solving $\partial \mathrm{R} / \partial\lambda = 0$, we obtain the wavelength position of the measured spectral notch, $\lambda_0$, which is given by

$$\lambda_0 = \frac{1}{2}\cos 2\theta\Delta\lambda, \tag{4.3}$$

Then the sensitivity of the fiber-optic bolometer to polarization perturbations, in terms of the wavelength shift of the spectral notch caused by a unit angle of the linear polarization rotation, is given by

$$\frac{\partial\lambda_0}{\partial\theta} = -\sin 2\theta\Delta\lambda, \tag{4.4}$$

It is seen that the sensitivity to polarization perturbation vanishes when the polarization of the light arriving at the fiber-optic bolometer is aligned with one of the principle axes of the fiber-optic bolometer ($\theta = 0° or 90°$) and assumes the maximal value when the polarization is at 45° with respect to one of the principle axes. However, in practical applications, it may be challenging to pin the polarization of the light at the fiber-optic bolometer to a particular state because fiber bending and rotation as well as temperature variations may cause a large change in the polarization state.

### 4.2.2 Influence of vibration and magnetic field applied on the fiber on fiber-optic bolometer operation

In practical plasma applications, the mechanical vibration and the strong static or quasi-static magnetic field can be present in a magnetic-confinement fusion system. Interferometry measurements on tokamaks have required the use of multi-wavelength approaches to remove mechanical vibrations, and have demonstrated movements of up to 1 cm on double-pass systems at frequencies of a few Hz [48,49]. During disruptions, tokamaks can also experience large amplitude oscillations [50]. How these macroscopic movements of the MCF device correspond to small scale oscillations for measurement systems depends on detailed design, but the potential for signal pollution is high. The optical fiber bending resulting from the mechanical vibration can induce linear birefringence, which can change the polarization of light that guided in the optical fiber. The magnetic field in the MCF systems could be static or evolving slowly over time, as well as have low amplitude, $\delta$ B/B < 0.1 high frequency, > 100 kHz, components discussed in more detail later. Based on applications, the quasi-static magnetic flux density can range from approximately 1 to 12 T, depending on device and location within the torus, inducing a circular birefringence to the fiber and the silicon FP interferometer and a Faraday rotation to the polarization of the light guided in the optical fiber and silicon FP interferometer [51]. As shown in *Section 4.3.2.2*, the fiber-optic bolometer is sensitive to the light polarization due to the birefringence of silicon FP interferometer. Both the mechanical vibration and the dc or quasi-dc magnetic field can cause polarization variations. In this section, we experimentally study the influences of mechanical vibration and quasi-dc magnetic field on the fiber-optic bolometer operation.

### 4.2.3 Experimental setup

The experimental setup to characterize both the mechanical vibration and magnetic field is schematically shown in Fig. 4.16 .This is similar to the setup that will be used for plasma radiation measurement in practical application. A different distributed feedback diode laser with a larger wavelength scanning range was used for the demodulation operating with a same method that demonstrated in the previous section. A triangle wave with frequency of 2 kHz was used to modulate the distributed feedback laser. In this case, the scanning wavelength range was 600 pm.

Besides the radiation, ambient temperature variations as well as laser drift will also cause responses to the bolometer. In order to remove these noises, we constructed a reference bolometer that is placed close to the sensing bolometer but shielded from the radiation. A portion of the light from the diode laser is split out via a fiber-optical coupler with a couple ratio of 33/67 and delivered to the reference bolometer. Laser wavelength drift and ambient temperature variations cause equal contributions to the responses of both bolometers. Therefore, the difference between the wavelength positions of the sensing bolometer and the reference bolometer removes the common noises and only contains the information from the radiation-induced temperature rise. For either the sensing bolometer or the reference bolometer, the returned light was directed to a photodetector and recorded by the data acquisition system with a sampling rate of 2 MHz. In this way, the fiber-optic bolometer mirrors the traditional reference bolometer [7] that arranges sensing and reference bolometers a Wheatstone bridge to remove environmental noise and demodulates an AC bridge drive to achieve high signal to noise.

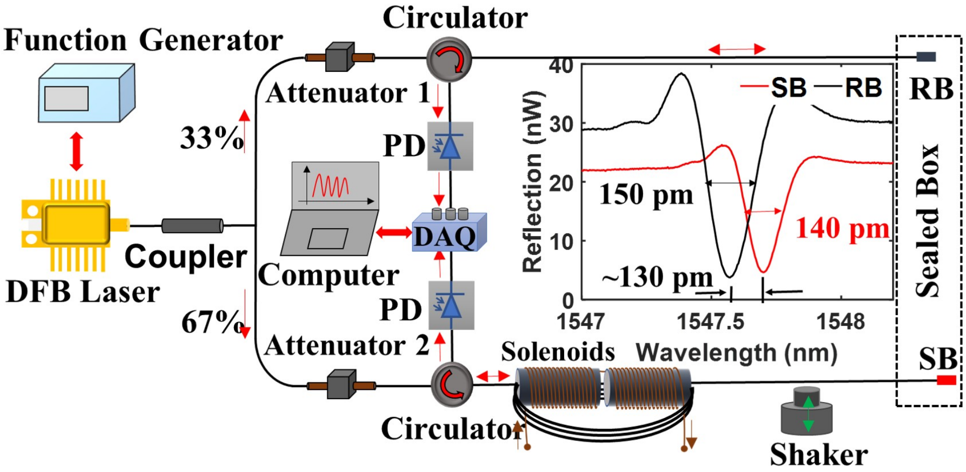

Figure 4.16: Experimental setup to characterize noise performance of the fiber-optic bolometer system. The inset shows the reflection spectral notches of the sensing bolometer and the resistive bolometer at room temperature.

As discussed early, the fiber-optic bolometers were sensitive to the power of the light injected to the fiber-optic bolometers due to the absorption of the gold coating. We introduced two attenuators that allowed us to conveniently fine-tune the relative positions of the resonant wavelengths of the two FB interferometers. The reflection spectra of the two fiber-optic bolometers are shown in the inset of Fig. 4.16 and the resonant notches were separated by 130 pm, which is well within the scanning range (600 pm) of the distributed feedback laser.

For mechanical vibration testing, vibration was applied to the lead-in single-mode fiber of the sensing bolometer by attaching the fiber on an electromagnetic shaker. For magnetic field testing, a solenoid was used to generated magnetic field and a few turns of the lead-in single-mode fiber of the sensing bolometer was threaded into the air-core of a solenoid so that the magnetic field was applied along the axial direction of the fiber. More details of the test conditions are provided below.

#### 4.2.3.1 Mechanical vibration

For the mechanical vibration test, we induced a 5 Hz vibration with a peak-to-peak displacement of 0.5 cm to the fiber using the electromagentic shaker. The shaker was turned on at t = 6 s and remained on until t = 25 s when it was turned off. During the process, the measured differential wavelength shift and the equivalent temperature change are shown in Fig. 4.17 Significant variations in the signal was observed between 6 – 25 s when the vibrator was on. The standard deviations of the signal under vibration (6 - 25 s) are 0.066 pm and 0.78 mK in terms of wavelength shift and equivalent temperature change, respectively. Without vibration (1-5s and 26 - 40 s), these values are, respectively, 0.014 pm and 0.16 mK. It is seen that the vibration increased the noise of the fiber-optic bolometer system by 5 times. A close-up view of the signal under vibration is shown in the inset of Fig. 4.17 and reveals that the variation had an oscillation pattern with the same frequency (5 Hz) of the vibration.

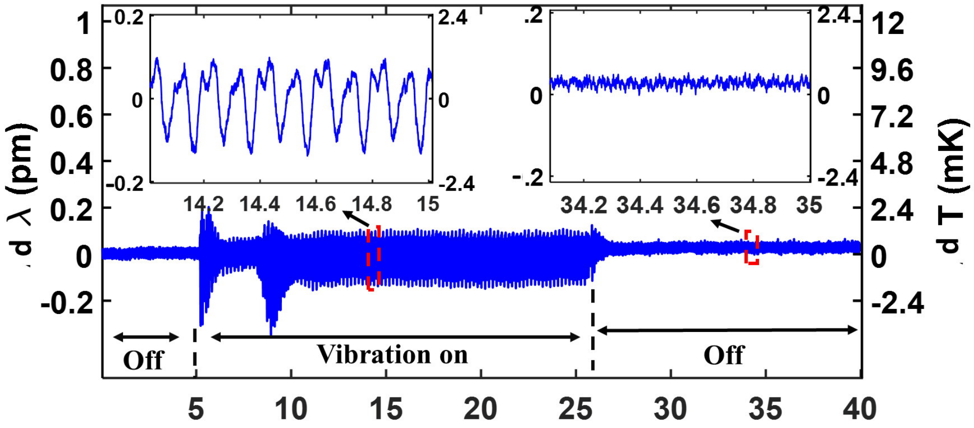

Figure 4.17: Fiber-optic bolometer response to 5-Hz vibration applied on the lead-in single-mode fiber of the fiber-optic bolometer induced by an electromagnetic shaker. The insets are the enlarged view of the signals when the shaker was on (left) and off (right).

#### 4.2.3.2 Magnetic field

To study its effect on the fiber-optic bolometer with a regular single-mode fiber, we placed several loops of the optical fiber with a total length of 1.1 m was placed in the air-core of a solenoid that generated a maximum of 0.05 T magnetic field at the center of the core (measured by a gaussmeter). The expected Faraday rotation from the magnetic field over this length of fiber is 1.7 degree. The solenoid was alternately turned on and off at every 10 s and the response of the fiber-optic bolometer is shown in Fig. 4.18 . It shows that the 0.05 T magnetic field caused a wavelength shift of 0.15 pm, equivalent to a temperature change of 1.8 mK of the fiber-optic bolometer, which is 11 times larger than the noise of the fiber-optic bolometer obtained in quiet magnetic-field-free conditions (0.014 pm or 0.16 mK). Note that, in addition to the step changes in response to the magnetic field, the fiber-optic bolometer signal appears to have a low-frequency drift over the 50 s time span of test. Such drift was also observed in other experiments described later. The exact origins of the drift are unknown. A possible mechanism responsible for the drift is the change of the laser heating due to the intensity variations of the distributed feedback laser. Nevertheless, the fiber-optic bolometer is useful for short pulse operation of MCF applications where the plasma radiation only lasts a few milliseconds and the slow drift of the fiber-optic bolometer signal can be effectively filtered out.

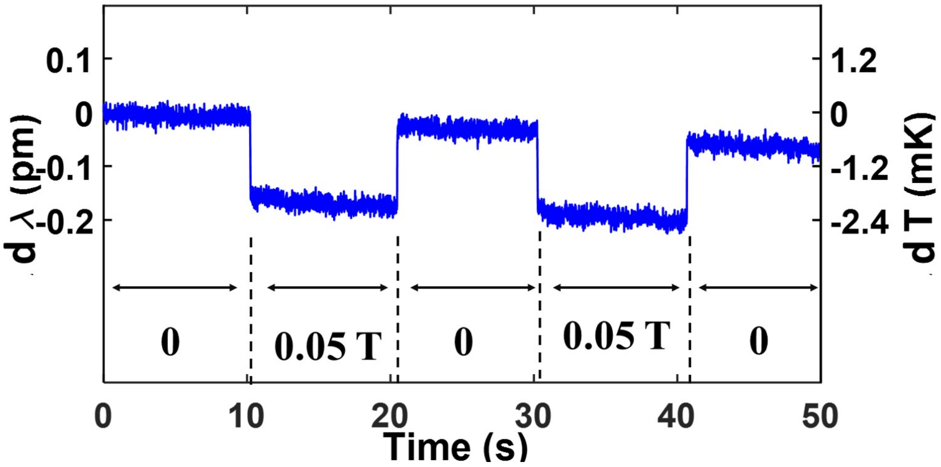

Figure 4.18: Fiber-optic bolometer response to magnetic field of 0.05 T and frequency modulated by a square wave of 0.1 Hz.

Finally, we note that the polarization state of the light arriving at the fiber-optic bolometer was not controlled. From *Section 4.3.2.3*, the sensitivity of the fiber-optic bolometer to polarization perturbations is dependent on the specific polarization state and specific perturbations. As a result, the responses of the fiber-optic bolometer to vibration and magnetic field could be different at different polarization state. Nevertheless, the results show that both mechanical vibration and magnetic field can cause significant noise increase or measurement errors due to the birefringence of the fiber-optic bolometer head and it is important to mitigate these effects for practical applications of the fiber-optic bolometer.

### 4.2.4 Mitigation of birefringence effects

In this section we demonstrate two effective methods to mitigate the birefringence effects. The first is to use polarization maintaining fiber in the fiber-optic bolometer system and the second is to use a polarization scrambler to randomize the polarization of light from the laser source.

#### 4.2.4.1 Fiber-optic bolometer system with polarization maintaining lead-in fiber

We fabricated two new fiber-optic bolometers with polarization maintaining lead-in fibers and replaced the fiber-optic bolometers with the regular single-mode fiber in the fiber-optic bolometer system shown in Fig. 4.19. In fabricating the fiber-optic bolometer, the principle axes of the polarization maintaining fiber were aligned with the principle axes of the fiber-optic bolometer at an arbitrary angle. The inset in Fig. 4.19 . shows the reflection spectra of these two fiber-optic bolometers with polarization maintaining fibers and the spectral widths are 130 and 160 pm for the sensing bolometer and the reference bolometer, respectively.

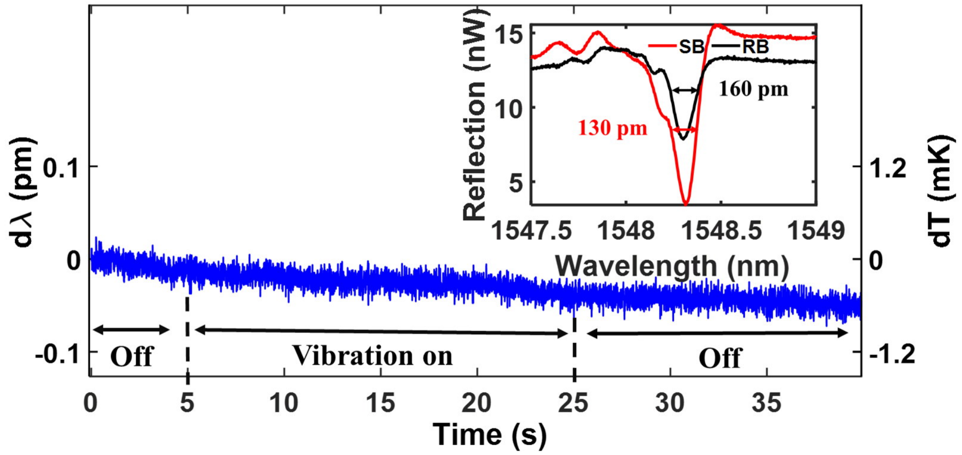

Figure 4.19: Polarization maintaining fiber-optic bolometer response to vibration The inset shows the reflection spectra the sensing bolometer and reference bolometer at room temperature.

For mechanical vibration test, only the polarization maintaining fiber was placed on the shaker and vibrated. The mitigation of birefringence effect was characterized by using these polarization maintaining bolometers without changing any other devices. Polarization maintaining fibers have large linear birefringence by design to prevent the coupling of the two principle linear polarization states so that the polarization of the light is maintained in the fiber even when the fiber is subject to mechanical perturbation. Indeed, the signal from the bolometer constructed on polarization maintaining fibers did not show any observable changes when the vibration was turned on, as shown in Fig 4.19.

Similar to vibration, the effect from Faraday rotation can be greatly suppressed using a polarization maintaining fiber. For a polarization maintaining fiber, the circular birefringence induced from the magnetic field is swamped by the much higher linear birefringence of the polarization maintaining fiber. In general, the effective length that Faraday rotation can accumulate is roughly half of the beat length of the fiber [52]. While the beat-length of regular single-mode fiber can reach 10 m at the wavelength of 1550 nm [53], it is < 5 mm at 1550 nm for the polarization maintaining fiber used here, representing a three-orders of magnitude reduction on the effective interaction length between the fiber and the magnetic field. We then tested the fiber-optic bolometer with a polarization maintaining fiber pigtail of the same length in the field and repeated the experiment described in *Section 4.3.3.3*. The result is shown in Fig. 4.20. Clearly, under the current system resolution, no changes were observed by the presence of the 0.05 T magnetic field.

We note that the polarization maintaining fiber was only applied to the fiber-optic bolometer pigtail, which is sufficient for the purpose of demonstration, and single-mode fiber were still used for other component in the system. The fiber-optic bolometer system would be still sensitive to vibrations and magnetic field applied on the other components with regular single-mode fibers. In practical applications, all fibers in the system needs to be replaced with polarization maintaining fibers.

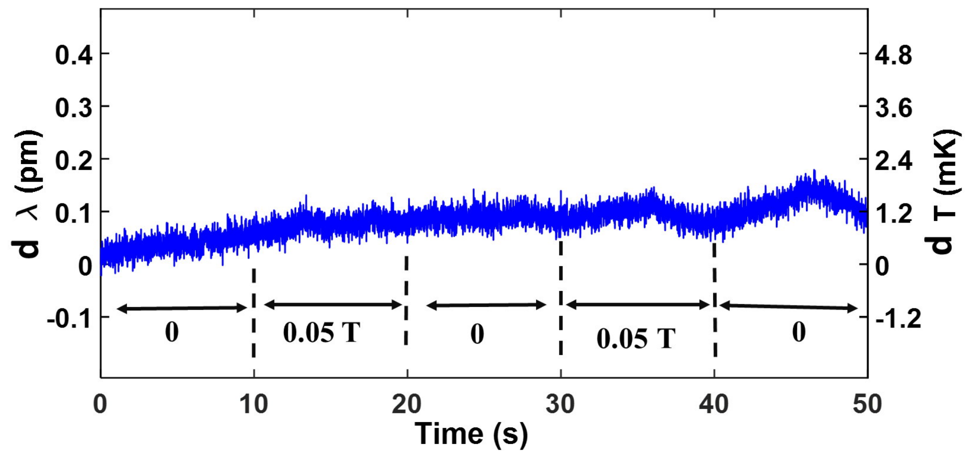

Figure 4.20: Polarization maintaining fiber-optic bolometer response to the magnetic field.

#### 4.2.4.2 Polarization scrambling

This method aims at randomizing the polarization state of the light emitted from the distributed feedback laser using a polarization scrambler at a speed much higher than the scanning speed of the laser. As a result, each spectral frame measured by the scanning laser is the average of results from all generated random polarization states and is independent on the polarization state of the distributed feedback diode laser. Here, a polarization scrambler (Model: PS3000, FiberPro) with a modulation frequency of 1 MHz was used to randomize the scanning laser before the light directed into the coupler. We repeated the vibration test and magnetic field test described in *Sections 4.3.3.2 and 4.3.3.3*. Note that regular single-mode fiber was used throughout the fiber-optic bolometer system. Figure 4.21 shows the output of the fiber-optic bolometer system when vibration with frequency of 5 Hz was applied to the sensing bolometer between 6 - 25 s. No extra noise was induced due to the vibration. Figure 4.22 is the result when the pigtail fiber of sensing bolometer was exposed to a magnetic field of 0.05 T modulated by a 0.1 Hz square waveform. It is seen that the fiber-optic bolometer system shows unmeasurable sensitivity to the magnetic field.

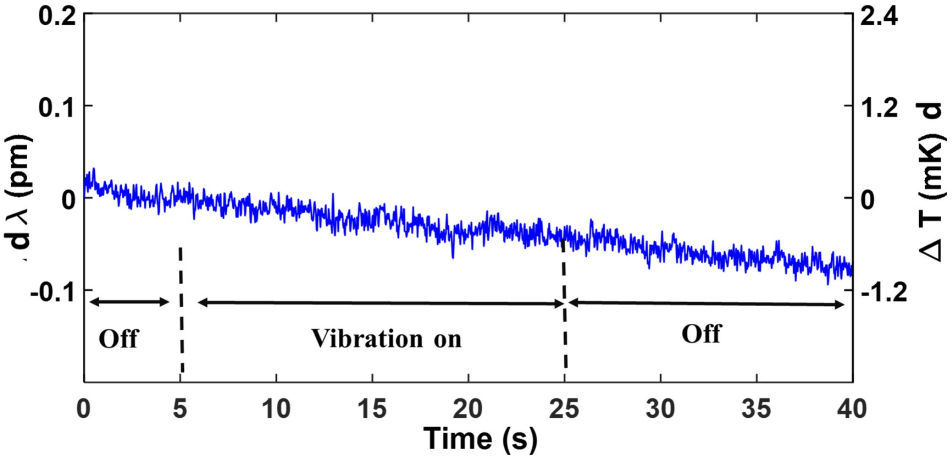

Figure 4.21: Fiber-optic bolometer response to vibration after using a polarization scrambler.

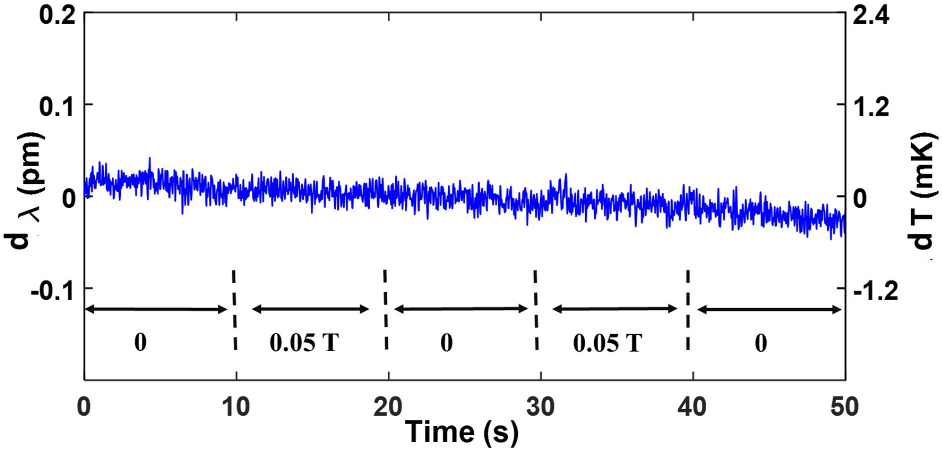

Figure 4.22: Fiber-optic bolometer response to magnetic field after using a polarization scrambler.

#### 4.2.4.3 Comparison of polarization maintaining fiber-optic bolometer and polarization scrambling

In our experiment, both the use of polarization maintaining fibers and the polarization scrambler showed promising ability to mitigate the birefringence effects of the fiber-optic bolometer. The polarization maintaining fiber relies on maintaining a linear polarization state of the light throughout the system. The polarization extinction ratio of polarization maintaining fibers may be reduced with increased fiber length and/or severe environmental perturbations. Compare with the polarization maintaining fiber-optic bolometer, the polarization scrambler randomizes the polarization states of the light in regular single-mode fibers that can cover the whole Poincare sphere, which may make the system more resilient to environmental perturbations. However, effectiveness of the polarization scrambler in this application is dependent on the scrambling speed and the maximum modulation frequency of commercial polarization scramblers is typically limited to a few MHz. For an fiber-optic bolometer system with high measurement speed, polarization scrambling may not be suitable. Inductive sensors close to the plasma have observed fast magnetic field fluctuations of order the 10's of mT, which could be aliased with a high-speed polarization scrambling. In NSTX-U, sustained ion-cyclotron emission was observed up to 5 MHz with $\partial$B/B of a few percent [54] and stronger intermittent poloidal magnetic field fluctuations prior to edge localized modes have been observed on many devices in the 10's to 100's of kHz range [55]. While these signals will fall off quickly moving away from the plasma, while line-integrated emission seen by bolometry will not, a polarization scrambling solution may still be acceptable if for some reason a polarization maintaining fiber-optic bolometer encounters other problems when testing integration into MCF systems

### 4.2.5 Effect of vibration and magnetic field applied on fiber-optic bolometer head

Note that the vibration and magnetic field were only applied to the optical fibers of the fiber-optic bolometer system, but not on the silicon pillar that forms the fiber-optic bolometer head. The small size of the silicon pillar and the fact that it is directly attached to the end face of a pigtail fiber makes it difficult to apply vibration and magnetic field exclusively on the silicon FP interferometer. Nevertheless, a brief discussion on this matter should be worthwhile.

The vibration is unlikely to cause significant bending to the silicon pillar because the small size and the cantilever configuration of the fiber-optic bolometer head. Consequently, vibration of the silicon pillar is not expected to significantly change the polarization state of the light traveling in the silicon pillar and cause degradation in the signal. However, the effect of magnetic field applied on the silicon pillar needs more careful consideration because of the relatively large Faraday effect of silicon with a Verdet constant  40 times larger than that of fused silica at 1550 nm [56, 57]. Magnetic field applied on a material will induce circular birefringence to the material, which can be expressed as

$$\Delta n_c = n_+ + n_- = \nu B\lambda/\pi, \tag{4.5}$$

where $n_+$ and $n_-$ are, respectively, the refractive index for the right- and left-circular polarizations in the material, $\nu$ is the Verdet constant, B is the magnetic field, and $\lambda$ is the light wavelength. Using $\nu = 0.24$ rad/(T·cm) for single-crystal silicon at $\lambda = 1550$ nm [56], we estimate that the maximum magnetic field obtained in the lab B = 0.05 T would yields a circular birefringence of $\Delta n_c = 5.9 \times 10^{-7}$). This is 50 times smaller than the measured value of the linear birefringence of the fiber-optic bolometer head (see *Section 4.3.2.2*). As a result, its effect on the measurement is likely unobservable under the test conditions in this study. It is worth noting that, in practical MCF applications with magnetic field that can reach 12 T, the induced circular birefringence may become comparable to or even exceed the linear birefringence. The two mitigation methods studied here for the linear birefringence of the silicon pillar should be equally effective for the circular birefringence.

### 4.2.6 Conclusion

The advantages of fiber-optics sensing technique motivated us to develop a new fiber-optic bolometer to overcome the limitations of the resistive bolometer. Based on a previously demonstrated fiber-optic bolometer, we studied the influences of mechanical vibration and magnetic field on the performance of fiber-optic bolometers and the mitigation of the influences. First, we characterized the birefringence of the fiber-optic bolometer. The experimental results showed that the fiber-optic bolometer had a high sensitivity to the light polarization variation due to the birefringence of the silicon FP interferometer. Then we characterized the fiber-optic bolometer performance of both mechanical vibration and magnetic field that can be presented in the practical plasma applications. Both mechanical vibration and magnetic field contribute to the variation of polarization of the light guided in the fiber, which, in turn, increase the noise of the fiber-optic bolometer system. The experimental results showed that both the mechanical vibration and magnetic field introduce large noise to the performance of fiber-optic bolometer. To mitigate the birefringence effects, two methods were studied: using polarization maintaining fiber for fiber-optic bolometer system and using a polarization scrambler after the laser source. The experimental results show that these methods can effectively mitigate the birefringence effects of the silicon FP interferometer. These results show that the fiber-optic bolometer is a promising technology for plasma diagnosis in magnetic confinement fusion systems. We also note that, due to limitation of the experimental set up in our laboratory and the complexity of the fusion systems, it is difficult to accurately simulate the vibration and magnetic field in fusion systems. Further development is needed and underway before the bolometer can be tested in fusion systems in practice.

# CHAPTER 5

# SUMMARY AND FUTURE WORK

## 5.1 Summary

In this dissertation, we mainly focused on the development of fiber-optic interferometric bolometer. We first presented a model to study the noise performance of fiber-optic extrinsic FP interferometric sensors with planar metal mirrors. Taking advantage of this model, we theoretically studied the effects of key parameters of FP cavity, including the metal mirror thickness, beam width, cavity length, and wedge angle, on the sensor noise performance. Based on the simulation results, we propose an empirical equation for estimating the noise of the sensor system and a formula involving visibility and bandwidth of the reflection notches that can be used as the figure-of-merit to characterize the inherent sensor noise performance. Our work provides a useful tool for designing, constructing, and interrogating fiber-optic extrinsic FP interferometric sensors with metal mirrors. Based on the analysis through the simulation model, we focuses on the development of low-finesse fiber-optic FP interferometric bolometer and the high-finesse fiber-optic bolometer. For the low finesse fiber-optic bolometer, we proposed a new fiber-optic temperature sensor with fast response and high resolution by cutting off the heat transition path from the sensor sensing part to the fiber stub. The experimental results showed a large improvement in the sensor response time (13 vs. 83 ms). In addition to the new temperature sensor, we proposed a novel signal processing method to eliminate the spurious jumps encountering in the wavelength tracking demodulation method. The modified correlation demodulation method could successfully eliminate the spurious jumps indicating a higher accuracy in the sensor reading. For the high-finesse fiber-optic interferometric sensor, we first demonstrated a novel fiber-optic bolometer based on a high-finesse silicon FP interferometer. The front mirror of the FP cavity was coated by the high reflection dielectric coating and the back mirror was coated by using the high reflection thin gold film. The experimental results tested at a lab condition showed a noise equivalent power density of 0.27 W/m$^2$, which is comparable with the conventional resistive bolometer. Taking advantage of this new bolometer, we experimentally studied the mechanical vibration and quasi-dc magnetic field , both of which can present in the practical applications, influence on the sensor noise performance. The experimental results verified that the influences of mechanical vibration and magnetic field are mainly from the birefringence of the silicon FP interferometer. To mitigate the birefringence effects, we proposed two efficient methods including: polarization maintaining fiber replace the single-mode fiber, and polarization scrambling. The experimental results show that both methods can efficiently mitigate the birefringence effects. These results show that the fiber-optic bolometer is a promising technology for plasma diagnosis in MCF systems.

## 5.2 Future Work

In the development of fiber-optic bolometer, we are still in the phase of theoretical analysis and experimental verification. For simplicity, the silicon sensing part of the fiber-optic bolometer was mainly glued to the tips of the single-mode fiber by using epoxy. The epoxy has a temperature tolerance less than 150 °C. However, in the practical applications, the fiber-optic bolometer needs to be baked first at a high temperature condition around 300 °C, which is far beyond the tolerance temperature of epoxy. A novel epoxy free fabrication method is necessary.

Furthermore, the magnetic field in the MCF systems could be static or evolving slowly over time with low amplitude, $\delta$B/B < 0.1 high frequency, > 100 kHz, components. The variation of the magnetic field may cause eddy current on the fiber-optic bolometer leading to unexpected temperature fluctuations, therefore the effects of the eddy current induced by the varying magnetic field on the bolometer need to be examined.

Finally, as we demonstrated before, the high reflection thin gold mirror at the back surface of the FP interferometer is used to improve the reflectivity of the FP interferometer. The reflectivity of the gold mirror is temperature dependent. In the practical applications, the temperature variations due to the absorption of the fiber-optic bolometer to the plasma radiation may change the reflectivity of the FP interferometer. The details of this influence need to be explored.

# APPENDIX

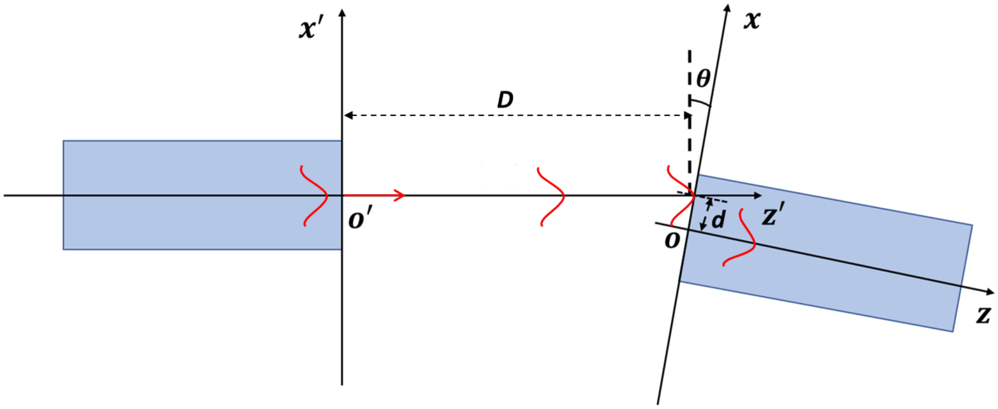

Figure .0.1: Schematics for calculating the filed coupling efficient for the light from fiber $o'$ coupled into fiber $o$ with a longitudinal ($D$), lateral ($d$), and angle ($\theta$) misalignment [31].

To calculate the coupling coefficient for each round trip of the light in the extrinsic FP interferometric sensor, we start with the calculation of the coupling coefficient of two single-mode fibers as shown in Fig.0.1, where the light of a free-space wavelength $\lambda_0$ from fiber $o'$ propagates a longitudinal propagation of $D$ in a uniform medium with a refractive index of $n$ and is coupled into fiber $o$ with a lateral ($d$) and angle ($\theta$) misalignment with respect to fiber $o'$ [31]. The fundamental mode of an single-mode fiber can be approximated by a Gaussian beam and, in $(x', y', z')$ coordinates, its electrical field in the free space can be written as

$$E_1\left(x',y',z'\right) = E_{01}\frac{\omega_0}{\omega'}exp[\frac{-x'^2-y'^2}{\omega'^2}]exp\{i[kz'+k\frac{x'^2+y'^2}{2R'}-\varphi\left(z'\right)]\}, \tag{1}$$

where

$$\omega' = \omega_0\sqrt{1+\left(\frac{z'}{z_0}\right)^2}, \tag{2}$$

$$R' = z'\left(1+\frac{z_0^2}{z'^2}\right), \tag{3}$$

$$\varphi\left(z'\right) = tan^{-1}\left(\frac{z'}{z_0}\right), \tag{4}$$

are, respectively, the spherical wavefront radius, wavefront radius curvature, and the Gouy phase of the Gaussian beam after the propagating a distance of z', $E_0$, $\omega_0$, and $z_0 = \pi\omega_0^2 n/\lambda_0$ are, respectively, the amplitude, waist radius, and the Rayleigh range of Gaussian beam, respectively, and $k = 2\pi n/\lambda_0$ is the wave number. To calculate the coupling coefficient, the field given by Eq. (1) is converted to $(x, y, z)$ coordinates at the coupling plane $z = 0$ by substituting

$$x' = (x - d)\cos\theta, \tag{5}$$

$$y' = y, \tag{6}$$

$$z' = (x - d)\sin\theta + D, \tag{7}$$

Eq. (1), which yields

$$E_{1D}\left(x', y', z'\right) = E_{01}\frac{\omega_0}{\omega'}exp[\frac{-(x-d)^2\cos^2\theta - y^2}{\omega'^2}]exp\{i[kz' + k\frac{(x-d)^2\cos^2\theta + y^2}{2R'} - \varphi\left(z'\right)]\}, \tag{8}$$

The equation can be further simplified by assuming a small angle ($\theta$) or $\sin\theta \approx \theta$, $\cos\theta \approx 1$, and $z' \approx D$. Substituting these approximations into Eq. (A8), we obtain the electrical field from fiber $o'$ at the coupling plane $z = 0$

$$E_{1D} = E_{01}\frac{\omega_0}{\omega'}exp\{-\left(\frac{1}{\omega'^2} - i\frac{k}{2R'}\right)[(x-d)^2 + y^2] + ik\theta x - ikd\theta\}exp[i\phi\left(D\right)], \tag{9}$$

where $\phi\left(D\right) = KD - tan^{-1}\left(D/z_0\right)$ is the phase change due to the wave propagation.

The fundamental mode of fiber $o$ is also a Gaussian beam and its field at the coupling plane can be written in $(x, y, z)$ coordinates as

$$E_2 = E_{20}exp\left(\frac{-x^2 - y^2}{\omega_0^2}\right). \tag{10}$$

Then the coupling coefficient is given by [30]:

$$\eta = \frac{\iint_{-\infty}^{+\infty} E_{1D}E_2^* dxdy}{\left(\iint_{-\infty}^{+\infty} E_{1D}E_{1D}^* dxdy\right)^{\frac{1}{2}}\left(\iint_{-\infty}^{+\infty} E_2E_2^* dxdy\right)^{\frac{1}{2}}} \tag{11}$$

Substituting Eqs. (9) and (10) into Eq. (11) and after some straightforward algebra, we obtain

$$\eta_m = \frac{2}{\omega_0\omega'_m q}e^{-pd_m^2\left(1-\frac{p}{q}\right)}e^{-\frac{k^2\theta_m^2}{4q}}e^{-ikd_m\theta_m\left(1-\frac{p}{q}\right)}e^{i\phi_m}, \tag{12}$$

where $p = \frac{1}{w'^2} - i\frac{k}{2R'}$ and $q = p + \frac{1}{\omega_0^2}$. For the case that there are no angular and lateral alignments, $\theta = 0$, $d = 0$, and the coupling coefficient becomes

$$\eta|_{\theta=0,d=0} = \frac{2}{\omega_0\omega' q}exp[i\phi\left(D\right)], \tag{13}$$

For a high-finesse extrinsic FP interferometric sensor, the calculation of coupling coefficient for each round trip could be simply treated as the case shown in Fig. 1. The longitudinal, angle, and lateral mismatch after $m$ round trips are given by

$$D_m = 2mL, \tag{14}$$

$$\theta_m = 2m\alpha, \tag{15}$$

$$d_m = 2m^2\alpha L, \tag{16}$$

respectively, where $L$ is the cavity length of extrinsic FP interferometric sensor, and $\alpha$ is the wedge angle formed by two surfaces of the sensor [31]. Then the coupling coefficients for multiple roundtrips can be obtained by substituting Eqs.(8)-(16) into Eq. (12).

Note that assuming $R' = \infty$, we can obtain the power coupling coefficient, $|\eta|^2$ from Eq. (12):

$$|\eta|^2 = \left(\frac{2\omega_0\omega'}{\omega_0^2 + \omega'^2}\right)^2 exp\left(-\frac{2d^2}{\omega_0^2 + \omega'^2}\right) exp[-\frac{2(\pi\omega_0\omega'\theta n)^2}{\left(\omega_0{}^2 + \omega'^2\right)\lambda_0{}^2}], \tag{17}$$

which is consistent with the results shown in Ref. [31] (except for the omission of $n$ in the third term in Ref. [31]).

# BIBLIOGRAPHY

# BIBLIOGRAPHY

[1] J. Ongena, R. Koch, R. Wolf, and H. Zohm, “Magnetic-confinement fusion,” *Nat. Phys.* vol. 12, pp. 398-410, 2016.

[2] M. L. Reinke, J. W. Hughes, A. Loarte, D. Brunner, I. H. Hutchinson, B. LaBombard, J. Payne, and J. L. Terry, "Effect of N2, Ne and Ar seeding on Alcator C-Mod H-mode confinement," *J. Nucl. Mater.* vol 415, pp. S340-S344, 2011.

[3] A. Kallenbach, M. Bernert, T. Eich, J. C. Fuchs, L. Giannone, A. Herrmann, J. Schweinzer, W. Treutterer, and A. U. T. the, "Optimized tokamak power exhaust with double radiative feedback in ASDEX Upgrade," *Nucl. Fusion*, vol. 52, pp. 122003, 2012.

[4] P. Monier-Garbet, P. Andrew, P. Belo, G. Bonheure, Y. Corre, K. Crombe, P. Dumortier, T. Eich, and R. Felton, J. Harling, “Impurity-seeded ELMy H-modes in JET, with high density and reduced heat load,” *Nucl. Fusion*, vol. 45, pp. 1404 2005.

[5] T. Petriea, M. Wadea, N. Brooks, M. Fenstermacher, M. Groth, A. Hyatt, R. Isler, C. Lasnier, A. Leonard, M. Mahdavi, G. Porter, M. Schaffer, J. Watkins, W. West, “Compatibility of the radiating divertor with high performance plasmas in DIII-D,” *J. Nucl. Mater.* vol. 363-365, pp. 416-420, 2007.

[6] N. Asakura, T. Nakano, N. Oyama, T. Sakamoto, “Investigations of impurity seeding and radiation control for long-pulse and high-density H-mode plasmas in JT-60U,” *Nucl. Fusion*, vol. 49, pp. 115010, 2009.

[7] K. F. Mast, J. C. Vallet, C. Andelfinger, P. Betzler, H. Kraus, and G. Schramm, "A low noise highly integrated bolometer array for absolute measurement of VUV and soft x radiation," *Rev. Sci. Instrum.* vol. 62, pp. 744-750, 1991.

[8] H. Meister, M. Willmeroth, D. Zhang, A. Gottwald, M. Krumrey, and F. Scholze, “Broadband efficiency calibration of ITER bolometer prototypes using Pt absorbers on SiN membranes,” *Rev. Sci.c Instrum.* vol. 84, pp. 123501, 2013.

[9] B. Peterson, H. Parchamy, N. Ashikawa, H. Kawashima, S. Konoshima, A. Kostryukov, I. Miroshnikov, D. Seo, and T. Omori, “Development of imaging bolometers for magnetic fusion reactors (invited),” *Rev. Sci. Instrum.* vol. 79, pp. 10E301, 2008.

[10] D. L. Griscom, "Radiation hardening of pure-silica-core optical fibers by ultra-highdose $\gamma$-ray pre-irradiation," *J. Appl. Phys.* vol. 77, pp. 5008-5013, 1995.

[11] A. Gusarov and S. K. Hoeffgen, "Radiation effects on fiber gratings," *IEEE Trans. Nucl. Sci.* vol. 60, pp. 2037-2053, 2013.

[12] C. Vorpahl, W. Suttrop, M. Ebner, B. Streibl, and H. Zohm, "Deformation measurement of internal components of ASDEX Upgrade using optical strain sensors," *Fusion Eng. Des.* vol 88, pp. 537-540, 2013.

[13] Q. Sheng, B. Li, N. Uddin, A. Mitul, Y. Zhu, Z. Qiu, and M. Han, “High-resolution, fast-response fiber-optic temperature sensor with reduced end conduction effect,” *Opt. Express* vol 23, pp. 7237-7247, 2015.

[14] W. Tsai, and C. Lin, “A novel structure for the intrinsic Fabry-Perot fiber-optic temperature sensor,” *J. Light, Technol.* vol. 19, 682-686, 2001.

[15] R. Rong, H. Sun, X. Qiao, J. Zhang, M. Hu, and Z. Feng, “A miniature fiber-optic temperature sensor based on a Fabry-Perot interferometer,” *J. Opt.* vol. 14, pp. 045002, 2012.

[16] Q. Yu, and X. Zhou, “Pressure sensor based on the fiber-optic extrinsic Fabry-Perot interferometer,” *Photonics Sensor* vol. 1, pp. 72-83, 2011.

[17] J. Alcoz, C. Lee, and H. Taylor, “Embedded fiber-optic Fabry-Perot ultrasound sensor,” IEEE Trans. *Ultrason. Ferroelectr. Freq. Control* vol. 37, pp. 302-306, 1990.

[18] W. Zhang, R. Wang, Q. Rong, X. Qiao, T. Guo, Z. Shao, J. Li, W. Ma, “An optical fiber Fabry-Perot interferometric sensor based on functionalized diaphragm for ultrasound detection and imaging,” *IEEE Photonics J.* vol. 9, pp. 7103208, 2017.

[19] G. Liu, Q. Sheng, W. Hou, and M. Han, “Optical fiber vector flow sensor based on a silicon Fabry–Perot interferometer array,” *Opt. Lett.* vol. 41, pp. 4629-4632, 2016.

[20] W. Hou, G. Liu, M. Han, “A novel, high-resolution, high-speed fiber-optic temperature sensor for oceanographic applications,” *In Proceedings of the 2015 IEEE/OES 11th Current, Waves and Turbulence Measurement Conference (CWTM 2015)*, 2015.

[21] Z. Ran, Y. Rao, J. Zhang, Z. Liu, and B. Xu, “A miniature fiber-optic refractive-index sensor based on laser-machined Fabry-Perot interferometer tip,” *J. Light. Technol.* vol. 27, pp. 5426-5429, 2009.

[22] T. Zhang, S. Talla, Z. gong, S. Karandikar, K. Giorno, and L. Que, “Biochemical sensing with a polymer-based micromachined Fabry-Perot sensor,” *Opt. Express* vol. 18, pp. 18394-18400, 2010.

[23] Y. Zhao, X. Hu, S. Hu, and Y. Peng, “Applications of fiber-optic biochemical sensor in microfluidic chips: a review,” *Biosens. Bioelectron.* vol. 166, pp. 112447, 2020.

[24] X. Bao, and L. Chen, "Recent Progress in Distributed Fiber Optic Sensors," *Sensors* vol. 12, pp. 8601-8639, 2012.

[25] G. Liu, M. Han, and W. Hou, “High-resolution and fast-response fiber-optic temperature using silicon Fabry-Perot cavity,” *Opt. Express* vol. 23, pp. 7237-7247, 2015.

[26] M. Reinke, M. Han, G. Liu, G. Eden, R. Eveblij, and M. Haverdings, “Development of plasma bolometers using fiber-optic temperature sensors,” *Rev. Sci. Instrum.* vol. 87, pp. 11E708, 2016.

[27] L. Sanchez-Soto, J. Monzon, and G. Leuchs, “The many facets of Fabry-Perot,” *Eur. J. Phys.* vol. 37, pp. 064001, 2016.

[28] N. Tran, C. Campbell, and F. Shi, “Study of particle size effects on an optical fiber sensor response examined with Monte Carlo simulation,” *Appl. Opt.* vol. 45, pp. 7557-7566, 2006.

[29] Y. Zhang, Y. Li, T. Wei, X. Lan, Y. Huang, G. Chen, and H. Xiao, "Fringe visibility enhanced extrinsic Fabry–Perot interferometer using a graded index fiber collimator," *IEEE Photonics J.* vol. 2, pp. 469-481, 2010.

[30] O. Kilic, M. Digonnet, G. Kino, and O. Solgaard, “Asymmetrical spectral response in fiber Fabry–Perot interferometers,” *J. Light. Technol.* vol. 27, pp. 5648–5656, 2009.

[31] K. K. Chin, Y. Sun, G. Feng, G. E. Georgiou, K. Guo, E. Niver, H. Roman, and K. Noe, "Fabry-Perot diaphragm fiber-optic sensor," *Appl. Opt.* vol. 46, pp. 7614-7619, 2007.

[32] D. Marcuse, "Loss Analysis of Single-Mode Fiber Splices," *Bell Labs Tech. J.* vol. 56, pp. 703-718, 1977.

[33] M. Born, and E. Wolf, Principles of Optics (Sixth Edition) (Pergamon, 1980), Chap. 1.

[34] M. Born, and E. Wolf, Principles of Optics (Sixth Edition) (Pergamon, 1980), Chap. 13.

[35] C. Ma and A. Wang, “Signal processing of white-light interferometric low-finesse fiber-optic Fabry-Perot sensors,” *Appl. Opt.* vol. 52, pp. 127-138, 2013.

[36] Y. Yang, F. Ma, K. Chen, and Q. Yu, “High-speed and high-resolution low-coherence interferometric demodulation without phase jumps,” *IEEE Sens. J.* vol. 20, pp. 12225-12231, 2020.

[37] G. Liu, W. Hou, W. Qiao, and M. Han, "Fast-response fiber-optic anemometer with temperature self-compensation," *Opt. Express* vol. 23, pp. 13562-13570, 2015.

[38] Y. Zhao, L. Cai, and X. Li, "Temperature-Insensitive Optical Fiber Curvature Sensor Based on SMF-MMF-TCSMF-MMF-SMF Structure," *IEEE Trans. Instrumen. Meas.* 66, pp. 141-147, 2017.

[39] P. Morkel, R. Laming, and D. Payne. "Noise characteristics of high-power doped-fibre superluminescent sources," *Electron. Lett.* vol. 26, pp. 96-98, 1990.

[40] C. G. Askins, M. A. Putnam, E. J. Friebele, "Instrumentation for interrogating many-element fiber Bragg grating arrays," in *Proc. SPIE Smart Sensing, Processing and Instrumentation* 2444, 257, 1995.

[41] W. L. Emkey, C. A. Jack, “Analysis and evaluation of graded-index fiber-lenses,” *J. Light. Tchnol.* vol. LT-5, 1987.

[42] G. Liu, Q. Sheng, W. Hou, and M. Han, “Influence of fiber bending on wavelength demodulation of fiber optic Fabry-Perot interferometric sensors,” *Opt. Express* vol. 24, pp. 26732-26744, 2016.

[43] G. Liu, W. Hou, W. Qiao, and M. Han, “Fast-response fiber-optic anemometer with temperature self-compensation,” *Opt. Express* vol. 23, pp. 13562-13570, 2015.

[44] Q. Sheng, G. Liu, M. L. Reinke, and M. Han, "A fiber-optic bolometer based on a high-finesse silicon Fabry-Pérot interferometer," *Rev. Sci. Instrum.* vol. 89, no. 6, p. 065002, 2018.

[45] G. Liu, Q. Sheng, W. Hou, M. L. Reinke, and M. Han, "A Silicon-tipped Fiber-optic Sensing Platform with High Resolution and Fast Response," *JoVE* no. 143, p. e59026, Jan. 2019.

[46] Y. H. Meyer, "Fringe shape with an interferential wedge," *J. Opt. Soc. Am.* vol. 71, no. 10, pp. 1255-1263, Oct. 1981.

[47] S. Lederhandler, "Infrared studies of birefringence in silicon," *J. Appl. Phys.* vol. 30, no. 11, pp. 1631-1638, 1959.

[48] T. N. Carlstrom, D. R. Ahlgren, and J. Crosbie, "Real-time, vibration-compensated CO2 interferometer operation on the DIII-D tokamak," *Rev. Sci. Instrum.* vol. 59, no. 7, pp. 1063-1066, 1988.

[49] W. F. Bergerson, P. Xu, J. H. Irby, D. L. Brower, W. X. Ding, and E. S. Marmar, "Far-infrared polarimetry diagnostic for measurement of internal magnetic field dynamics and fluctuations in the C-MOD Tokamak (invited)," *Rev. Sci. Instrum.* vol. 83, no. 10, p. 10E316, 2012.

[50] V. Riccardo, "Chapter 7: Disruption Studies in JET," *Fus. Sci. Technol.* vol. 53, no. 4, pp. 1064-1079, May 2008.

[51] A. M. Smith, "Polarization and magnetooptic properties of single-mode optical fiber," *Appl. Opt.* vol. 17, no. 1, pp. 52-56, Jan. 1978.

[52] R. I. Laming and D. N. Payne, "Electric current sensors employing spun highly birefringent optical fibers," *J. Lightwave. Technol.* vol. 7, no. 12, pp. 2084-2094, 1989.

[53] S. Xie, X. Bao, and L. Chen, Distributed fiber beat length, birefringence and differential group delay measurement using BOTDA technique *(21st International Conference on Optical Fibre Sensors (OFS21)). SPIE* 2011.

[54] E. D. Fredrickson et al., "Emission in the ion cyclotron range of frequencies (ICE) on NSTX and NSTX-U," *Phys. Plasmas* vol. 26, no. 3, p. 032111, 2019.

[55] F. M. Laggner, A. Diallo, M. Cavedon, and E. Kolemen, "Inter-ELM pedestal localized fluctuations in tokamaks: Summary of multi-machine observations," *Nucl. Mater. Energy*, vol. 19, pp. 479-486, May 2019.

[56] H. Piller and R. F. Potter, "Faraday Rotation Near the Band Edge of Silicon," *Phys. Rev. Lett.* vol. 9, no. 5, pp. 203-205, Sep. 1962.

[57] J. Noda, T. Hosaka, Y. Sasaki, and R. Ulrich, "Dispersion of Verdet constant in stress-birefringent silica fibre," *Electron. Lett.* vol. 20, no. 22, pp. 906-908, 1984.

[58] Q. Sheng, G. Liu, N. Uddin, M. L. Reinke, and M. Han, "Fiber-optic silicon Fabry-Perot Interferometric bolometer: the influence of mechanical vibration and magnetic field," Journal of Lightwave Technology, vol. 38, pp. 2547-2554, 2020.

[59] Q. Sheng, G. Liu, N. Uddin, and M. Han, “Analysis of single-mode fiber-optic extrinsic Fabry-Perot interferometric sensors with planar metal mirrors," Applied Optics, vol.60, no. 24, 2021.

[60] Q. Sheng, N. Uddin, and M. Han, "Spurious jumps in wavelength tracking of fiber-optic Fabry-Perot interferometric sensor," which is currently submitted to Journal of the Optical Society of America B and in the process of peer review.